Applications of Noble Gases in Hydrogeology in Fractured, Fast Infiltration Systems — From the Greenland and Columbia Ice Sheets to Hawaii

by

Yi Niu

A dissertation submitted in partial fulfillment
of the requirements for the degree of
Doctor of Philosophy
(Earth and Environmental Sciences)
in the University of Michigan
2018

Doctoral Committee:

Professor Maria Clara Cruz Da Silva Castro, Chair
Adjunct Professor Sarah M. Aciego, University of Wyoming
Professor Avery H. Demond
Associate Research Scientist Chris M. Hall
Professor Kyger C Lohmann
Professor Daniele L. Pinti, Université du Québec à Montréal

Yi Niu

niuyi@umich.edu

ORCID: 0000-0003-1054-2041

© Yi Niu 2018

To my family

ACKNOWLEDGEMENTS

I am indebted to my advisor, Dr. Clara Castro, for her invaluable guidance and continuous support in the past five years. This dissertation would not have been possible without her encouragement and help. Clara is a great mentor and I have learned a lot as we worked on the projects presented here. I would like to thank Dr. Chris Hall, the lab manager of the Noble Gas Lab. Over the years, Chris has provided numerous insightful suggestions on too many aspects that I can list here. Discussions among us covered topics from how to think creatively and present effectively, to practical experiences in the lab work and writing. I also want to thank Dr. Avery Demond, my cognate committee member. I benefited a lot from her class in groundwater hydrology. Special thanks go to Dr. Sarah Aciego, who shared valuable insights in various areas of Earth Sciences, especially in glaciology. Many thanks go to Dr. Kyger C Lohmann for his advice on stable isotopes of water. And finally, I would like to thank Dr. Daniele Pinti for sharing his constructive thoughts and his generosity with his time for my committee meeting and defense.

I would like to thank the past and current members in our research group: Rohit Warrier, WEN Tao, Laura BOUVIER, Julien AMALBERTI, and HAN Guolei for their help, suggestions, and accompany in this endeavor.

I am also thankful to current and past staff member in the department, to name a few, Nancy Kingsbury, Dale Austin, Bill Wilcox, Craig Delap, and especially Anne Hudon, to whom I am indebted for all the help and recommendations.

Many thanks go to my friends for all of their accompany and support and a great time in Ann Arbor. To name a few: GUO Chenghuan, NI Peng, Benjamin Gebarski, Kyle Meyer, PU Xiaofei, WANG Yi, CHEN Sang, LIU Xiaojian, YUAN Ke, AI Wei, CHEN Xi, NIU Shuai, SONG Shiya, and many more.

Last but not least, I want to thank my parents for their unconditional love and continuous support.

TABLE OF CONTENTS

LIST OF TABLES

CHAPTER II

CHAPTER III

CHAPTER IV

CHAPTER V

LIST OF FIGURES

CHAPTER II

CHAPTER III

CHAPTER IV

CHAPTER V

Appendix B

Appendix C

LIST OF APPENDICES

ABSTRACT

Due to their temperature dependency, stable noble gases (He, Ne, Ar, Kr, and Xe) have been routinely used as indicators of past climate in sedimentary systems for over four decades. However, noble gas studies in fractured systems, where infiltration is rapid, remain scarce. These include studies in ice sheets in old cratonic regions (e.g., Antarctica and Greenland), as well as old and recent volcanic areas such as the archipelagos of the Galapagos and Hawaii. Here, noble gas studies in fractured systems are presented. These include two studies in ice-covered regions, one in the Greenland Ice Sheet (GrIS) and the other in the Athabasca Glacier (AG) of the Columbia Icefield in the Canadian Rockies, as well as two studies in a tropical basaltic island, the Island of Maui, Hawaii. Noble gases in the GrIS (Chapter 2) and the AG (Chapter 3) studies are used to constrain glacial meltwater sources, water source altitude and water residence times. In Maui, noble gases are first used to characterize the different water sources contributing to groundwater recharge (e.g., fog, orographic and synoptic-scale rain), and to assess whether timing and location of recharge can be estimated based on atmospheric noble gas signatures (Chapter 4). In Chapter 5, the potential for noble gases to record temporal variations is assessed. Noble gases are used together with oxygen and hydrogen isotopic composition data to further constrain water source altitudes in Maui.

Noble gases in the meltwater samples from both the GrIS and the AG are dominated by a partially equilibrated air-saturated water (ASW) component rather than trapped air in the glacial ice. Water source altitudes based on Xe range between 0.8 and 2.4 km for most samples from the GrIS and between 2.5 and 3.5 km for the AG. A crustal He component, observed in almost all samples in both studies, is used to estimate water residence times. Most meltwater samples from the GrIS yield water residence times between ~100 and ~400 years while two samples yield older ages of ~2000 and ~4000 years. In contrast, samples from the AG yield a younger average of ~160 years.

Water samples were collected in Maui from rain events, springs from perched aquifers, and wells tapping the basal aquifer in June 2014 and February 2016. All samples are in disequilibrium with the atmosphere at the collection point and do not represent the mean annual air temperature. Distinct noble gas signatures in spring and basal aquifer samples suggest that the two types of aquifers are separate entities. In June 2014, noble gases in rainwater and basal aquifer display an ice-like signature possibly related to synoptic-scale rain. The basal aquifer yields similar noble gas signatures in both sampling seasons, while temporal variations are observed in rainwater and spring samples. A few springs and wells yield samples with a significant mantle He component in both years. A combined dataset of noble gas and water stable isotopic composition yield source altitudes for rainwater samples between 0.1 and 3 km above sea level (asl). Water source altitudes for most groundwater samples range between 1.5 and 5.5 km asl, indicating that the water source contributing to groundwater recharge that originate at higher altitudes in the atmosphere was not sampled.

This dissertation has important scientific implications in the fields of glaciology, hydrogeology, and meteorology.

CHAPTER I
Introduction

This chapter introduces studies of stable noble gases in the past few decades and current research focuses, as well as the major problems that this dissertation investigates.

Noble gases occupy the rightmost column in the periodic table. Their outer shells are filled with electrons, rendering them very chemically inert. Furthermore, the five lightest noble gases, He, Ne, Ar, Kr, and Xe, are not radioactive. Therefore, these stable noble gases are mostly sensitive to physical parameters and processes [Mazor, 1972], making them excellent tracers in geochemical processes [e.g., Ozima and Posodek, 2002; Burnard, 2013].

In the past four decades, studies of stable noble gases dissolved in groundwater have greatly enhanced our understanding of surface water and groundwater dynamics by providing indications on flow paths, connectivity between aquifers, and water residence times [e.g., Andrews, 1985; Ballentine et al., 1991; Mazor and Bosch, 1992; Castro et al., 1998a; 1998b; 2000; de Marsily et al., 2002; Kipfer et al., 2002; Kulongoski et al., 2003; Patriarche et al., 2004; Ma et al., 2009; Müller et al., 2016; Pinti et al., 2017]. In addition, noble gas concentrations in the recharge areas of groundwater systems are typically considered to be mostly a function of temperature, pressure (altitude of recharge area), and excess air (EA). Consequently, noble gas temperatures (NGTs) are estimated in NGT models based on the atmospheric Ne, Ar, Kr, and Xe concentrations and assumptions including equilibration altitudes, and have been commonly used as paleothermometers [e.g., Andrews and Lee, 1979; Stute and Schlosser, 1993; Aeschbach-Hertig et al., 2002; Castro and Goblet, 2003; Kulongoski et al., 2004; Ma et al., 2004; Castro et al., 2007; 2012]. In recent years, numerous studies have been dedicated to improving EA estimation and development of NGT models as well as improving our understanding of noble gas behavior in the unsaturated zone and at the air-water interface [e.g., Heaton and Vogel, 1981; Pinti and van Drom, 1998; Ballentine and Hall, 1999; Klump et al., 2007; 2008; Sun et al., 2010; Hall et al., 2012; Aeschbach-Hertig and Solomon, 2013].

In contrast, far fewer studies have been conducted in fractured groundwater systems and, in particular, in volcanic and glacial environments, where the presence of preferential flow paths allows fast water flow from the surface to the bottom of the glaciers. Studies in volcanic settings include those in Lassen and Yellowstone National Parks [e.g., Mazor and Wasserburg, 1965; Kennedy et al., 1985, 1988; Gardner et al., 2010], the Cascades Volcanic Arc [James et al., 2000; Saar et al., 2005], the Réunion Island [Marty et al., 1993], Cabo Verde [Heilweil et al., 2009, 2012], the Azores [Jean-Baptiste et al., 2009], Galápagos [Warrier et al., 2012], and the Canary [Marrero-Diaz et al., 2015] Islands. With the exception of Gardner et al. [2010], Heilweil et al. [2012], and Warrier et al. [2012], most studies did not take advantage of information provided by NGTs. Studies of nobles gases in glacial environments or seas fed by glacial meltwater include those in the Weddell Sea [Schlosser, 1986; Schlosser et al., 1990; Weppernig et al., 1996], firn layer in Greenland [Craig and Wiens, 1996], Lake Vostok, East Antarctica [Jean-Baptiste et al., 2001], southeast Pacific [Hohmann et al., 2002], Lake Bonney, Taylor Valley, Antarctica [Poreda et al., 2004; Warrier et al., 2015; Hall et al., 2017], firn air at the South Pole and Siple Dome, Antarctica [Severinghaus and Battle, 2006], Lake Vida, McMurdo Dry Valleys, Antarctica [Malone et al., 2010], and a mixing model of glacial meltwater, sea water, and air bubbles [Loose and Jenkins, 2014]. These studies focused on seawater mixed with glacial meltwater, snow and firn, ice cores, and modeling. However, none of these studies focused on glacial meltwater, which is a significant end-member in the studies focusing on mixing between seawater and glacial meltwater.

This dissertation focuses on developing new NGT applications in fractured, fast-infiltration systems, in order to explore the information that stable noble gases can provide with respect to the local hydrological cycle. As climate changes intensify, areas in all latitudes are greatly affected. Continental ice sheets at high latitude, e.g., Greenland, are extremely sensitive to and are significant drivers of climate change due to the enormous water masses they store. Understanding climate shifts in the outlet glaciers of the Greenland Ice Sheet (GrIS) is even more critical as these areas may be particularly sensitive to global climate forcing [Intergovernmental Panel on Climate Change, 2013]. Alpine glaciers, e.g., those in the Tibetan Plateau and the Canadian Rocky Mountains, are extremely important water reservoirs providing freshwater throughout the world [Schindler and Donahue, 2006; Kehrwald et al., 2008; Immerzeel et al., 2010]. As snowpack and alpine glacier diminish, regions relying on melting

snowpacks and/or glaciers for their water supply are extremely vulnerable with respect to freshwater availability [Barnett et al., 2005; Schindler and Donahue, 2006]. In addition, natural hazards, such as landsides and rock avalanches, and loss of biodiversity are also concerns in alpine stream and river systems [Evans and Clague, 1994; Brown et al., 2007; Mark et al., 2010; Chevallier et al., 2011]. Furthermore, the concerns with respect to water supply do not occur only in regions supplied by melting glaciers. Basaltic islands, e.g., the Island of Maui, Hawaii, typically have complex internal structures and challenging access, are often poorly characterized with respect to groundwater resources and frequently suffer from freshwater scarcity. Maui has particularly extreme variations in both the amounts and the spatial distribution of rainfall, adding to the freshwater shortage problem in some of the most densely populated areas of the island. A previous study in the basaltic Galápagos Islands, suggested that NGTs have the potential to identify the location and timing of recharge in fractured flow systems [Warrier et al., 2012]. Subsequently, noble gases in rainwater samples collected in southeast Michigan were found to be in disequilibrium with the atmosphere at the collection point and noble gas concentration patterns were hypothesized to link to weather patterns [Warrier et al., 2013]. These studies point to the potential of using noble gases dissolved in groundwater in volcanic systems with fast infiltration rates to develop a new NGT application in terms of location and timing of groundwater recharge, as well as characterization of precipitation. In summary, this dissertation focuses on utilizing the complete set of stable noble gases in either glacial meltwater (in Greenland and the Athabasca Glacier) or rainwater and groundwater samples (in Maui) to better understand the local hydrological system in terms of glacier dynamics, water source altitude, water residence times and connectivity of aquifers.

Chapter 2 presents the first comprehensive stable noble gas study in glacial meltwater. Vertical conduits, e.g., crevasses and moulins, from the surface of the glacier to the bottom form preferential flow paths for water melting at the surface when air temperature is above 0°C during a brief period in summer. Water samples were collected in five outlets glaciers of the GrIS from supraglacial lakes, at the terminus area (where subglacial meltwater is discharged), and in rivers downstream from the terminus area. Noble gas concentrations are far from equilibrium with the atmosphere at collection point. A few samples display a unique noble gas pattern of relative Ar enrichment or relative Ne depletion, which was previously observed in a few high altitude springs in the Galápagos Islands [Warrier et al., 2012] and rainwater samples in southeast

Michigan [Warrier et al., 2013]. This study explores the potential of utilizing atmospheric Ne, Ar, Kr, and Xe concentrations to estimate the source altitude of the glacial meltwater samples. A first-order estimate of water resident time is presented in this study by taking advantage of ^{4}He, which is produced in the crust and accumulated in subglacial meltwater.

Chapter 3 represents the first comprehensive stable noble gas study in an alpine glacier. This study of the Athabasca Glacier (AG) of the Columbia Icefield in the Canadian Rocky Mountains follows the same line of the study conducted in the GrIS, which is a continental glacier. Water samples are collected at the terminus area over a period of two months during the peak melting season. This study takes advantage of Xe concentrations to estimate the water source altitudes in an attempt to better understand the dynamics of this alpine glacier. A crustal He component is also observed in subglacial meltwater at AG and a first-order estimate of water resident time suggests that the AG meltwater is up to an order of magnitude younger than that from the GrIS.

Chapter 4 represents the first comprehensive stable noble gas study in the Island of Maui, Hawaii. Maui is a basaltic island with preferential flow pathways because of the presence of dykes and fractures [e.g., Gingerich, 1999a; 1999b]. Warrier et al. [2012] suggested that noble gas concentrations in these fractured hydrologic systems do not represent the mean annual air temperature (MAAT) as observed in sedimentary basins. This study further explores the information noble gases can provide in rapid rainwater infiltration systems. It assesses whether NGTs can be applied to these systems to estimate the location of recharge and explores the relative contributions of different water sources. This study also discusses the usage of noble gases in investigating connectivity between aquifers.

Chapter 5 represents a follow-up study to Chapter 4. This study focuses on exploring whether noble gases and water stable isotopes preserve temporal changes in the basal and perched aquifers. It assesses the potential of using a combined dataset of noble gases and stable isotopes to constrain the type of water sources and water source altitudes. Water residence times of the basal aquifer are estimated based on tritium measurements and estimated ^{3}He concentrations resulting from tritium decay (tritiogenic ^{3}He; $^{3}He_{trit}$).

A summary of the major results and conclusions of this dissertation and potential future research focuses are provided in Chapter 6. This dissertation has important societal relevance in regions with fractured, fast infiltration hydrologic systems. Results in chapters 2 and 3 can

contribute to a better understanding of the dynamics of both continental and alpine glaciers. Results in chapters 4 and 5 contribute to a better understanding of the hydrogeology of regions that suffer from freshwater scarcity due to uneven spatial and temporal distribution of precipitation and can lead to improved water resource management plans in these areas. This dissertation has important scientific implications in the fields of glaciology, hydrogeology, and meteorology.

CHAPTER II

Noble gas signatures in Greenland: Tracing glacial meltwater sources[1]

Abstract

This study represents the first comprehensive noble gas study in glacial meltwater from the Greenland Ice Sheet. It shows that most samples are in disequilibrium with surface collection conditions. A preliminary Ne and Xe analysis suggests that about half of the samples equilibrated at a temperature of ~0°C and altitudes between 1 km and 2 km, with a few samples pointing to lower equilibration altitudes and temperatures between 2°C and 5°C. Two samples suggest an origin as melted ice and complete lack of equilibration with surface conditions. A helium component analysis suggests that this glacial meltwater was isolated from the atmosphere prior to the 1950s, with most samples yielding residence times ≤ 420 years. Most samples represent a mixture between a dominant atmospheric component originating as precipitation and basal meltwater or groundwater, which has accumulated crustal ^{4}He over time.

[1]Citation: Niu, Y., Castro, M. C., Aciego, S. M., Hall, C. M., Stevenson, E. I., Arendt, C. A., and Das, S. B. (2015). Noble gas signatures in Greenland: Tracing glacial meltwater sources. *Geophys. Res. Lett.*, *42*, 9311–9318, doi:10.1002/2015GL065778.

2.1 Introduction

The study of noble gases (He, Ne, Ar, Kr, and Xe) dissolved in groundwater can enhance our understanding of surface and groundwater dynamics by providing us with an indication about flow paths, connectivity between aquifers, and water residence times [e.g., Andrews, 1985; Mazor and Bosch, 1992; Castro et al., 1998a, 1998b; Patriarche et al., 2004; Castro et al., 2007]. In addition, because noble gases are conservative tracers and their concentrations in the recharge areas of groundwater systems are typically considered to be simply a function of temperature (T), pressure (P) (altitude of recharge area), and excess air (EA), noble gas temperatures (NGTs) have commonly been regarded as a potentially robust indicator of past climate [Stute and Schlosser, 1993; Ballentine and Hall, 1999; Aeschbach-Hertig et al., 2002; Kipfer et al., 2002; Sun et al., 2010; Castro et al., 2012].

Although noble gas studies have been carried out extensively in ice-free regions, studies of noble gases in glacial environments remain particularly scarce [e.g., Craig and Wiens, 1996; Severinghaus and Battle, 2006; Malone et al., 2010]. High-latitude regions such as Greenland are extremely sensitive to and are significant drivers of climate change due to the enormous water masses they store. Understanding climate shifts in the Greenland Ice Sheet (GrIS) margins is even more critical as these areas may be particularly sensitive to global climate forcing [Intergovernmental Panel on Climate Change, 2013]. The GrIS has been extensively studied to estimate its ice melting and acceleration rates [Rignot et al., 2011], as well as its contributions to sea level rise [Zwally et al., 2005; Shepherd and Wingham, 2007; Rignot et al., 2011]. However, many questions remain to be answered pertaining to the dynamics and seasonality of the GrIS [Das et al., 2008; Joughin et al., 2008], sources and composition of the meltwater, as well as temperature changes in GrIS and their driving mechanisms [Hanna and Cappelen, 2003; Chylek et al., 2006].

Here, we present a pilot noble gas study of GrIS glacial meltwater. This study explores the information noble gases can provide in glacial environments with respect to glacial meltwater sources, relative source contributions, water residence times, and locations where this glacial meltwater originates within the ice sheet. Ultimately, we seek to improve our understanding of the dynamics of these massive ice sheets, critical for the major role they play in climate change. This is possible due to the conservative nature of noble gases and the temperature dependency of their concentrations in equilibrated air saturated water (ASW), allowing for calculation of NGTs

and, under certain assumptions, estimation of the altitude at which glacial meltwater originated. In addition, crustally produced isotopes such as ^{4}He accumulate in water over time, allowing for a first-order estimation of water residence times.

2.2 Geologic, Glaciologic, and Climatologic Background

Greenland is located between the Arctic and Atlantic Oceans, northeast of Canada, and is covered by the GrIS. The Summit in central Greenland is 3231 m above sea level (asl); in southern Greenland, the highest elevation is 2873 m asl (Figure 2.1) [Bamber, 2001]. The geology of the current ice-free margin has been extensively studied [e.g., Baadsgaard, 1973; Friend and Nutman, 2005; Hollis et al., 2006; Dawes, 2009]. Most of the bedrock is Precambrian shield and is mainly composed of granitic gneiss and granitoids [Dawes, 2009].

Mean annual air temperatures range from – 5°C to 2°C at our sampling locations (Figure 2.1). Average summer (June, July, and August) and winter (December, January, and February) temperatures observed within sea level to 100 m asl range from 5°C to 10°C and from – 18°C to – 4°C, respectively [Vinther et al., 2006; Hanna et al., 2012] (Danmarks Meteorologiske Institut, http://www.dmi.dk/groenland/arkiver/vejrarkiv/, 2014). Summer temperatures allow for surface melting to occur during a brief period.

2.3 Sampling and Analytical Methods

Thirteen samples for noble gas analyses were collected at five locations at or near the coast of central and southern Greenland (Figure 2.1; Table 2.1) in July and August 2013, at or slightly after the peak of the summer melting season. These include eight subglacial (terminus) meltwater, three surface meltwater, and two river water samples. Samples were collected at altitudes between 0 and 1221 m asl with water collection temperatures ranging from 0°C to 2.8°C. Water samples were collected in standard refrigeration grade 3/8” copper tubing. All samples were analyzed at the Noble Gas Laboratory at the University of Michigan on a MAP-215 mass-spectrometer following procedures described in Castro et al. [2009] and Hall et al. [2012].

2.4 Conceptual GrIS GMW Model: Implications for Noble Gases

Figure 2.2 illustrates a conceptual model of the GrIS glacial hydrology near the terminus

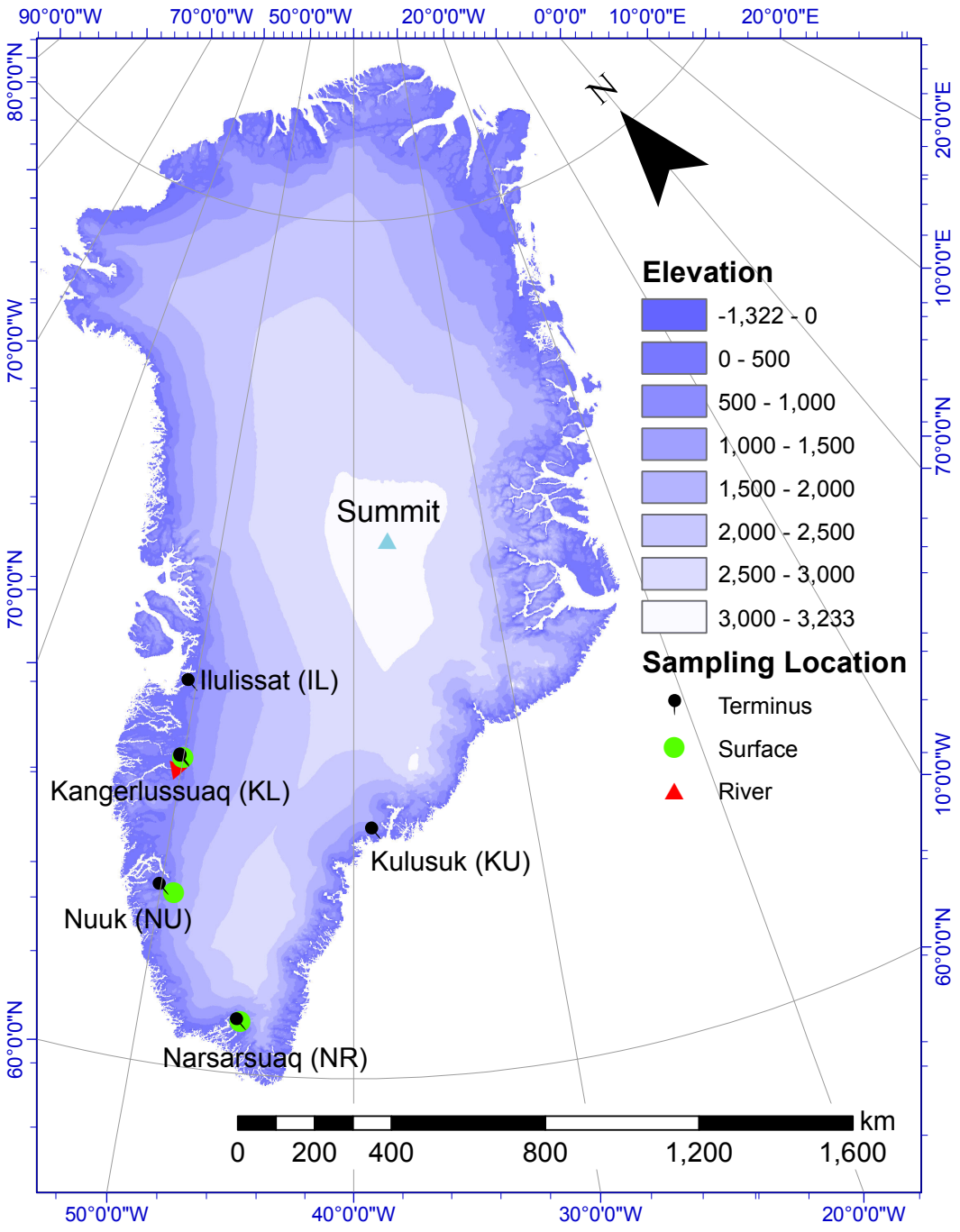

Figure 2.1 Map of Greenland [Modified from Bamber, 2001]; sampling locations and type of samples collected are indicated.

Table 2.1 Sampling locations, sample type, measured water temperatures and noble gas concentrations[1], R/R_a, and R_{exc}/R_a values[2].

Sample type and number	Location	Longitude (West)	Latitude (North)	Elevation (m)	Water Temperature (°C)	He 10^{-8} cm^3 STP g^{-1}	Ne 10^{-7} cm^3 STP g^{-1}	Ar 10^{-4} cm^3 STP g^{-1}	Kr 10^{-8} cm^3 STP g^{-1}	Xe 10^{-9} cm^3 STP g^{-1}	R/R_a ($\pm1\sigma$)	R_{exc}/R_a ($\pm1\sigma$)
Terminus												
NR-T1	Narsarsuaq	45°19.765'	61°12.466'	25	1.1	33.80	2.53	5.19	11.56	15.90	0.25 (0.01)	0.09 (0.02)
IL-T1	Ilulissat	50°22.957'	68°53.851'	10	0.0	6.42	1.74	4.31	10.05	14.82	0.78 (0.02)	0.05 (0.08)
KL-T1	Kangerlussuaq	50°03.549'	67°08.144'	417	0.0	6.62	2.25	4.78	11.50	17.40	0.91 (0.02)	0.63 (0.31)
KL-T2	Kangerlussuaq	50°03.527'	67°08.147'	406	0.1	7.09	1.41	3.28	7.18	9.06	0.67 (0.01)	0.03 (0.05)
NU-T1	Nuuk	49°57.123'	64°06.167'	176	0.0	21.09	2.75	5.76	12.39	17.21	0.41 (0.01)	0.15 (0.05)
NU-T2	Nuuk	49°57.123'	64°06.167'	176	0.0	6.73	1.91	4.75	11.42	16.88	0.75 (0.01)	0.12 (0.06)
KU-T1	Kulusuk	38°27.524'	65°42.597'	0	0.3	6.23	1.95	5.19	12.48	19.43	0.83 (0.02)	0.21 (0.10)
KU-T2	Kulusuk	38°27.524'	65°42.597'	0	0.3	5.79	1.91	4.64	10.84	15.81	0.90 (0.02)	0.36 (0.16)
Surface												
NR-S1	Narsarsuaq	45°18.243'	61°13.347'	71	0.1	6.68	2.25	3.81	8.60	11.99	0.92 (0.01)	0.41 (0.16)
KL-S1	Kangerlussuaq	50°02.154'	67°08.961'	513	0.0	5.41	1.90	4.68	11.32	17.53	0.86 (0.02)	0.05 (0.14)
NU-S1	Nuuk	49°18.269'	64°00.367'	1221	0.2	5.59	1.74	4.19	9.87	14.49	0.88 (0.02)	0.51 (0.09)
River												
KL-R1	Kangerlussuaq	50°56.843'	66°57.958'	122	2.8	8.03	1.87	4.66	10.73	16.48	0.67 (0.02)	0.17 (0.05)
KL-R2	Kangerlussuaq	50°16.599'	67°04.634'	248	2.6	5.32	1.90	4.79	11.10	17.07	1.06 (0.06)	1.54 (0.60)

[1]Measurement errors of noble gas concentrations are 1.5%, 1.3%, 1.3%, 1.5%, and 2.2% for He, Ne, Ar, Kr, and Xe, respectively.
[2]Helium isotope ratios, $R = {}^3He/{}^4He$, are normalized by the atmospheric value of $R_a = 1.384 \times 10^{-6}$ [Clarke et al., 1976].

area [Martinerie et al., 1992, 1994; Skidmore et al., 2005; Das et al., 2008; Cuffey and Paterson, 2010]. Water starts as melted snow or firn at the surface, in contact with air. Partial noble gas equilibration may occur both at the surface (area a in Figure 2.2) and at the terminus area (area c in Figure 2.2). Exposure of surface GMW to the atmosphere varies between hours and weeks, where an ASW component forms. For example, the formation of a supraglacial lake over ~3–4 weeks was observed followed by massive and sudden drainage lasting ~1.4 h at an average rate of 8700 m^3/s [Das et al., 2008]. EA is likely incorporated in GMW as water is fiercely transported through vertical conduits (crevasses and moulins), similar to the EA component present in sedimentary systems resulting from air bubbles trapped due to rapid water table fluctuations [Heaton and Vogel, 1981]. The meltwater discharged at the base of the glacier is likely a combination of surface melting routed through moulins and basal melt which has interacted with subglacial till and bedrock [Jean-Baptiste et al., 2001; Skidmore et al., 2005]. Trapped air in ice, which has a composition nearly indistinguishable from that of EA, can also be incorporated into the subglacial meltwater. This was observed by earlier studies of noble gases in ice cores and seawater affected by the submarine melting of ancient glacial ice [e.g., Schlosser, 1986; Schlosser et al., 1990; Martinerie et al., 1992, 1994; Weppernig et al., 1996; Hohmann et al., 2002; Loose and Jenkins, 2014]. However, its contribution is expected to be minor, following the local hydrologic conceptual model for the GrIS GMW (Figure 2.2). The noble gas signature revealed by our samples supports this conceptual model (cf., section 2.5).

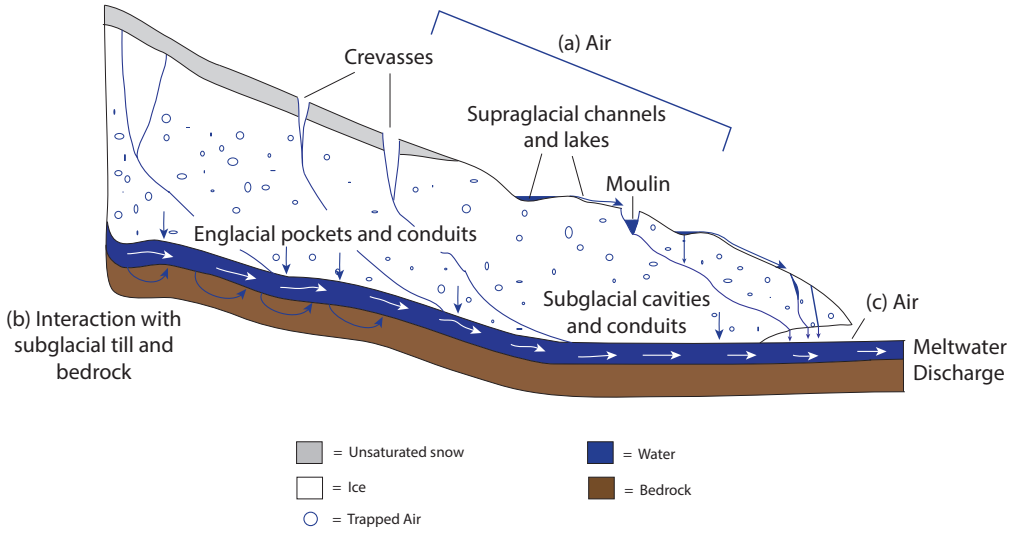

Figure 2.2 Conceptual model of glacial hydrology near the terminus area.

2.5 Results

Figure 2.3a displays noble gas concentrations of our samples normalized to those in 0.09 cm^3 of air per gram of ice, i.e., the expected trapped air in glacial ice [e.g., Martinerie et al., 1992, 1994]. It is apparent that our samples are heavily depleted in Ne and present an extreme Xe enrichment when compared to trapped air in ice. These measured concentrations contrast highly with those of trapped air in ice and suggest that the bulk of our GrIS GMW is not derived directly from the melting of old glacial ice in absence of atmospheric contact. Figure 2.3b displays noble gas concentrations normalized to the ASW corresponding to measured water temperature and altitude at collection points. With the exception of He, for which buildup of radiogenic ^{4}He is observed, and in contrast to trapped air in ice, it is apparent that most samples display a pattern close to that of ASW. This suggests that an ASW component largely dominates over any possible EA component, including one originating from trapped air in glacial ice for the four heavier noble gases. EA can be incorporated both during rapid transport through vertical conduits and from melted old glacial ice. The composition of these EA components are nearly identical.

From Figures 2.3b and 2.3c, it is apparent that for all GrIS GMW samples, noble gas concentrations do deviate somewhat from expected ASW values ($C/C_{ASW} = 1$) corresponding to

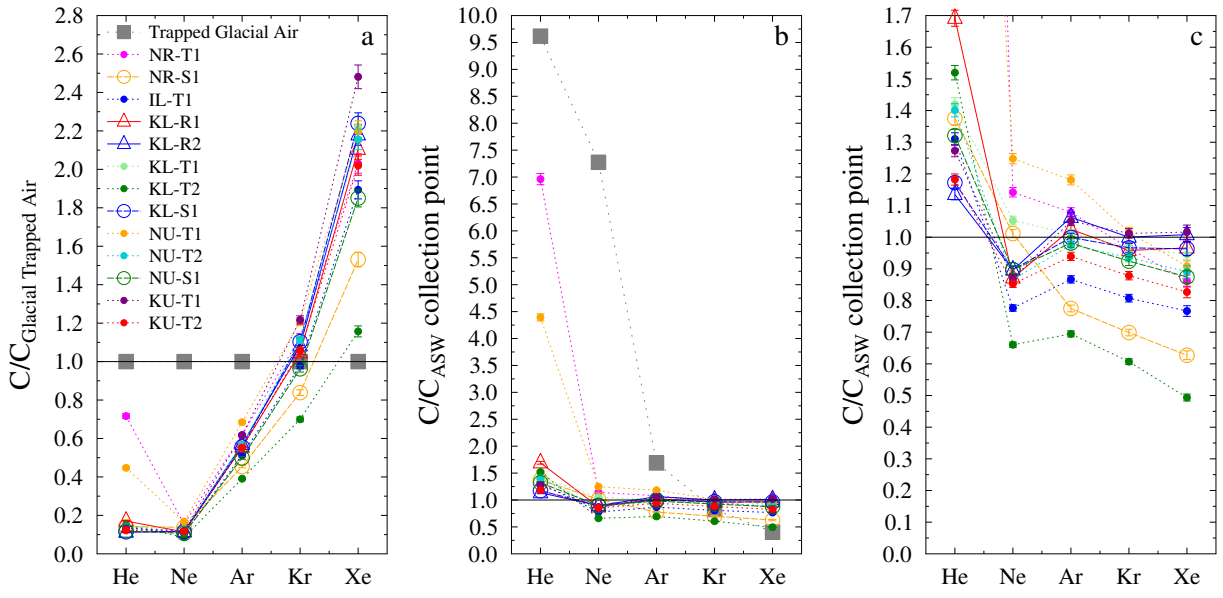

Figure 2.3 Measured noble gas concentrations normalized to (a) trapped air in glacier ice or (b and c) ASW at collection temperatures and altitudes. The solid black line indicates noble gas concentrations with no addition or loss of gases compared to trapped air in glacier ice or ASW. All samples (Figure 2.3b). Zoomed into 0 – 1.7 on the vertical axis (Figure 2.3c).

measured water temperature and altitude at collection points (Figures 2.3b and 2.3c and Table 2.1). All samples display He excesses with respect to ASW values (Figure 2.3b). Two terminus samples (NR-T1 and NU-T1) display, by far, the highest excesses, with values up to 596% and 339% that of ASW, respectively (Figure 2.3b). All other samples display excesses varying between 14% and 69% that of ASW. The origin and respective fractions of these He excesses are constrained by R/R_a values, where R is the measured $^3He/^4He$ ratio and R_a is the atmospheric value of 1.384×10^6 [Clarke et al., 1976]. All samples but KL-R2 display $R/R_a < 1$ (Table 2.1), pointing to the presence of a crustal He source ($0.02 \leq R_c/R_a \leq 0.05$) [e.g., O'Nions and Oxburgh, 1983] with a strong negative correlation between R/R_a values and total He concentrations (Figure 2.4). A decreasing trend of R_{exc}/R_a from atmospheric to crustal values with increased total He

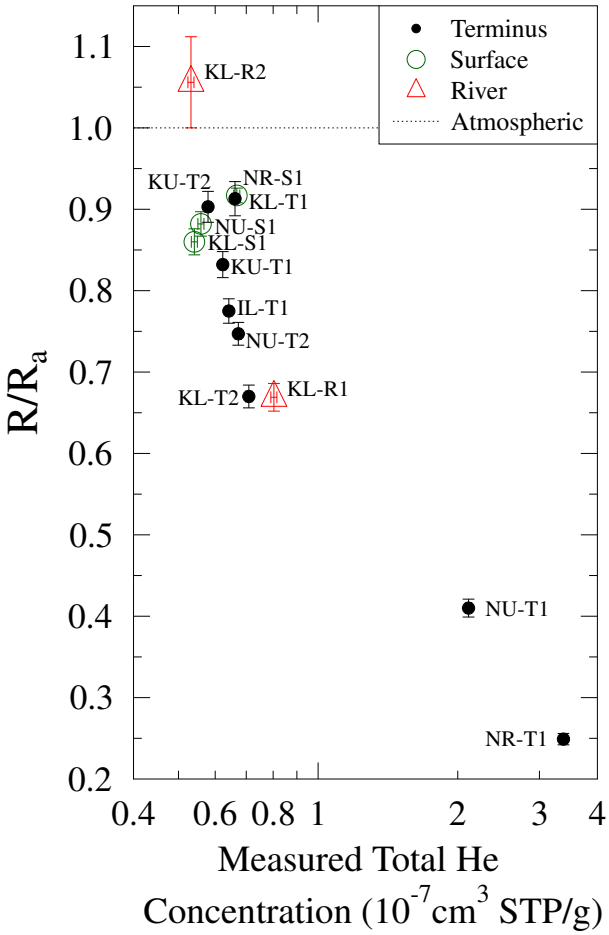

Figure 2.4 Measured R/R_a values versus total He concentrations, indicating negative correlation between R/R_a values and He concentrations.

and $^4He_{exc}$ concentrations (where R_{exc} and $^4He_{exc}$ are the $^3He/^4He$ ratios and ^4He concentrations from which the atmospheric component was removed, respectively) [e.g., Castro, 2004] is also observed. This strongly suggests that ^4He excesses are dominated by ^4He crustal production, which allows, under certain assumptions, for subsequent calculation of GMW residence times (cf., section 2.6.2). In contrast to He, Ne, Kr, and Xe concentrations for most samples are depleted with respect to ASW, while six samples are also depleted in Ar (Figures 2.3b and 2.3c). Five samples are enriched in Ar up to a maximum of 18%, while two samples display expected ASW values with respect to collection point conditions. While Ne concentrations display a maximum depletion of 34%, Ar, Kr, and Xe display maximum depletions of 31%, 39%, and 51% with respect to ASW at collection altitudes and measured water temperatures. Deviations of measured concentrations from ASW values at collection point suggest an apparent lack of equilibration of GrIS melt- water with surface conditions (cf. section 2.6.1). The presence of two patterns in our samples is apparent. One group displays a mass-dependent depletion pattern with stronger depletion of the heavier noble gases compared to the lighter ones. This group consists of three terminus samples (NR-T1, KL-T1, and NU-T1) and one surface sample (NR-S1). Of these, three samples present Ne excesses, while sample NR-S1 displays the expected ASW Ne concentration. The second group displays a relative Ne depletion with respect to Ar, Kr, and Xe. This group includes nine samples of all three types, i.e., terminus, surface, and river samples. All samples in this group display Ne depletion with respect to ASW values at collection point conditions. As Ar, Kr, and Xe in GrIS GMW follow the mass-dependent depletion pattern for most samples, we refer here to this pattern as a relative Ne depletion as opposed to the relative Ar enrichment identified in previous studies [Warrier et al., 2012, 2013]. All Ne, Ar, Kr, and Xe isotopic ratios are indistinguishable from ASW values. In their study of springs in the Galápagos Islands, Warrier et al. [2012] hypothesized that this mass- independent pattern is likely due to mixing between low-altitude (<~400m) fog droplets and high-altitude precipitation. Fog was present in Greenland during two of our sampling days, and Bergin et al. [1994] have also reported the presence of fog at the Summit.

2.6 Discussion

2.6.1 Equilibration Temperatures and Altitudes

Concentrations of atmospheric noble gases dissolved in water record various physical

parameters (e.g., temperature, EA, and altitude) at which final equilibration with the atmosphere takes place. Assuming that both Ne and Xe are in equilibrium with the atmosphere, it is possible to compare 1/Xe versus Ne/Xe to estimate an initial range of temperatures and altitudes of equilibration for our GrIS GMW samples [Warrier et al., 2012]. This is achieved by comparing measured Ne and Xe concentrations along with loci of calculated expected values for ASW for

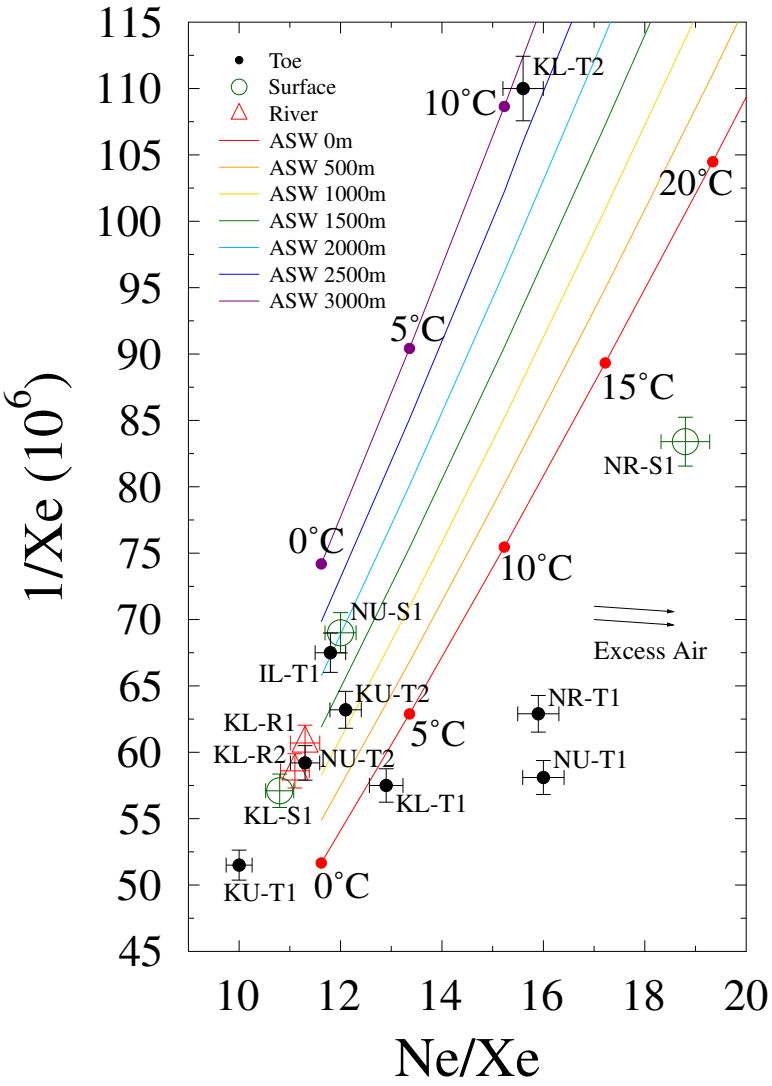

Figure 2.5 Preliminary estimation of equilibration temperatures and altitudes under the assumption that both Ne and Xe have equilibrated with surface conditions by comparing measured 1/Xe versus Ne/Xe for all Greenland samples with theoretical ASW values. Colored lines indicate ASW values at altitudes between 0 and 3000 m asl, and colored markers indicate temperatures between 0°C and 20°C. EA addition moves samples in the direction indicated by arrows.

altitudes and temperatures varying between 0 and 3000 m asl and between 0°C and 20°C, respectively (Figure 2.5). Such a plot suggests that six samples (IL-T1, KL-R1, KL- R2, NU-T2, NU-S1, and KU-T2) have nearly equilibrated with the atmosphere at ~0°C and at altitudes varying between 1 km and 2 km, values which are consistent with both temperatures and elevations in Greenland and, in particular, in our study area. In contrast, sample KL-T2, a terminus sample collected at 406 m at Kangerlussuaq (Figure 2.1), points to a significantly higher equilibration elevation, between 2500 m and 3000 m, and an apparent equilibration temperature of 11°C. This temperature is far too high and inconsistent with temperatures in the area and points to a lack of water equilibration with surface conditions. It is possible that the concentrations of the heavier noble gases and that of Xe in particular, which are extremely low in sample KL-T2, are due to ice formation at higher altitudes rather than the apparently high equilibration temperature. Indeed, due to their large atomic radii, Ar, Kr, and Xe tend to be excluded from the ice structure [Top et al., 1988; Malone et al., 2010]. Low heavy noble gas concentrations in precipitation have previously been observed and associated with ice formation at high altitudes [Warrier et al., 2013]. Sample KL-T2 is likely to be melted ice that has not equilibrated with the atmosphere. In addition, samples KL-S1 and KU-T1 point to temperatures below freezing, which can be identified through their Ne depletion and/or Xe excess. On the other hand, samples NR-T1, NR-S1, KL-T1, and NU-T1 suggest the presence of EA as revealed by their excess Ne (Figure 2.2). Any addition of EA to a sample moves it toward the bottom-right following the arrows indicating EA. In order to estimate the higher limit of equilibration temperature, the sample may be moved toward the up-left parallel to the EA arrows by a certain amount to its collection altitude, without knowledge of the exact amount of EA present in the sample. The equilibration altitude is always higher than or equal to the collection altitude; therefore, when a sample is moved to its collection altitude, its maximum equilibration temperature can be estimated. This process of removing EA will lead to lower apparent equilibration temperatures and higher apparent equilibration altitudes. More specifically, this leads to maximum equilibration temperatures of ~5°C, 2°C, and 3°C for samples NR-T1, KL-T1, and NU-T1, temperatures, which are consistent with conditions on the ground. Sample NR-T1 was collected at 25 m asl, very close to the observation site at Narsarsuaq [Vinther et al., 2006; Hanna et al., 2012], with a summer mean surface air temperature of ~10°C [Hanna et al., 2012]. Samples KL-T1 and NU-T1 were collected at 417 m asl and 176 m asl, respectively, at relative

proximity to the observation site altitudes at Kangerlussuaq and Nuuk, respectively [Vinther et al., 2006; Hanna et al., 2012]. It is also possible for the equilibration temperature suggested by samples KL-T1 and NU-T1 to be compatible with the surface conditions. In contrast, sample NR-S1, collected at 176m asl at Narsarsuaq, points to an equilibration temperature of ~13°C, assuming equilibrium at collection altitude. Similarly to sample KL-T2, this temperature is too high to be compatible with surface conditions in Greenland and suggests an ice origin, possibly melted ice that did not equilibrate with the atmosphere.

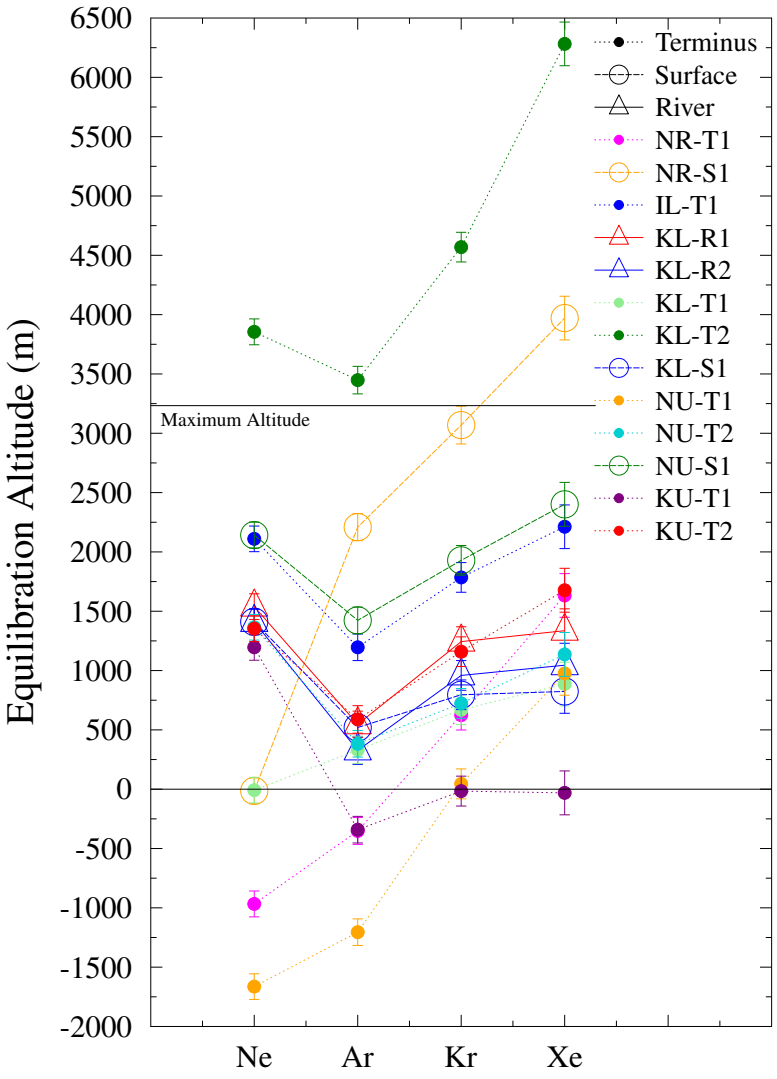

Figure 2.6 Equilibration altitudes based on single gas concentrations assuming equilibration at 0°C. The black solid lines indicate the elevation interval physically possible based on Greenland topographic surface.

If equilibration for all noble gases is not warranted, as appears to be the case for at least some of our GrIS samples, examining each gas separately is necessary. Because Xe requires the longest equilibration times, it will provide us with the most reliable original equilibration altitudes. To determine equilibration altitudes based on each single noble gas, an equilibration temperature of 0°C was assumed for all samples (Figure 2.6).

Overall, it is apparent from Figure 2.6 that 10 samples out of 13 yield Xe equilibration altitudes ranging from 820m to 2400m, an altitude interval that overlaps with that derived from Figure 2.5, but which is larger. Because the equilibration temperature is set at 0°C, higher apparent equilibration temperatures are equivalent to higher altitudes at lower temperatures. In particular, sample KL-T2 points to very high Ar, Kr, and Xe equilibration altitudes, which are higher than the highest elevation in Greenland. This reinforces the notion that sample KL-T2 is likely to have formed directly from ice and has not equilibrated with the atmosphere, as was previously discussed. Similarly, the Xe equilibration altitude of sample NR-S1, 4000 m, is also incompatible with conditions on the ground, pointing to melted ice that has not equilibrated with the atmosphere. However, Ar and Kr equilibration altitudes are compatible with Greenland topography and suggest that sample NR-S1 has reached a greater level of partial equilibration with the atmosphere than sample KL-T2. This sample's Ne equilibration altitude is approximately that of collection altitude and suggests that Ne equilibrated with the atmosphere at the time of collection. This, however, assumes the absence of EA. Three samples, KL-R1, KL-R2, and KL-S1, each shows very close Kr and Xe equilibration altitudes, which are also higher than their collection altitudes, suggesting that Kr has just started to equilibrate with surface conditions which are distinct from those at the water source, while Xe is still recording original water source altitudes. Xe equilibration altitude is higher than the collection altitude for sample KL-S1, suggesting that there is no Xe excess, and the apparent subfreezing temperature in Figure 2 is solely due to Ne depletion. On the other hand, Kr and Xe of sample KU-T1 have equilibrated with surface conditions at the collection point, preventing identification of this water's original source. Similar to sample KL-S1, its anomalously low Ne concentration, shown as high equilibration altitude in Figure 2.6, causes the apparent subfreezing temperature in Figure 2.5. Three samples, NR-T1, KL-T1, and NU-T1, yield Ne equilibration altitudes at or below sea level and thus below their collection altitudes, suggesting the presence of Ne excess resulting from EA.

As Ne concentration is greatly affected by the EA component, a negative EA component or a degassing process may be required to explain the observed Ne depletion. Bubbles that form in water under pressure and subsequently escape from the water phase are likely to preferentially lower Ne concentrations dissolved in water. Warrier et al. [2012] hypothesized that higher pressures in fog droplets cause lower noble gases solubilities in fog than the surrounding air. Due to Ne's higher diffusivity, Ne is more sensitive to pressure differences than the heavier noble gases, resulting in lower Ne concentrations relative to heavier noble gases. Subsequent mixing of the fog with ASW components might lead to Ne depletion. This process could partially explain the relative Ne depletion and Ar enrichment observed in some of our samples.

2.6.2 Sources and Residence Times of GrIS Meltwater

It is possible to separate and quantify the different He components, i.e., atmospheric, crustal, and/or mantle to identify different water sources, i.e., precipitation as rain, snow, or ice versus groundwater. Estimation of the crustal He component subsequently allows estimation of groundwater residence times under certain simplifications and assumptions. This analysis is typically done by plotting R_{noea}/R_a versus $^4He_{eq}/^4He_{noea}$, where R_{noea} and $^4He_{noea}$ are the $^3He/^4He$ ratios and total measured ^4He concentration at collection conditions after removal of EA and $^4He_{eq}$ is the ASW ^4He concentration under collection conditions (Figure 2.7) [Castro, 2004] (Appendix A1). From Figure 2.7, it is apparent that two terminus samples, NR-T1 and NU-T1, are dominated by crustal ^4He. These samples have crustal contributions of 84.4% and 74.0%, minor mantle contributions of 0.7%–1.2%, and likely pre-modern atmospheric contributions of 14.9% and 24.8%, respectively, as indicated by a complete absence of tritiogenic ^3He. Alternatively, 10 tritium unit (TU) could be considered in the absence of a mantle component. However, due to the significant amounts of crustal ^4He in these samples, this scenario is unlikely as 10 TU would correspond to modern water, which cannot have built up ^4He. Indeed, measurements of tritium levels in Greenland precipitation in 2009 show an annual average value of 11 TU (International Atomic Energy Agency, https://www.univie.ac.at/cartography/project/wiser/, 2012). All other samples are dominated by an ASW component with $^3He_{trit}$ levels varying between 0 TU and 5 TU, lower than modern average tritium values (Figure 2.7). The very low $^3He_{trit}$ levels suggest that (1) our glacial meltwater samples have been isolated from contact with the atmosphere since before the bomb-

test era, i.e., prior to the 1950s or (2) samples are very young so tritium has not yet decayed. Our first-order glacial meltwater residence time estimation based on $^4He_{exc}$ concentrations, together with estimated ^4He production rates in basement rocks and ^4He accumulation rates in water (Appendix A2), supports scenario 1, as very young water would not have accumulated radiogenic ^4He from contact with bedrock. Based on excess ^4He concentrations and ^4He production rates, maximum and minimum water residence times were calculated (Table 2.2;

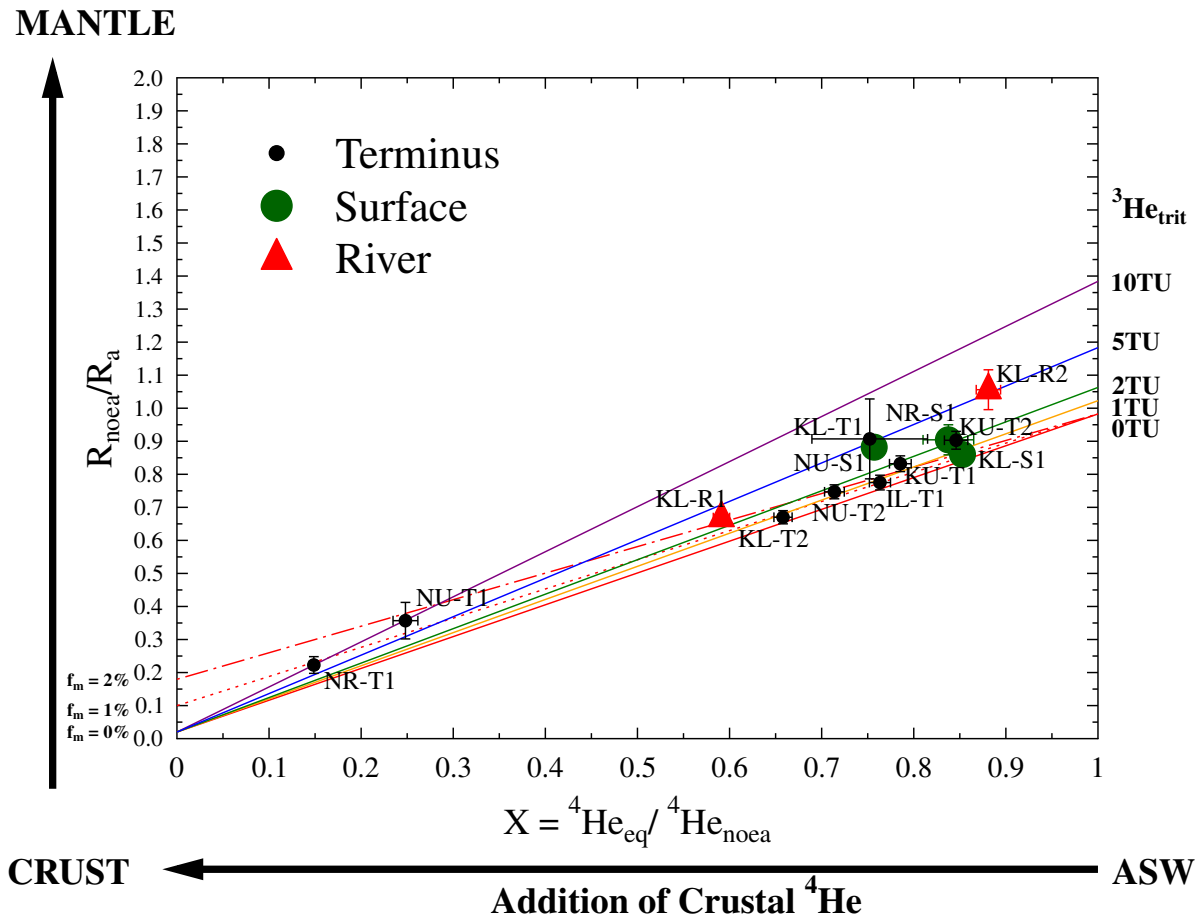

Figure 2.7 Helium component separation. Colored lines indicate expected position for samples with tritiogenic ^3He levels varying from 0 to 10 TU and percentages of mantle component in the non-ASW sources varying between 0% and 2%. The terms f_m noted along the left vertical axis indicate mantle contributions to the He in the sums of crustal and mantle sources. End-members used for crust and mantle components are 0.02 and 8 times the atmospheric value, respectively. The x coordinate indicates the fraction of He contributed by ASW. The total contributions of crustal and mantle source are calculated by subtracting the x coordinates from 1, denoted as $(1 - X)$. Mantle contribution to the whole sample is the corresponding f_m multiplied by $(1 - X)$.

Table 2.2 Water residence times calculated based on $^{4}He_{exc}$ and U-series measurement (Arendt, 2015). Ages are reported in years with 1σ errors in parentheses, expect the U-series age, where 2σ errors are reported.

Sample Type and Number	Location	$^{4}He_{exc}$ (10^{-8} cm^{3} STP g^{-1})	+/-	Minimum Age	Maximum Age	Average Age	U-series Age
Ternimus							
NR-T1	Narsarsuaq	27.8	0.73	2800 (100)	4400 (100)	3600 (100)	1074 (193)
IL-T1	Ilulissat	1.52	0.01	150 (10)	240 (20)	200 (10)	12 (1)
KL-T1	Kangerlussuaq	1.54	0.43	160 (40)	240 (70)	200 (40)	
KL-T2	Kangerlussuaq	2.43	0.11	250 (10)	380 (20)	310 (10)	
NU-T1	Nuuk	14.6	0.80	1500 (100)	2300 (100)	1900 (100)	266 (54)
NU-T2	Nuuk	1.92	0.10	190 (10)	300 (20)	250 (10)	
KU-T1	Kulusuk	1.34	0.09	140 (10)	210 (10)	170 (10)	203 (35)
KU-T2	Kulusuk	0.89	0.09	90 (10)	140 (10)	110 (10)	
Surface							
NR-S1	Narsarsuaq	0.94	0.13	95 (14)	150 (20)	120 (10)	
KL-S1	Kangerlussuaq	0.80	0.08	80 (8)	120 (10)	100 (10)	
NU-S1	Nuuk	1.36	0.08	140 (10)	210 (10)	180 (10)	
River							
KL-R1	Kangerlussuaq	3.28	0.12	330 (10)	510 (20)	420 (10)	

Appendix A2). Average ^{4}He water ages were also estimated (Table 2.2; Appendix A2). It should be noted that these age estimations yield simply a first estimation for the GMW. Although most samples display residence times between 100 years and 420 years, terminus samples NR-T1 and NU-T1 display significantly older ages of 3600 years and 1900 years, respectively. These residence times further support the notion that the ice from which these samples originated was isolated from the atmosphere prior to the 1950s. Highly variable calculated ages reflect the dominance of various contributions and origins for different samples, in particular, the presence of an older crustal versus a younger atmospheric component.

Residence times for four locations based on U-series (^{222}Rn, ^{238}U, and $^{234}U/^{238}U$) measurements are listed in Table 2.2 (Arendt, 2015). Estimates based on both sets of tracers are the same order of magnitude at Narsaruaq and Kulusuk. One of the two noble gas samples yields s similar age estimate to the U-series age, while the other sample yields an age about an order of

magnitude higher. The residence time estimate at Ilulissat based on He is also about an order of magnitude higher than that based on U-series.

Overall, the atmospheric component dominates, with most samples displaying an atmospheric ASW contribution of ~59% – 88% and a crustal contribution of ~12% – 41%. This suggests that at least 59% – 88% of the water is from precipitation as liquid, snow, or ice, with the remainder being meltwater either from the base of the ice sheet that has accumulated ^{4}He over time or directly from groundwater moving upward, a process commonly observed in crystalline, fractured systems. Processes such as upward He diffusion are not considered, rendering these fractions representative of lower limits, and they may be underestimated. The two terminus samples with ~84% and ~74% crustal ^{4}He suggest that much of this water is from basal melt or groundwater that has accumulated crustal ^{4}He for a much longer time period, with possibly additional mantle He. Mixing of groundwater with basal meltwater will lead to overestimated basal meltwater residence times and older apparent ages.

2.7 Acknowledgments

We thank Dr. Kim Cobb for the editorial handling of the manuscript, as well as Dr. Peter Schlosser and two anonymous reviewers for their thoughtful and constructive reviews. Financial support by the University of Michigan, the Packard Foundation, and the Department of Earth and Environmental Sciences Turner fellowship at the University of Michigan awarded to E.I. Stevenson is greatly appreciated.

CHAPTER III

Characterizing glacial meltwater sources in the Athabasca Glacier, Canada, using noble gases as tracers[1]

Abstract

This study is the first comprehensive noble gas study in meltwater of an alpine glacier. It uses stable noble gases' (He, Ne, Ar, Kr, and Xe) concentrations and isotopic ratios from the Athabasca Glacier meltwater (AGMW), Canada, in an attempt to identify the original source location of ice melt and the relative contributions of modern surface melt versus basal melt and/or groundwater. It also estimates first order water residence times of the glacial meltwater (GMW) resulting from a mixture of modern surface and basal melt and/or groundwater. Two patterns are apparent with respect to noble gas concentrations: 1) a mass-dependent depletion pattern with stronger depletion of the heavier noble gases compared to the lighter ones, and 2) a pattern displaying a relative Ne depletion with respect to Ar. Ratios of noble gas concentrations suggest that different gases have different degrees of equilibration and samples are far from equilibration with the atmosphere at any temperature compatible with the glacial environment. Xe concentrations alone suggest that all AGMW samples equilibrated with the atmosphere at altitudes between 2.5 and 3.4 km, altitudes that lie within the altitude range (1.9 – 3.5 km) of the Columbia Icefield. Most samples display Xe equilibration altitudes above the maximum altitude of the AG (~2.7 km), suggesting that a significant portion of the current AGMW originates in the Columbia Icefield that contributes to both the AG per se and current subglacial meltwater discharge. All AGMW samples are largely dominated by surface melt as opposed to basal melt with surface melt representing at least 71% – 96% of the total GMW. Basal melt and/or groundwater represent at most 4% – 29% of the total GMW. All AGMW samples exhibit tritiogenic ^3He ($^3He_{trit}$) levels varying between 0 and 12 TU. Based on estimated $^3He_{trit}$ levels, ^4He concentrations, and average U and Th concentrations in carbonates, we conclude that the bulk of our AGMW is likely a mixture between pre-bomb and present time GMW with a most

likely average residence time of 160 ± 5 years with the exclusion of one present day sample.

[1]Citation: Niu, Y., Castro, M. C., Hall, C. M., Aciego, S. M., and Arendt, C. A. (2017a). Characterizing glacial meltwater sources in the Athabasca Glacier, Canada, using noble gases as tracers. *Appl. Geochem.*, *76*, 136–147, doi:10.1016/j.apgeochem.2016.11.015.

3.1 Introduction

The study of noble gases (He, Ne, Ar, Kr, and Xe) dissolved in groundwater can enhance our understanding of surface and groundwater dynamics by providing an indication about flow paths, connectivity between aquifers, and water residence times [e.g., Andrews, 1985; Torgersen et al., 1989; Mazor and Bosch, 1992; Stute et al., 1992; Castro et al., 1998a, 1998b; Solomon, 2000; Kulongoski et al., 2003; Carey et al., 2004; Patriarche et al., 2004; Castro et al., 2007; Ma et al., 2009; Pinti et al., 2011]. In addition, because noble gases are conservative tracers and their concentrations in the recharge areas of groundwater systems are typically considered to be simply a function of temperature (T), pressure (P) (altitude of recharge area), and excess air (EA), noble gas temperatures (NGTs) have commonly been regarded as a potentially robust indicator of past climate [Stute and Schlosser, 1993; Ballentine and Hall, 1999; Aeschbach-Hertig et al., 2002; Kipfer et al., 2002; Castro and Goblet, 2003; Kulongoski et al., 2004; Sun et al., 2010; Castro et al., 2012]. Noble gas studies have been carried out extensively in sedimentary basins. However, noble gas studies in glacial environments remain scarce [Craig and Wiens, 1996; Poreda et al., 2004; Severinghaus and Battle, 2006; Malone et al., 2010; Dowling et al., 2014; Niu et al., 2015; Warrier et al., 2015].

Alpine glaciers are extremely important water reservoirs providing freshwater throughout the world. Regions relying on melting snowpacks and/or glaciers for their water supply are more strongly dependent on temperature than local precipitation and are thus extremely vulnerable with respect to freshwater availability as snowpack and glaciers diminish [Barnett et al., 2005]. For example, the Tibetan Plateau and adjacent mountain ranges feed all rivers in Asia with its meltwater from snow or ice being critical to the Indus River recharge while being also very significant to the Brahmaputra River [Immerzeel et al., 2010]. Meltwater also plays a less important but still significant role in the Ganges, Yellow, and Yangtze Rivers, leading to half a billion people being affected by the retreat of the Tibetan Plateau glaciers [Kehrwald et al., 2008; Immerzeel et al., 2010]. Similarly, with the decline in glaciers and snowpacks in the Canadian Rocky Mountains, where all the major rivers in this region originate, Canada's west prairie provinces are facing a water crisis [Schindler and Donahue, 2006]. Tropical glaciers, including those in the central Andes Mountains [Chevallier et al., 2011] are also affected by climate change. With the initial increase in river flow resulting from increasing ice/snow melt, moraine dams, riverbanks, and infrastructures are under threat [Chevallier et al., 2011]. Hazards, e.g.,

landslides and rock avalanches, are likely to be triggered by ice mass loss, increasing the vulnerability of humans and livestock [Evans and Clague, 1994; Mark et al., 2010; Chevallier et al., 2011]. Loss of biodiversity due to retreating glaciers is also a concern in alpine streams [Brown et al., 2007]. It is therefore increasingly important to understand the roles that alpine glaciers play in the global and local hydrological cycle.

Here, we present the first comprehensive noble gas study in meltwater of an alpine glacier. This study represents the second noble gas study of glacial meltwater. The first study was carried out in outlet glaciers of the Greenland Ice Sheet (GrIS) [Niu et al., 2015]. In the present study, we use noble gas concentrations and isotopic ratios in the glacial meltwater from the Athabasca Glacier (AG) in an effort to quantify the relative contributions of modern surface melt versus basal ice melt and to identify the original source location of the ice melt. Ultimately, we seek to constrain the relative contributions of the Athabasca glacial meltwater (AGMW) sources, GMW residence times, and locations where GMW originates within the glacier in an attempt to improve our knowledge of the dynamics of alpine glaciers. This is possible due to the conservative nature of noble gases and the dependency of their concentrations on temperature and ambient air pressure in equilibrated air saturated water (ASW), allowing for estimation of the altitude at which glacial meltwater originated under certain assumptions applicable in the glacial environment. In addition, crustally produced isotopes such as ^{4}He accumulate in water over time, allowing for a first order estimation of water residence times.

3.2 Climatologic and Geological Background

The Columbia Icefield straddles the continental divide in the Canadian Rocky Mountains, on the southern end of Jasper National Park in Alberta, Canada. The AG is one of eight outlet glaciers of the Columbia Icefield (Figure 3.1a and 3.1b). The Columbia Icefield is situated at altitudes varying between 1900 m and 3500 m above sea level (asl). Altitudes of the AG are between approximately 2700 m and 2030 m. Between 1919 and 2009, long term mean annual air temperature (MAAT) at the Columbia Icefield is – 4.0°C and long term total annual precipitation is 1277 mm [Tennant and Menounos, 2013]. Average summer (June, July, and August) air temperature between 1988 and 2011 at Yoho National Park (51.35°N, 116.33°W), about 110 km SE of AG and at an altitude of 2045 m, is about 9°C [National Centers for Environmental Information, NOAA, retrieved on November 13, 2015]. The long term average air temperature at

Job Creek (52.35°N, 116.78°W), located about 40 km NE of the AG at an altitude of 2005 m, is about 5 C in May [Alberta Climate Information Service, retrieved on November 13, 2015]. These air temperatures allow ice melt to occur in summer. Long term annual precipitation at Job Creek is about 600 mm. Temperature and precipitation values recorded at these stations are considered to be representative of the AG because of their proximity and similar altitude.

The geology in the ice-free regions in the Columbia Icefield area has been extensively studied [Luckman and Crockett, 1978; Ross and Parrish, 1991; Gibson et al., 2005]. The bedrock underneath the Columbia Icefield is dominated by a formation known as zebra dolomites, which

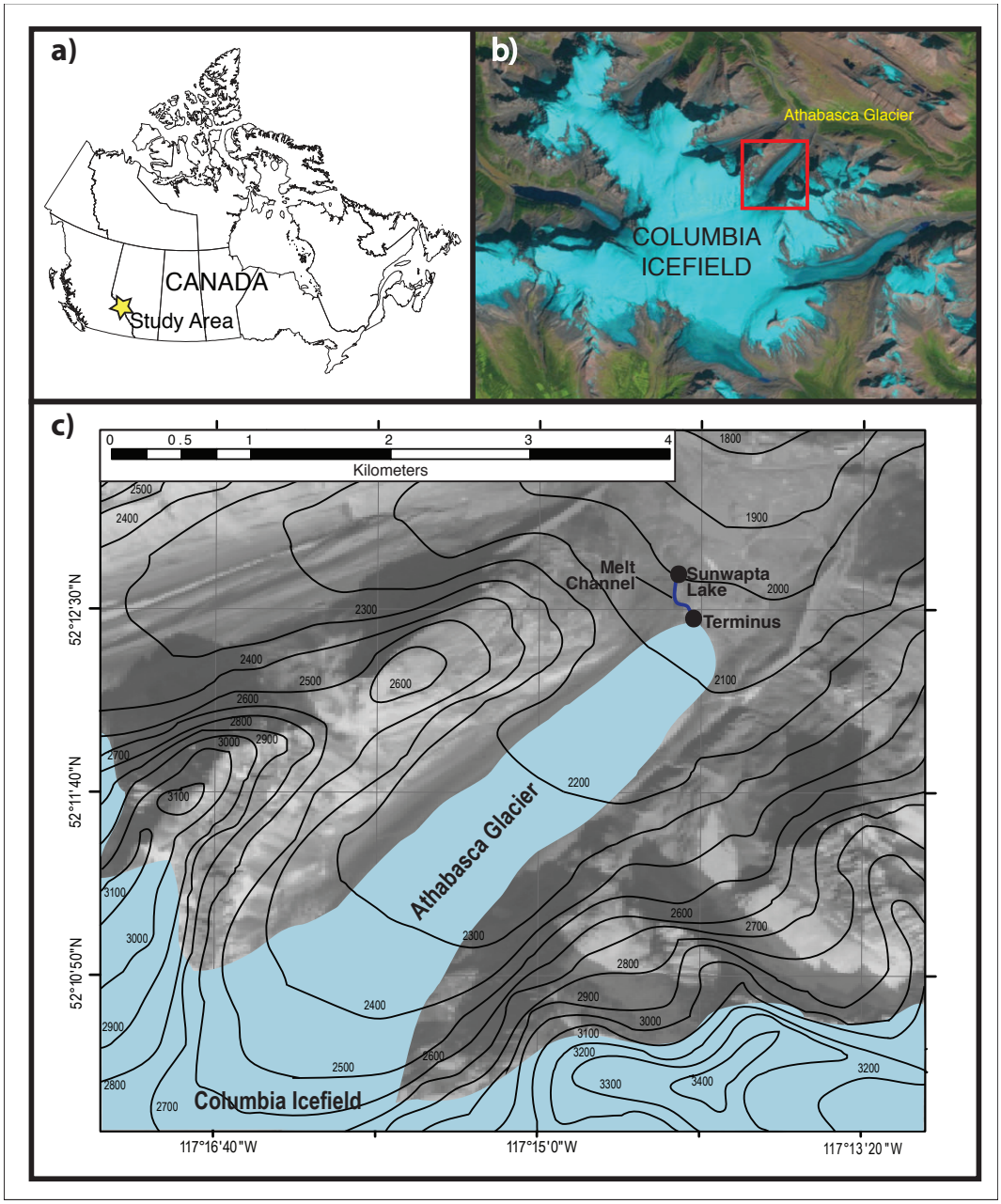

Figure 3.1 Map of Athabasca Glacier. Modified from Arendt et al. (2015).

contains repeated laminae of fine crystalline dark gray and coarse crystalline white dolomite [Swennen et al., 2003]. Hart [2006] described the bedrock at the AG's terminus as laminated limestone. The lithology around the Columbia Icefield is dominated by the Windermere Supergroup, which consists mainly of pelite and marble. Many other types of rock, including shale, sandstone, carbonates, syenite, granite, granodioritic gneiss, and other undivided sedimentary and metamorphic rocks are also present in the surrounding area [Luckman and Crockett, 1978; Parrish et al., 1988; Ross and Parrish, 1991; Crowley and Parrish, 1999; Johnston et al., 2000; Gibson et al., 2005].

3.3 Sampling and Analytical Methods

Water samples for noble gas analyses were collected in the morning on selected dates in May and July 2011 at 52°12.562”N, 117°14.287”W, 2030 m asl, 10 m downstream from the AG's terminus and at 52°12.360”N, 117°14.192”W, 2080 m asl, 200 m upstream from the initial terminus as the melt season progressed and the glacier retreated (Table 3.1). A total of eight samples were collected on six different days. On two collection days, two samples were collected at different times within the same day, samples 45 and 46 and samples 47 and 48.

Water samples were collected in standard refrigeration grade 3/8” copper tubing after being allowed to flow through for 10 min. As water flowed through the copper tube, the absence of gas bubbles was visually checked through a transparent plastic tube mounted to the end of the copper tube. The copper tubes were then sealed by stainless steel pinch-off clamps [Weiss, 1968]. All samples were analyzed for all stable noble gas concentrations (He, Ne, Ar, Kr, and Xe) and isotopic ratios in the Noble Gas Laboratory at the University of Michigan. The copper tube is attached to a vacuum extraction system and evacuated to below 2×10^{5} Torr. The bottom clamp is then opened, releasing the water into a low He diffusion glass flask. Extraction of the dissolved gases occurs in two stages: the first uses water vapor as a carrier gas to transport all dissolved gases through a tubing constriction into a liquid N_2 cold trap; the second stage uses water vapor from warming the small quantity of water in the cold trap to transport the dissolved gases into a section of the system with a 3Å molecular sieve. This part of the system is dried by the water adsorption properties of the molecular sieve, and the gases from the water sample can then be admitted into a clean-up section equipped with getter pumps to remove all active gases. Purified noble gases are then sequentially allowed to enter a MAP-215 mass-spectrometer using

Table 3.1 Sample number, sampling date, location, altitude, and measured water temperature.

Sample Number	Date Sampled	Longitude (West)	Latitude (North)	Elevation (m)	Water Temperature (°C)
03	05/07/11	52°12.562'	117°14.287'	2030	0.6
16	05/20/11	52°12.562'	117°14.287'	2030	1.3
38	07/16/11	52°12.360'	117°14.192'	2080	0.8
42	07/20/11	52°12.360'	117°14.192'	2080	n/a
45	07/23/11	52°12.360'	117°14.192'	2080	n/a
46	07/23/11	52°12.360'	117°14.192'	2080	n/a
47	07/25/11	52°12.360'	117°14.192'	2080	n/a
48	07/25/11	52°12.360'	117°14.192'	2080	n/a

a computer-controlled cryo-separator. The errors on measured He, Ne, Ar, Kr, and Xe concentrations are 1.5%, 1.3%, 1.3%, 1.5%, and 2.2%, respectively. Additional detail on sampling and measurement procedures can be found in Castro et al. [2009] and Hall et al. [2012].

3.4 Conceptual Model of the Glacial Hydrology

A conceptual model of the glacial hydrology near the terminus area is illustrated in Figure 3.2 [Martinerie et al., 1992, 1994; Skidmore et al., 2005; Das et al., 2008; Cuffey and Paterson, 2010; Arendt, 2015; Niu et al., 2015]. Snow and firn melt at the surface, where meltwater is in contact with air [Arendt, 2015]. Partial noble gas equilibration may occur both at the surface (area a) and at the terminus (area c) areas. An ASW component then forms on the surface as the surface GMW is exposed to the atmosphere for hours to weeks. For example, the formation of a supraglacial lake over 3 – 4 weeks was observed followed by massive and sudden drainage lasting ~1.4 h at an average rate of 8700 m^3/s in Greenland [Das et al., 2008]. As water is routed down to the bottom of glaciers by vertical conduits (crevasses and moulins), EA is likely incorporated in GMW. This EA component is similar to that present in sedimentary systems, which results from air bubbles trapped due to rapid water table fluctuations [Heaton and Vogel, 1981]. It is likely that the meltwater discharged at the base of the glacier is a combination

of surface melt transported to the base and basal melt which has interacted with subglacial till and bedrock [Jean-Baptiste et al., 2001; Skidmore et al., 2005; Arendt, 2015]. As ice melts at the base, trapped air in ice can also be incorporated into the subglacial meltwater under the pressure of the glacier, whose composition is nearly indistinguishable from that of EA in sedimentary systems. This was observed in earlier studies of noble gases in ice cores and seawater affected by the submarine melting of ancient glacial ice [e.g. Schlosser, 1986; Schlosser et al., 1990; Martinerie et al., 1992, 1994; Weppernig et al., 1996; Hohmann et al., 2002; Loose and Jenkins, 2014]. However, the contribution of trapped glacial air is expected to be minor given the local hydrologic conceptual model for the glacier near the terminus area (Figure 3.2).

The diffusion rates of noble gases into water are relatively low in comparison to the time scale required for water to flow from the terminus to the collection point (~10 m away from the terminus). The diffusion coefficients of noble gases in water at a temperature of 5°C are: D_{He} = 5.10×10^{-5} cm^2/s, $D_{Ne} = 2.61 \times 10^{-5}$ cm^2/s, $D_{Kr} = 1.02 \times 10^{-5}$ cm^2/s, and $D_{Xe} = 0.774 \times 10^{-5}$ cm^2/s [Jähne et al., 1987]. When there is no turbulence, within 100 s (~2 min), noble gases can diffuse for distances of 0.7 mm, 0.5 mm, 0.3 mm, 0.3 mm for He, Ne, Kr, and Xe, respectively, using the equation $x^2 = Dt$, where x is mean displacement, D is the diffusion coefficient, and t is time. These distances are overestimated for the collection conditions, as diffusion coefficients are lower at temperatures around 1°C than at 5°C. Noble gases are expected to diffuse for distances significantly under 1 mm during the time water flows from the terminus (~ 30 s), so the sampling

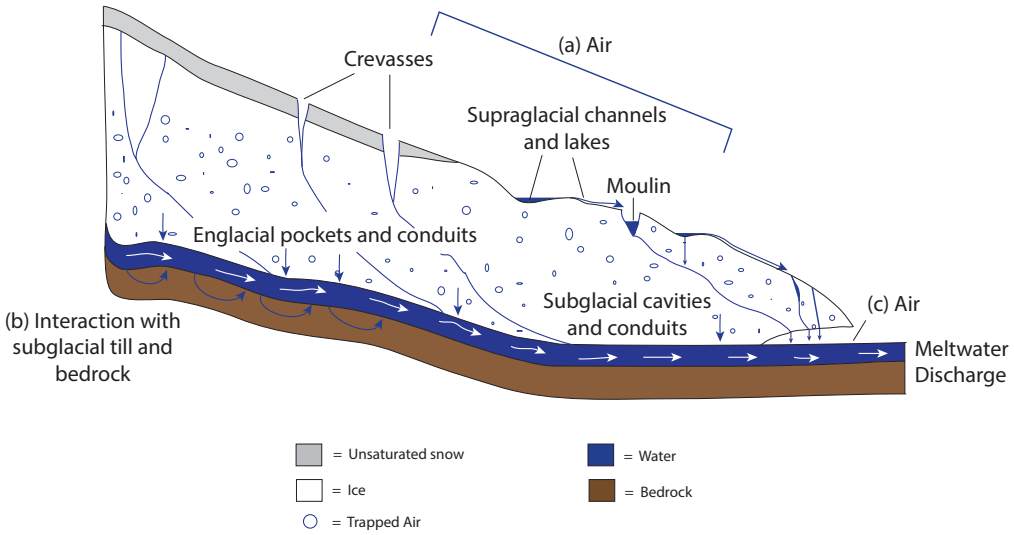

Figure 3.2 Conceptual model of the glacial hydrology near the terminus area (Niu et al., 2015).

methodology is not expected to lead to erroneous data due to noble gas equilibration with the atmosphere at the point of sample collection.

The same conceptual model of the glacial hydrology near the terminus area was applied to the GrIS and is well supported by the noble gas signatures revealed in the GrIS GMW [Niu et al., 2015]. In that study, subglacial meltwater, surface meltwater, and river water samples were collected [Niu et al., 2015]. In this study, meltwater samples were collected within 10 m of the terminus of an outlet glacier of an alpine icefield (the Columbia Icefield), but not at the surface or from rivers. As shown below (cf., section 3.5), the AGMW exhibits a similar pattern to that of the GrIS where the ASW component dominates with the addition of some EA.

3.5 Results

Figure 3.3a exhibits measured noble gas concentrations of our AGMW samples normalized to those in the expected trapped air in glacial ice, i.e., 0.09 cm^3 of air per gram of ice [Martinerie et al., 1992; 1994]. It is apparent that our samples are heavily depleted in Ne and extremely enriched in Xe when compared to trapped in
glacial ice. These measured concentrations contrast strikingly with those of trapped air in glacial ice and suggest that the bulk of AGMW is not derived directly from the melting of old glacial ice in the absence of atmospheric contact. If this were the case, a nearly horizontal pattern would be expected. Figure 3.3b displays measured noble gas concentrations normalized to the ASW concentrations corresponding to measured water temperature and altitude at the collection points. He and Ne in trapped air in ice normalized to ASW at 2080 m and 0°C are not shown as they are 12.3 and 9.3 times greater than the ASW values at collection conditions, respectively, and are off scale in the current diagram. With the exception of He, for which buildup of radiogenic ^{4}He is observed, and in contrast to trapped air in ice, it is apparent that most samples display a pattern far closer to that of ASW compared to that of trapped air in glacial ice. This suggests that an ASW component largely dominates over any possible EA component, including one originating from trapped air in glacial ice for the four heavier noble gases.

For all of the eight AGMW samples, noble gas concentrations do deviate to a certain degree from expected ASW values ($C/C_{ASW} = 1$) corresponding to measured water temperature and altitude at the collection points (Table 3.2; Figure 3.3). For most samples, 1s error bars are smaller than the symbols. For samples without a record of water temperature, 0°C was used to

normalize measured values. As the subglacial meltwater is constantly in contact with the glacier, it is likely that the water temperature does not deviate much from 0°C. All samples display He excesses with respect to ASW values ranging from 4% to 91%. The origin and source of these He excesses are constrained below by R/R_a values, where R is the measured $^3He/^4He$ ratio and R_a is the atmospheric value of 1.384×10^6 [Clarke et al., 1976].

In contrast to He, Xe concentrations for all samples are depleted with respect to ASW, with depletion levels varying from 2% to 14%. Five samples are depleted in Kr with depletion values ranging from 2% to 10%. Three samples display Kr enrichments up to 4%. In contrast, six out of eight Ne samples are enriched, with enrichment values varying between 6% and 43%. Six samples are enriched in Ar, with enrichment levels varying from 2% to 18%, while two samples are depleted up to 2%. This suggests an apparent lack of equilibration of the AGMW with the atmosphere, as measured noble gas concentrations deviate from ASW values at collection conditions. Similar to the GrIS meltwater samples [Niu et al., 2015], two noble gas patterns are

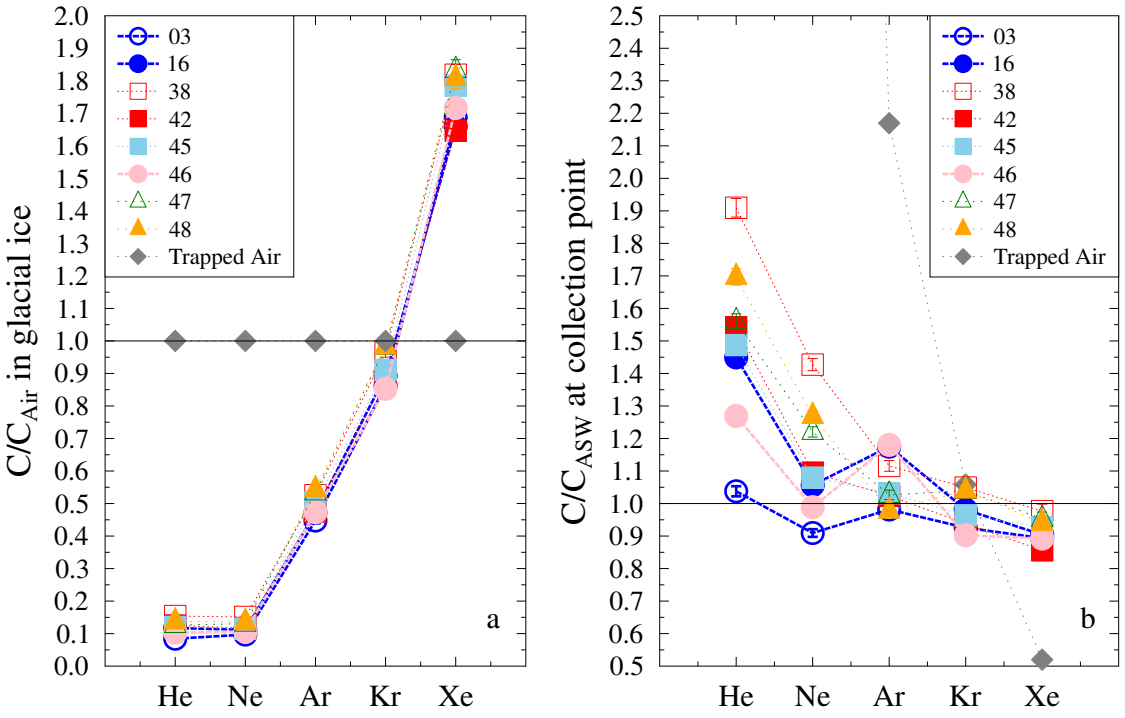

Figure 3.3 Measured noble gas concentrations normalized to (a) trapped air in compressed glacial ice, and (b) ASW at collection water temperatures and altitudes. The solid black line indicates noble gas concentrations with no addition or loss of gases compared to (a) trapped air, and (b) ASW. For most samples, 1σ error bars are smaller than the symbols.

Table 3.2 Measured noble gas concentrations at STP[1], R/R_a [2], R_{exc}/R_a values, estimated equilibration altitudes based on each gas, estimated EA amounts to account for Ne excesses with respect to ASW at 0°C and collection altitudes for each sample, and ASW noble gas concentrations at a temperature of 0°C and altitudes of 2030 m and 2080 m. For samples 03 and 46, estimated Ne altitudes are compatible with local topography, and are assumed to have no EA.

Sample Number	He 10^{-8} cm^3 g^{-1}	Ne 10^{-7} cm^3 g^{-1}	Ar 10^{-4} cm^3 g^{-1}	Kr 10^{-8} cm^3 g^{-1}	Xe 10^{-8} cm^3 g^{-1}	R/R_a ($\pm1\sigma$)	R/R_a without ^{3}He from 5 TU of ^{3}H ($\pm1\sigma$)	R_{exc}/R_a ($\pm1\sigma$)	Estimated Equilibration Altitude				EA based on Ne excess (10^{-4} cm^3/g)
									Ne (m)	Ar (m)	Kr (m)	Xe (m)	
03	3.97	1.59	3.77	8.85	1.32	0.98 (0.03)	0.75 (0.02)	0.96 (0.91)	2900	2300	2800	3200	-
16	5.53	1.83	4.00	9.16	1.30	0.92 (0.02)	0.76 (0.01)	0.74 (0.11)	1700	990	2500	3300	3.86
38	7.26	2.47	4.47	9.90	1.42	1.03 (0.04)	0.91 (0.04)	1.23 (0.29)	-790	1400	1900	2500	39.8
42	5.89	1.92	4.02	9.10	1.29	0.90 (0.02)	0.75 (0.01)	0.67 (0.10)	1300	1900	2600	3400	9.16
45	5.68	1.89	4.22	9.34	1.40	0.80 (0.14)	0.64 (0.11)	0.27 (0.54)	1400	1800	2400	2700	7.69
46	4.85	1.73	3.99	8.75	1.34	1.16 (0.02)	0.98 (0.02)	1.83 (0.18)	2200	710	2900	3000	-
47	5.96	2.14	4.51	10.08	1.44	1.01 (0.04)	0.86 (0.03)	1.13 (0.27)	430	1900	1800	2500	21.2
48	6.49	2.22	4.62	10.09	1.42	0.78 (0.03)	0.64 (0.02)	-	100	2800	1800	2600	25.9
ASW 0°C 2030 m	3.85	1.76	3.9	9.76	1.52								
ASW 0°C 2080 m	3.82	1.75	3.87	9.7	1.51								

[1]Measurement errors of noble gas concentrations are 1.5%, 1.3%, 1.3%, 1.5%, and 2.2% for He, Ne, Ar, Kr, and Xe, respectively.
[2]Helium isotope ratios, $R = {}^3He/{}^4He$, are normalized by the atmospheric value of $R_a = 1.384 \times 10^{-6}$ [Clarke et al., 1976].

observed in the AGMW samples. One group dis- plays a mass-dependent depletion pattern, where the heavier noble gases are more depleted compared to the lighter ones. This group consists of samples 38, 42, and 45 (squares in Figures 3.3 and 3.5). All of these three samples present Ne excesses with respect to ASW values. The second group displays a relative Ar enrichment with respect to Ne, Kr, and Xe. This group consists of samples 03, 16, and 46 (circles with bold lines in Figures 3.3 and 3.5). These three samples all present Kr and Xe depletion compared to ASW values. In these three samples, while Ar is relatively enriched with respect to Ne, there is not a consistent pattern in Ne and Ar concentrations with respect to ASW.

Specifically, sample 03 is depleted in both Ne and Ar, sample 16 is enriched in both Ne and Ar, and sample 46 is depleted in Ne and enriched in Ar. Samples 47 and 48, collected the same day, do not fit in these two groups, presenting similar Ar and Kr concentrations normalized to ASW or Kr enrichment relative to Ar. The relative-Ar-enrichment or Ne-depletion pattern was first observed in high-altitude springs in the Galápagos Islands [Warrier et al., 2012] and

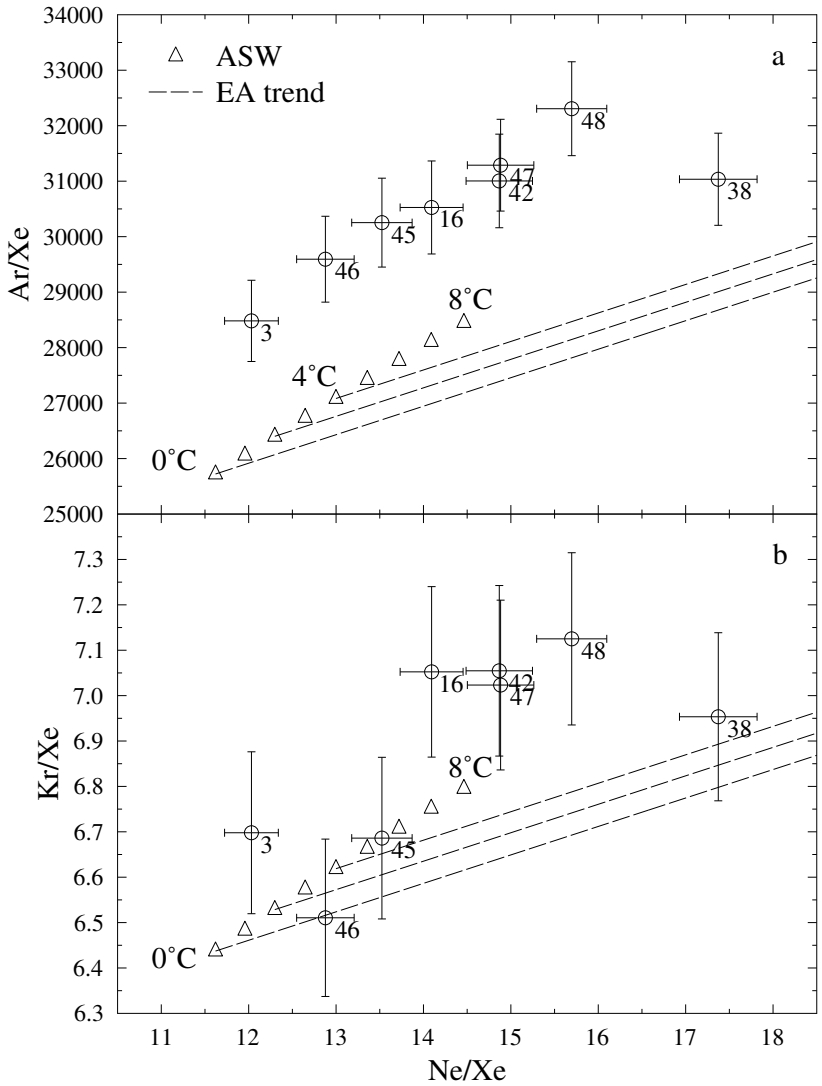

Figure 3.4 Preliminary estimation of equilibration temperatures. Measured (a) Ar/Xe and (b) Kr/Xe ratios versus Ne/Xe. ASW values for temperatures between 0°C and 8°C are also shown, at intervals of 1°C. Dashed lines originating from triangles show how addition of EA affects these ratios from initial ASW compositions at 0°C, 2°C, and 4°C. None of the samples yield conditions compatible with the local environment for all four noble gases simultaneously.

subsequently in rainwater in southeast Michigan [Warrier et al., 2013]. More recently, it was also observed in GMW from the GrIS [Niu et al., 2015]. For most samples, Ne, Ar, Kr, and Xe isotopic ratios are indistinguishable from atmospheric values, as was also observed in the GrIS samples.

3.6 Discussion

3.6.1 Equilibration Temperatures and Altitudes

Concentrations of atmospheric noble gases dissolved in water record various physical parameters (e.g., temperature, altitude, and EA) at which final equilibration with the atmosphere takes place. When the ambient air pressure is not 1 atm, a uniform correction factor is applied to the solubility values at sea level in distilled water for all noble gases [Mazor, 1972]. As the same correction factor for altitude is applied to all noble gases, the Ne/Xe, Ar/Xe, and Kr/Xe ratios in ASW are independent of altitude and are functions of temperature only. The measured Ar/Xe and Kr/Xe versus Ne/Xe are compared with ASW values at temperatures between 0°C and 8°C in Figure 3.4. Dashed lines originating from triangles show how addition of EA affects these ratios from initial ASW compositions at 0°C, 2°C, and 4°C. From Figure 3.4, it is apparent that our samples are not in equilibrium with the atmosphere at conditions comparable with the local climate and geography and different gases exhibit very different patterns. It should be noted that the temperature of basal melt water is always near the freezing point, for it is in constant contact with the glacier, and the highest measured water temperature for our samples is 1.3°C, with other measured glacial melt water temperatures below 1°C (Table 3.1). All samples plot above and/or to the left of the lines representing ASW with EA in Figure 3.4a, which is the result of relative Ar excess and/or Ne depletion. This suggests that none of the samples is in equilibrium. In contrast, a subset of samples in Figure 3.4b exhibits Kr/Xe ratios apparently compatible with ASW and EA within one sigma error, when none of the samples in this group is equilibrated in Ar. As different gases have very different degrees of equilibration, it is not possible to estimate meaningful equilibration conditions based solely on measured ratios of gas concentrations. Therefore, it is necessary to examine each gas separately.

To determine equilibration altitudes based on one single noble gas, an equilibration temperature of 0°C was assumed for all samples. Estimation of recharge altitude was done assuming ASW concentrations and with an altitude correction factor as outlined in Ballentine

and Hall [1999]. Because of its low diffusion coefficients in air and water, Xe requires the longest equilibration times, so it provides the most reliable estimate of original equilibration altitudes. Figure 3.5 exhibits the equilibration altitudes estimated based on Ne, Ar, Kr, and Xe for each sample and 1s error bars are shown; these equilibration altitudes are also tabulated in Table 3.2. Compatible equilibration altitudes are bounded by the local maximum altitude (3500 m) and collection altitudes (2080 m and 2030 m, respectively), all shown as black solid lines (Figure 3.5). A dashed line shows the maximum altitude of the AG at 2700 m. If the

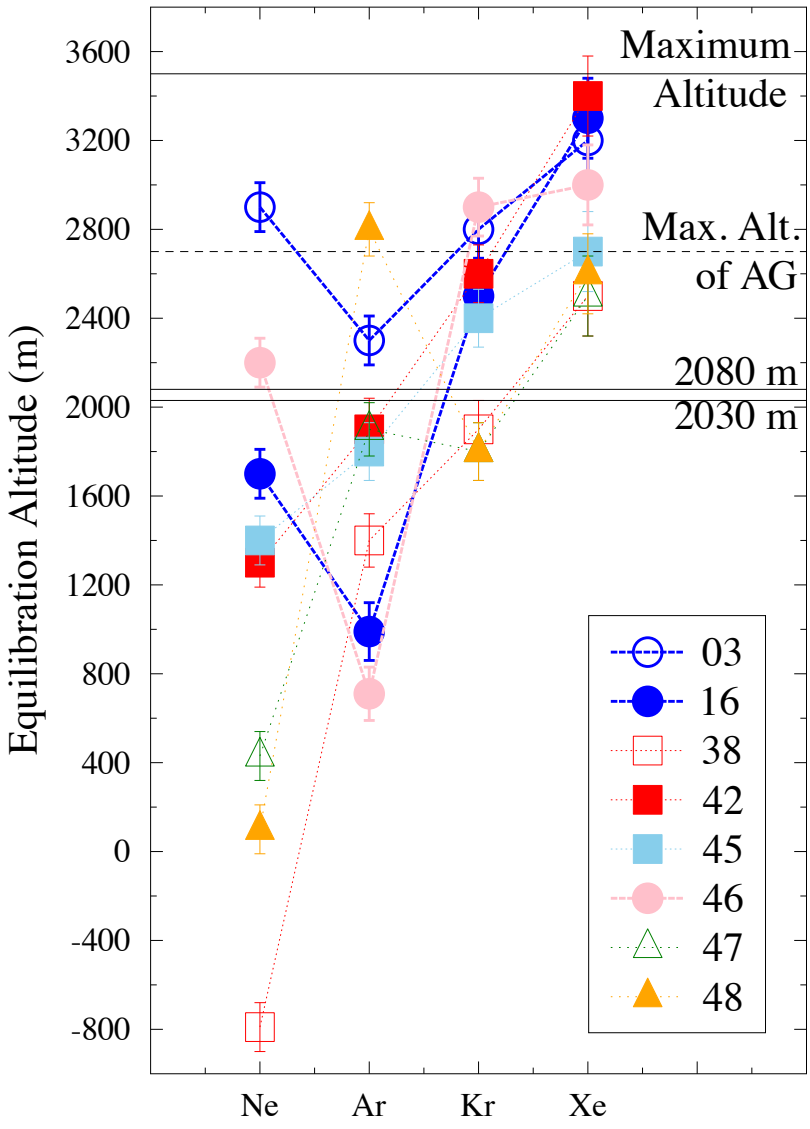

Figure 3.5 Equilibration altitudes based on single gas concentrations assuming an equilibration temperature of 0°C. The black solid lines indicate the elevation interval physically possible based on the topography at the Columbia Icefield. A dashed black line indicates maximum altitude of AG.

equilibration altitude based on any gas is higher than the local maximum altitude, the sample is depleted in this gas with respect to the ASW values at 0°C, which suggests that the sample was still in disequilibrium with the atmosphere at the time of collection. If the equilibration altitude based on any gas is lower than the collection altitude, the sample is enriched in this gas with respect to the ASW values at 0°C and collection altitude. When estimated Ne altitudes are lower than collection altitudes, it suggests the presence of EA. For these samples, one can estimate the EA amounts required to account for the Ne excesses with respect to ASW at 0°C and collection altitudes (Table 3.2). Specifically, for each sample, the difference between total measured Ne concentration and the ASW value at 0°C and collection altitude is assumed to be from EA only. The EA amount is then estimated following Ballentine and Hall [1999].

All AGMW samples show Xe equilibration altitudes ranging from 2500 m to 3400 m, compatible with local topography, and higher than their collection altitudes, suggesting that they were in the process of achieving equilibrium with the atmosphere at the time of collection. All samples, except sample 46, display Kr altitudes lower than Xe altitudes, suggesting that Kr has achieved a higher degree of partial equilibration in those samples. Sample 46 displays similar Kr and Xe altitudes, suggesting that Kr has just started to equilibrate and yields the altitude of the water source. Five of eight samples present Xe equilibration altitude equal to or higher than the highest elevation of the Athabasca Glacier (2700 m; Figure 3.5 and Table 3.2). This suggests that at least some of the subglacial meltwater currently discharged at the terminus of the AG does not originate from the AG itself but instead, from more distant locations within the Columbia Icefield.

With the exception of samples 03 and 46, all other AGMW samples display Ne altitudes lower than the collection altitudes suggesting the presence of EA. Samples 03 and 46 display apparently compatible Ne altitudes; however, Ne might have undergone depletion due to other processes, so the presence of EA cannot be ruled out. Warrier et al. [2012] hypothesized that the mixing of low-altitude fog and high-altitude precipitation is partially responsible for the Ne anomalies observed in their high altitude spring samples. Following a pilot rainwater noble gas study in southeast Michigan, Warrier et al. [2013] subsequently suggested that these Ne anomalies are associated with different weather patterns. Additional noble gas studies of fog, synoptic and orographic rain as well as snow are currently underway in an attempt to achieve a greater level of understanding of noble gas behavior in these environments and hopefully, a

better understanding of the source of the observed Ne and possibly Ar anomalies.

Samples 47 and 48, collected on the same day, register similar apparent Kr and Xe altitudes, but different Ne altitudes and even more drastically different Ar altitudes. Specifically, Ne altitude is 430 ± 110 m for sample 47 and 100 ± 110 m for sample 48; Ar altitude is 1900 ± 120 m for sample 47 and 2800 ± 120 m for sample 48. The difference in Ne altitudes for the two samples is barely over the sum of their 1σ errors, while estimated Ar altitudes for the two samples are clearly distinct. This suggests that local glacial hydrology and dynamics changed rapidly during the course of an hour during which both samples were collected, leading to very different processes that impact Ne and Ar concentrations within the AGMW. This is not unexpected taking into account the fast, turbulent flow observed at the collection site during sample collection. This turbulent flow might also be the cause of the observed high level of EA in some of these samples. Samples 45 and 46 yield different equilibration altitudes for all gases without a specific pattern. Specifically, sample 46 displays a much lower Ar altitude than Ne altitude while sample 45 yields lower equilibration altitudes for lighter noble gases. These two samples also suggest very rapid changes in local glacial hydrology and dynamics within the time-frame of an hour.

In conclusion, different gases have achieved different degrees of equilibrium or have equilibrated with the atmosphere at different altitudes. On the other hand, if the equilibration temperature is assumed to be 0°C, Xe concentrations alone indicate that all samples equilibrated with the atmosphere at altitudes varying between 2500 m and 3400 m. Most samples display Xe equilibration altitudes above the maximum altitude of the AG (~2700 m), suggesting that a significant portion of the current AG meltwater originates in the Columbia Icefield which contributes to both the AG per se and current subglacial meltwater discharge. Overall, it is apparent that all samples are in disequilibrium with the atmosphere at collection conditions.

3.6.2 Glacial Meltwater Sources and Residence Times

The separation and quantification of different He components, i.e., atmospheric, crustal and/or mantle, under certain assumptions, allows for the identification of different water sources within the AGMW, i.e., precipitation as rain, snow or ice versus groundwater. Estimation of the crustal He component subsequently allows for estimation of groundwater residence times under certain simplifications and assumptions. This analysis is typically done by plotting R_{noea}/R_a

versus $^4He_{eq}/^4He_{noea}$ [e.g., Weise, 1986; Weise and Moser, 1987; Castro, 2004; Wen et al., 2016a]. We specify

$$He_{noea} = He_s - He_{ea}, \quad (3.1)$$

$$He_{exc} = He_s - He_{eq} - He_{ea}, \quad (3.2)$$

where He_s is measured total He concentration of the sample, He_{eq} and He_{ea} are the ASW and EA components, respectively. He_{noea} is the measured He concentration without the EA He component and He_{exc} is the measured He concentration without both the ASW and EA He components. He_{ea} is estimated following Eq. (3.3) [Kipfer et al., 2002]:

$$He_{ea} = (He/Ne)_{atm} * (Ne_s - Ne_{eq}), \quad (3.3)$$

where Ne_S is measured total Ne concentration and Ne_{eq} is the ASW component at collection altitude and water temperature. $(He/Ne)_{atm}$ is the ratio of He and Ne in the atmosphere and is equal to 0.2882 ± 0.0028 (Ozima and Podosek, 2002). Concentrations of ^3He are given given by $^3He_s = {}^4He_s * R$, $^3He_{eq} = {}^4He_{eq} * R_{eq}$, and $^3He_{ea} = {}^4He_{ea} * R_a$, where $R_{eq} = (1.360 \pm 0.006) * 10^{-6}$ [Benson and Krause, 1980] and R are the $^3He/^4He$ ratios for ASW and total measured He, respectively. In addition, we specify:

$$R_{noea} = \frac{^3He_{noea}}{^4He_{noea}} \quad (3.4)$$

and

$$R_{exc} = \frac{^3He_{exc}}{^4He_{exc}}, \quad (3.5)$$

where R_{noea} and R_{exc} are the $^3He/^4He$ ratio without the EA component and that without both the ASW and EA components, respectively. Sample 03 and 46, with no Ne excess with respect to the ASW value, are subsequently treated as samples without EA. Calculated R_{exc}/R_a values are indicated in Table 3.2. Sample 03 has very little total He excess and sample 45 has very little excess ^3He ($^3He_{exc}$), which results in large errors in R_{exc}/R_a estimates. Sample 48 has no $^3He_{exc}$, leading to a negative apparent R_{exc}/R_a.

Figure 3.6 shows a plot of R_{noea}/R_a versus $^4He_{eq}/^4He_{noea}$ for AGMW (this study) and GrIS GMW [Niu et al., 2015] samples. Error bars show 1σ errors. Colored solid lines indicate the expected position for samples with tritiogenic ^3He levels varying from 0 to 12 TU and 0% mantle contribution while dashed lines indicate mantle contributions of 1% and 2% and a tritiogenic ^3He level of 0 TU. The lines are calculated following:

$$R_{noea}/R_a = \frac{{}^4He_{eq}R_{eq} + {}^4He_{exc}R_{exc} + {}^3He_{trit}}{{}^4He_{noea}R_a} \quad (3.6)$$

and rearranged to

$$R_{noea}/R_a = (kx + R_{exc}) / R_a \quad (3.7)$$

where, $k = R_{eq} - R_{exc} + {}^3He_{trit} / {}^4He_{eq}$, (3.8)

$$x = {}^4He_{eq} / {}^4He_{noea}, \quad (3.9)$$

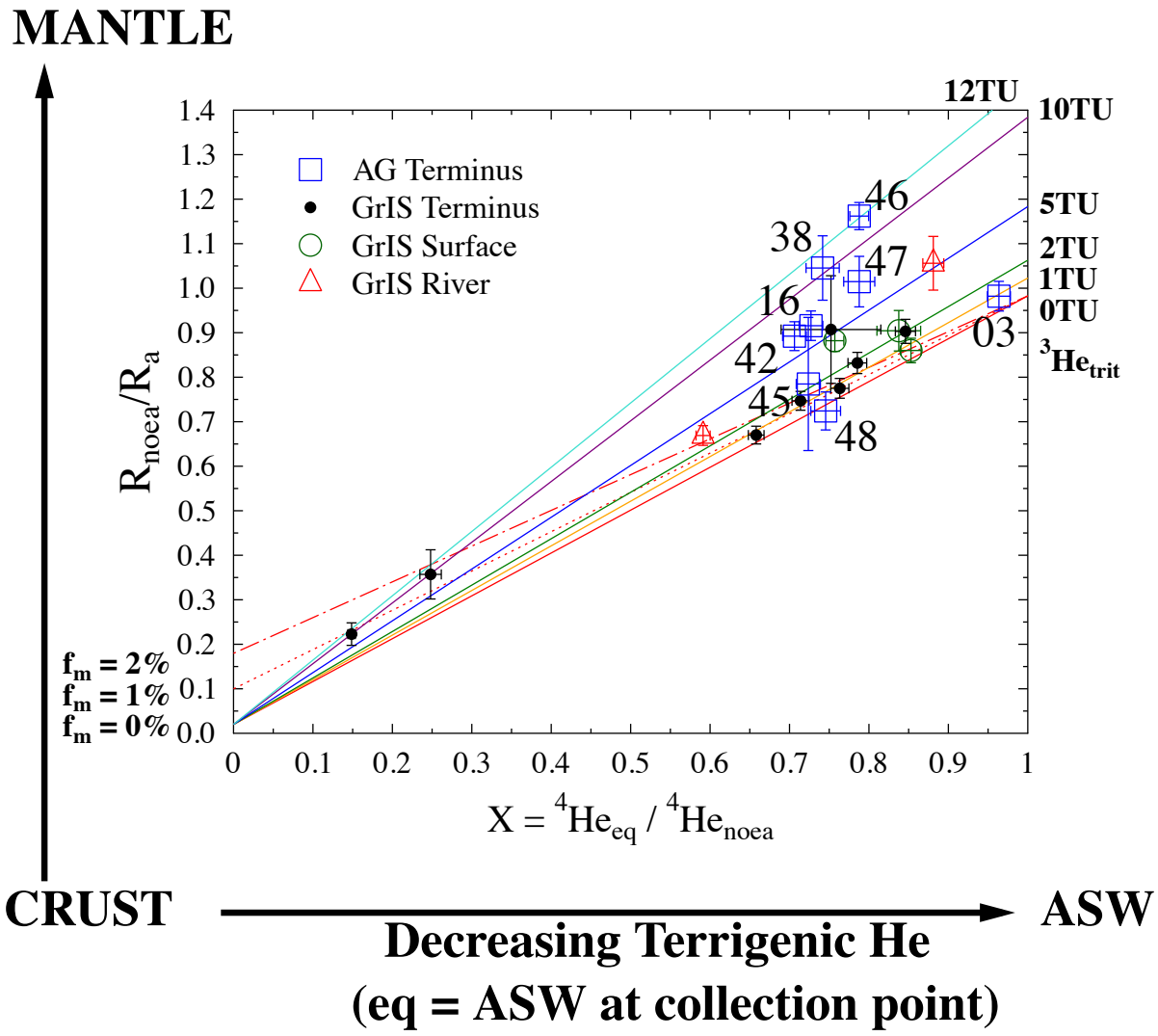

Figure 3.6 Helium component separation for the AGMW samples compared with GrIS samples (Niu et al., 2015). R/Ra values for crustal and mantle components are assumed to be 0.02 and 8, respectively. Lines corresponding to 0%, 1%, and 2% mantle helium and 0, 1, 2, 5, 10, and 13 TU tritiogenic ^{3}He are shown.

and

$$R_{exc} = f_m R_m + (1- f_m) R_c. \quad (3.10)$$

The term f_m, indicated along the left vertical axis, corresponds to the fraction of the mantle contribution and (1- f_m) is the crustal fraction of the terrigenic end-member. R_c and R_m are the $^3He/^4He$ crustal and mantle for the mid-ocean ridge basalts (MORB) ratio end-members, respectively, and are assumed to be 0.02 [O'Nions and Oxburgh, 1983] and 8 [Farley and Neroda, 1998] times the atmospheric ratio (R_a), respectively. The x coordinate indicates the He fraction contributed by ASW. The ASW component increases with decreasing terrigenic He. The fraction of terrigenic end-member is (1-x). In this graphic, a sample displaying a value of 1 on the horizontal axis points to a component of purely atmospheric origin or ASW, while a value approaching 0 points to a solely terrigenic origin. Increasing values on the left vertical axis denote increasing mantle contributions, while increasing values on the right vertical axis reflect increasing tritiogenic ^3He levels (in TU; 1 TU is equivalent to $2.5 * 10^{-15}$ cm^3 of ^3He per gram of water [Schlosser et al., 1988]). Samples plotting along a particular mixing line represent varying contributions of these components.

Figure 3.6 points to tritiogenic ^3He levels for AGMW samples varying between 0 and 12 TU, a wider range in tritiogenic values than that previously observed in GrIS GMW samples (0 – 5 TU) [Niu et al., 2015]. Samples 03, 45, and 48 point to tritiogenic ^3He levels of 1 TU, 2 TU, and approximately 0 TU, respectively. These values are below the pre-bomb tritium levels in precipitation (5 TU) [Craig and Lal, 1961; Roether, 1967]. Samples 16, 38, 42, 46, and 47 exhibit tritiogenic ^3He levels between 5 TU and 12 TU. Unlike the GrIS GMW samples, all the AGMW samples plot near the right hand side of the figure indicating the presence of a largely dominant ASW component. ASW contributions vary between 71% (42) and 96% (03) with a significantly smaller crustal contribution of ~4% (03) – 29% (42). This suggests that at least 71% – 96% of the water is from precipitation as liquid, snow, or ice, with the remainder being meltwater either from the base of the glacier that has accumulated ^4He over time or directly from groundwater moving upward, a process commonly observed in crystalline, fractured systems. Processes such as upward He diffusion are not considered, rendering these fractions representative of lower limits, and they may be underestimated.

For most samples, tritiogenic ^3He levels found in the AGMW are similar to ^3H levels found in modern precipitation at high latitudes in North America, for example, 4 TU in Portland, Oregon

in 2002, 18 TU in Ottawa, Ontario in 2007, and 7 TU in Anchorage, Alaska in 2009 [International Atomic Energy Agency, retrieved on October 27, 2015]. AG runoff water ^{3}H levels measured in 1963 yielded 420 TU and that in precipitation at Jasper National Park, of which the AG is part, yielded 8200 TU [Leventhal and Libby, 1970]. At the time our samples were analyzed (2012 and 2013), about four half-lives of ^{3}H ($t_{1/2}$ = 12.43 yr) [Unterweger et al., 1980] had elapsed since the bomb-test peak in 1963, more than 93% of the ^{3}H in the runoff and precipitation measured in 1963 should have decayed into ^{3}He and register tritiogenic ^{3}He levels of about 390 TU and 7600 TU, which are far greater than those estimated in our samples. Three scenarios could potentially lead to the tritiogenic ^{3}He estimated in the AGMW samples (0 – 12TU): (1) AGMW samples are older than the bomb-test era so that they contained solely background tritium levels (5 TU) at the time of ice formation; (2) AGMW samples are all extremely recent and are representative of present precipitation so the ^{3}H has not yet decayed to the ^{3}He levels seen in our samples; (3) AGMW samples represent a mixture of the pre-bomb, bomb, or post- bomb-era water and present day water, the latter having diluted the tritiogenic ^{3}He brought by the former component. Measurements of ^{3}H levels in AGMW samples would allow identification of these three possible scenarios; tritium measurements, however, are not available for these samples. For samples 03, 45, and 48, of which tritiogenic ^{3}He levels are below 5 TU, only scenario (2) or (3) applies; otherwise, at least 5 TU of tritiogenic ^{3}He should be detected. Given that surface meltwater is routed down through vertical crevasses and water is needed to keep the crevasse open and propagating [Das et al., 2008], it is likely that ice from different depths, which formed at different time periods, is being partially melted and incorporated in the meltwater collected in the terminus area. Thus, scenario 3 is the most likely explanation for the AGMW samples' tritiogenic compositions. The observed contrast between samples 45 and 46 and that also observed between samples 47 and 48, again, suggests very rapid changing local hydrology and conditions.

In general, the tritiogenic ^{3}He levels in the AGMW samples overlap with those of the GrIS samples with AG samples displaying a wider tritiogenic ^{3}He range than GrIS samples [Niu et al., 2015]. Unlike two GrIS samples, however, none of the AGMW samples is dominated by crustal He, suggesting relatively short water residence times. ^{4}He concentrations suggest that at least 71% – 96% of the water is from surface snow or ice melt, with the remainder being meltwater from the base of the Columbia Icefield or the AG and/or groundwater that has

accumulated ^{4}He over time. Processes such as upward He diffusion are not considered, so the fractions of basal melt represent upper limits and may be overestimated. Irrespectively, surface melt is likely the primary source for the water discharge from the AG with basal ice melt being a secondary source [Arendt, 2015].

As discussed above, all of the AGMW samples have fractions of crustal He varying between 4% and 29%. The presence of a crustal component is also apparent when the decay product of tritium background in precipitation of 5 TU [Craig and Lal, 1961; Roether, 1967] is excluded from total ^{3}He concentrations assuming complete decay, leading to R/R_a values below 1 for all samples (Table 3.2). It is therefore possible to derive first-order estimates of AGMW ages based on $^4He_{exc}$ concentrations, together with estimated ^{4}He production rates in basement rocks and ^{4}He accumulation rates in water. Production rates of ^{4}He in basement rocks are calculated as follows [Ballentine et al., 1991]:

$$P\,(^4He)_{rock} = 1.207\times10^{-13}\,[U] + 2.867\times10^{-14}\,[Th]\ \ cm^3\ STP\ g_{rock}^{-1}\ yr^{-1} \qquad (3.11)$$

where [U] and [Th] represent the U and Th concentrations. U and Th concentrations in the zebra dolomite, the dominant lithology under the Columbia Icefield and the AG, are not available and the lithology in the surrounding areas is complex, making it difficult to estimate a specific average composition for this area. Therefore, U and Th concentrations of average carbonate rocks ([U] = 2.2 ppm, [Th] = 1.7 ppm) [Parker, 1967] and those of average upper continental crust ([U] = 2.7 ppm, [Th] = 10.5 ppm [Rudnick and Gao, 2005] are used for a first order AGMW age estimation. ^{4}He accumulation rates in water, $P\,(^4He)_{H2O}$, were subsequently estimated according to:

$$P\,(^4He)_{H2O} = P\,(^4He)_{rock} * \rho_r * \Lambda * (1-\omega)/\omega\ \ cm^3\ STP\ cm^{-3}{}_{H2O}\ yr^{-1} \qquad (3.12)$$

where ρ_r is the mass density of the rock, assumed to be 2.7 g/ cm^3; ω is the porosity of the basement rock; Λ, which is the transfer efficiency of ^{4}He from the rock and glacial substrate to the water, is assumed to be 1 [Torgersen et al., 1989].

Effective porosities in carbonate rocks vary between 0.1 and 5% [Croff et al., 2003]. Assuming a porosity of 1%, the typical value of effective porosity for carbonate rocks [Croff et al., 2003] and average U and Th concentrations of carbonate rocks [Parker, 1967], the average water residence time is 140 ± 5 years (standard deviation of the mean) for all samples (Table 3.3), or 160 ± 5 years without sample 03, which is significantly younger than all other samples.

Table 3.3 Water residence times (^{4}He ages) calculated based on $^4He_{exc}$ assuming porosities of 0.1%, 1%, and 5% and U and Th concentrations of carbonate rocks and those assuming porosities of 2.5% and 5% and U and Th concentrations of the upper continental crust. ^{4}He age estimates are in years with 1σ errors in parentheses. U-series ages are in years with 2σ errors in parentheses.

Sample Number	Collection Date	$^4He_{exc}$ (10^{-8} cm^3 g^{-1})	+/-	^{4}He age Carbonates ω = 0.1%	^{4}He age Carbonates ω = 1%	^{4}He age Carbonates ω = 5%	^{4}He age Continental Crust ω = 2.5%	^{4}He age Continental Crust ω = 5%	U-series age
03	05/07/11	0.14	0.06	2 (1)	17 (7)	90 (40)	20 (10)	40 (20)	25.7 (5.4)
16	05/20/11	1.43	0.11	17 (1)	170 (10)	890 (70)	220 (20)	450 (30)	-
38	07/16/11	1.32	0.14	16 (2)	170 (10)	820 (90)	200 (20)	410 (40)	1.7 (1.1)
42	07/20/11	1.59	0.11	19 (1)	190 (10)	970 (70)	240 (20)	490 (40)	1.1 (0.6)
45	07/23/11	1.46	0.11	17 (1)	170 (10)	910 (70)	220 (20)	450 (30)	4.9 (2.3)
46	07/23/11	1.03	0.07	12 (1)	120 (10)	640 (50)	160 (10)	320 (20)	4.9 (2.3)
47	07/25/11	1.03	0.12	12 (1)	120 (10)	640 (70)	160 (20)	320 (40)	3.3 (4.1)
48	07/25/11	1.31	0.13	15 (2)	160 (20)	810 (80)	200 (20)	410 (40)	3.3 (4.1)
Average	-	-	-	14 (1)	140 (5)	720 (20)	180 (10)	360 (10)	
Average without 03	-	-	-	15 (1)	160 (5)	810 (30)	200 (10)	410 (10)	

Water residence times are nearly proportionally overestimated if porosity is overestimated (cf., Table 3.3). To discuss the effect of porosity on age estimation, we assume average carbonate rocks for the bedrock in the following estimates, and sample 03 is not included when average ages are calculated, because of its relative much younger age.

Lower effective porosity limit in carbonate rocks of 0.1% [Croff et al., 2003] yields an average water residence time of 15 ± 1 year and the age of sample 03 is 2 ± 1 years. Based on these ages, we can conclude that sample 03 exhibits a consistent $^3He_{trit}$ level and ^{4}He age. The other samples exhibit average ages between 12 and 19 years, suggesting these samples are a mixture of old water which has accumulated crustal ^{4}He and extremely recent water which diluted $^3He_{trit}$ and ^{4}He dissolved in the old water. Such a low porosity value, however, is highly unlikely and is simply representative of a lower limit for reference. If one assumes the highest effective porosity limit in carbonate rocks of 5% (Croff et al., 2003), the He based average age is 810 ± 30 years and that of sample 03 is 90 ± 40 years. As this porosity represents the highest effective porosity value in limestone and dolomite, these ages are considered as an upper limit for reference. This estimate suggests that all of the AGMW samples are composed of a mix

between pre-bomb test era water and extremely young/present time water and point to GMW ages from the AG likely of a couple of hundred years on average at most.

Previous studies have suggested that in aquifer systems, a significant external radiogenic ^{4}He component is produced in the crystalline basement underneath the sedimentary strata [e.g., Torgersen and Ivey, 1985; Castro et al., 1998a, 1998b; Ma et al., 2005, 2009]. At our study site, the Precambrian rocks underneath the sedimentary strata are also likely to contribute to the radiogenic ^{4}He present in the subglacial meltwater. For comparison, we estimate also an age based on the contribution from Precambrian rocks, by using U and Th concentrations of the average upper continental crust, which is very similar to that of Archean granites and gneisses which are present in the eastern slope of the Canadian Shield [Cameron and Garrels, 1980]. In these calculations, we assume porosity average values of 2.5% for dense crystalline rocks and 5% for fractured crystalline rocks [Domenico and Schwartz, 1998]. Calculations using porosity values of 2.5% and 5% lead to average water residence times of 200 ± 10 years and 410 ± 10 years, respectively, values that are slightly higher than those estimated from carbonate rocks' production but within the same order of magnitude. However, these assumed average porosities are total porosities. Effective porosities in the average upper crust are expected to be lower and would lead to younger water residence time estimates.

These estimates indicate that differences between extreme U and Th compositions, i.e., in carbonates, highly depleted in Th with respect to the overall upper continental crust affects the estimates of water residence times by a factor of about 2. U and Th concentrations, however, are not the main parameter impacting He based water residence time estimations; formation porosity is with the potential to affect the estimates by a factor of about 50.

With these estimates, we can conclude with a significant level of confidence that, although relatively young, i.e., likely tens to hundreds of years old (Table 3.3), the bulk of our AGMW is likely older than the atmospheric bomb-test era and it likely results from a mixture between pre-bomb and present time GMW. Measurements on the porosity under the Athabasca Glacier are needed to further constrain the values of water residence times and to confirm whether the AGMW is older than the bomb-test era or very recent, together with the constraints set by $^3He_{trit}$ analyses.

Residence times based on U-series (^{222}Rn, ^{238}U, and $^{234}U/^{238}U$) measurements are available for a total of 29 days in May and July of 2011 (Arendt, 2015). Only five are listed in

Table 3.3 when a sample for noble gas analyses is available. Overall, the age estimates based on U-series measurements range from 0 to 30 years, significantly lower than those based on He. Additional studies on other tracers are required in order to further constrain the water residence times and compare among different techniques.

3.7 Conclusion

This study uses stable noble gases' (He, Ne, Ar, Kr, and Xe) concentrations and isotopic ratios from the Athabasca Glacier meltwater in an attempt to identify the original source location of ice melt and the relative contributions of modern surface melt versus basal ice melt and/or groundwater, and to estimate first order water residence times of the GMW resulting from a mixture of modern surface and basal melt and/or groundwater. Overall, noble gas concentrations and patterns exhibited by AGMW display similar patterns to those of GrIS GMW [Niu et al., 2015]. Two patterns are apparent, with one group of samples displaying a mass- dependent depletion pattern with stronger depletion of the heavier noble gases compared to the lighter ones. The second group displays a relative Ne depletion with respect to Ar and, in some cases, with respect to Kr and Xe. Ratios of gas concentrations indicate that samples are not in equilibrium with the atmosphere at any temperature, and noble gas concentrations should reflect the equilibration altitude in the glacial environment as the temperature of water is unlikely to be much higher than the freezing point of water. Xe concentrations suggest that all samples equilibrated with the atmosphere at altitudes between 2500 m and 3400 m, values compatible with the local topography. Over half of the samples display Xe equilibration altitudes above the maximum altitude of the AG, suggesting that a significant portion of the current melt- water underneath the AG originates from the Columbia Icefield.

All AGMW samples are largely dominated by surface melt as opposed to basal ice melt. Surface melt represents at least 71% – 96% of the total GMW. Basal melt and/or groundwater represent at most 4% – 29% of the total GMW. All AGMW samples exhibit tritiogenic ^{3}He levels between 0 and 12 TU. Three scenarios could potentially lead to the estimated tritiogenic ^{3}He levels: (1) AGMW samples are older than the bomb-test era so that they contained solely background tritium levels (5 TU) at the time of ice formation; (2) AGMW samples are all extremely recent and are representative of present time so the ^{3}H has not yet decayed to the ^{3}He levels seen in our samples; (3) AGMW samples represent a mixture of the pre-bomb, bomb, or

post-bomb-era water and present day water, the latter having diluted the tritiogenic ^{3}He brought by the former component. Given that surface meltwater is routed to the base of the glacier through vertical crevasses, it is likely that ice from different depths, which formed at different time periods, is being partially melted and incorporated in the meltwater collected in the terminus area. Thus, scenario (3) is more likely.

Calculated AGMW residence times are dependent both on bedrock U and Th concentrations and porosity. The latter is the main factor impacting first order groundwater residence times. Assuming a typical effective porosity of 1% [Croff et al., 2003] and average U and Th composition in carbonate rocks leads to an average AGMW residence time of 160 ± 5 years with the exclusion of one present day sample. Overall AGMW is likely to result from a mixture between pre-bomb and modern GMW.

3.8 Acknowledgments

We thank Dr. Michael Kersten and Dr. Sarah Fortner for their editorial handling of this manuscript, as well as Dr. Thomas Darrah and an anonymous reviewer for their thoughtful and constructive reviews. Financial support by the University of Michigan, the NSF Hydrological Sciences [award EAR-1344357], and the Packard Foundation is greatly appreciated. We thank Sarah Aarons for assistance in the field.

CHAPTER IV

Noble gas signatures in the Island of Maui, Hawaii: Characterizing groundwater sources in fractured systems[1]

Abstract

Uneven distribution of rainfall and freshwater scarcity in populated areas in the Island of Maui, Hawaii, renders water resources management a challenge in this complex and ill-defined hydrological system. A previous study in the Galápagos Islands suggests that noble gas temperatures (NGTs) record seasonality in that fractured, rapid infiltration groundwater system rather than the commonly observed mean annual air temperature (MAAT) in sedimentary systems where infiltration is slower thus, providing information on recharge sources and potential flow paths. Here we report noble gas results from the basal aquifer, springs, and rainwater in Maui to explore the potential for noble gases in characterizing this type of complex fractured hydrologic systems. Most samples display a mass-dependent depletion pattern with respect to surface conditions consistent with previous observations both in the Galápagos Islands and Michigan rainwater. Basal aquifer and rainwater noble gas patterns are similar and suggest direct, fast recharge from precipitation to the basal aquifer. In contrast, multiple springs, representative of perched aquifers, display highly variable noble gas concentrations suggesting recharge from a variety of sources. The distinct noble gas patterns for the basal aquifer and springs suggest that basal and perched aquifers are separate entities. Maui rainwater displays high apparent NGTs, incompatible with surface conditions, pointing either to an origin at high altitudes with the presence of ice or an ice-like source of undetermined origin. Overall, noble gas signatures in Maui reflect the source of recharge rather than the expected altitude/temperature relationship commonly observed in sedimentary systems.

[1]Citation: Niu, Y., Castro, M. C., Hall, C. M., Gingerich, S. B., Scholl, M. A., and Warrier, R. B. (2017b). Noble gas signatures in the Island of Maui, Hawaii: Characterizing groundwater sources in fractured systems. *Water Resour. Res.*, *53*, 3599–3614, doi:10.1002/2016WR020172.

4.1 Introduction

Volcanic systems and tropical basaltic islands in particular, typically have complex internal structures and challenging access, are often poorly characterized with respect to groundwater resources and frequently suffer from freshwater scarcity. The Hawaiian Islands and Maui in particular have extreme variations in the amounts and spatial distribution of rainfall, adding to the freshwater shortage problem in some of the most densely populated areas of the island. The State of Hawaii's Commission on Water Resource Management has been addressing far more Maui-related petitions and contested hearings than for any other island in the Archipelago [Wallsgrove and Penn, 2012]. Thus, groundwater resource assessments and a thorough understanding of the hydrologic system on Maui are urgently needed. Current knowledge of groundwater-surface water relationships in the area is limited and calls for a better understanding of this complex hydrogeological system so that management of water resources can be improved [e.g., Gingerich, 1999a, 1999b; Scholl et al., 2002].

The study of stable noble gases (He, Ne, Ar, Kr, and Xe) dissolved in groundwater can enhance our understanding of surface and groundwater dynamics by providing indications on flow paths, connectivity between aquifers, and water residence times [e.g., Andrews, 1985; Ballentine et al., 1991; Mazor and Bosch, 1992; Castro et al., 1998a, 1998b, 2000; de Marsily et al., 2002; Kulongoski et al., 2003; Patriarche et al., 2004; Castro et al., 2007; Ma et al., 2009; Müller et al., 2016]. In addition, noble gases are conservative tracers and their concentrations in the recharge areas of groundwater systems are typically considered to be mostly a function of temperature, pressure (altitude of recharge area), and excess air (EA). Consequently, noble gas temperatures (NGTs) have commonly been regarded as a potentially robust indicator of past climate [Stute and Schlosser, 1993; Ballentine and Hall, 1999; Aeschbach-Hertig et al., 2002; Kipfer et al., 2002; Castro and Goblet, 2003; Kulongoski et al., 2004; Sun et al., 2010; Castro et al., 2012; Aeschbach-Hertig and Solomon, 2013].

NGTs derived from groundwater are generally assumed to reflect the mean annual air temperature (MAAT) and pressure conditions at the base of the aerated zone [Stute and Sonntag, 1992]. This is one of the key assumptions associated with the application of noble gases in paleoclimate reconstructions. Although this assumption has been verified through field experiments in sedimentary systems [Klump et al., 2007], it may not hold true in mountain groundwater flow systems [e.g., Manning and Solomon, 2003]. Indeed, due to the presence of

preferential flow paths in fractured systems leading to rapid infiltration, it is plausible that recharge water in these systems might reflect the temperature of the ground surface at the precise time of infiltration rather than the MAAT [Warrier et al., 2012], as is commonly assumed in sedimentary systems. If this is the case, noble gases in fractured and karstic areas with thin soil cover and rapid rainwater infiltration will record seasonality, and thus, should also provide us with information about the timing of recharge. Information on recharge sources might also be provided in areas with distinct water sources, e.g., local orographic rain and fog versus synoptic-scale rain, such as on the Island of Maui, if the respective noble gas end-members for these sources are known.

Although groundwater noble gas studies have been systematically conducted in sedimentary systems for decades, few studies have been carried out in fractured media. Among these are studies in the Yellowstone [e.g., Kennedy et al., 1985, 1988; Gardner et al., 2010] and the Cascades Volcanic Arc [James et al., 2000; Saar et al., 2005], the islands of R eunion [Marty et al., 1993], Cape Verde [Heilweil et al., 2009, 2012], Azores [Jean-Baptiste et al., 2009], Galapagos [Warrier et al., 2012], and the Canary Islands [Marrero-Diaz et al., 2015]. How- ever, with the exception of Gardner et al. [2010], Heilweil et al. [2012], and Warrier et al. [2012], most studies did not take advantage of information provided by NGTs. The main goal of this study is to explore the information noble gases can provide in rapid rainwater infiltration systems, i.e., in fractured or karstic groundwater flow environments. Here we assess whether NGTs can be applied to these systems to estimate both the location and timing of recharge by taking advantage of the temperature dependency of noble gas solubility. In addition, a first attempt is made to explore the relative contributions of different water sources, i.e., fog, orographic and synoptic-scale rain. For example, measurement of noble gases in a few rainwater samples in Israel during the 1970s indicated that rainwater can retain air-saturated water (ASW) values acquired in the atmosphere at high altitudes and low temperatures [Mazor, 1972]. More recently, Warrier et al. [2013] further suggested that rainwater is not in equilibrium with surface conditions and pointed to a potential linkage between the noble gas composition in rainwater and distinct weather patterns including the pres- ence or absence of fog. Additional studies are needed on both unknown (fog) and poorly understood recharge end-members (e.g., local orographic versus synoptic-scale rain), all of which are present on the Island of Maui.

4.2 Geologic, Climatologic, and Hydrologic Background

Maui is the second biggest island of the Hawaiian Archipelago which is located in the Pacific Ocean about 4000 km off the coast of California (Figure 4.1). The island is composed of two volcanoes, which are mainly basaltic in composition. The smaller and older West Maui Volcano [altitude 1764 m; Poland et al., 2014] consists of the Wailuku Basalt, Honolua Volcanics, and Lahaina Volcanics. The bigger and younger volcano, Haleakalā (altitude 3055 m), forms East Maui [Stearns and Macdonald, 1942; West et al., 1987; Bergmanis et al., 2000; Poland et al., 2014] with K-Ar ages for the oldest formation of Haleakalā, the Honomanu Basalt, ranging from 1.10 ± 0.05 to 0.97 ± 0.04 Ma [Chen et al., 1991]. Radiocarbon ages for the youngest eruptions, the Hāna Volcanics, range from 200 ± 15 to 45,000 ± 1,800 years B.P. [Bergmanis et al., 2000]. There is no known hydrothermal activity in East Maui at present, although there was evidence for low-temperature (24–35°C groundwater) hydrothermal systems on the leeward side of West Maui in the 1930s [Kennedy, 1985; Thomas, 1989]. Fercho et al. [2015] suggested the possibility of finding a robust hydrothermal system on Maui, but could not

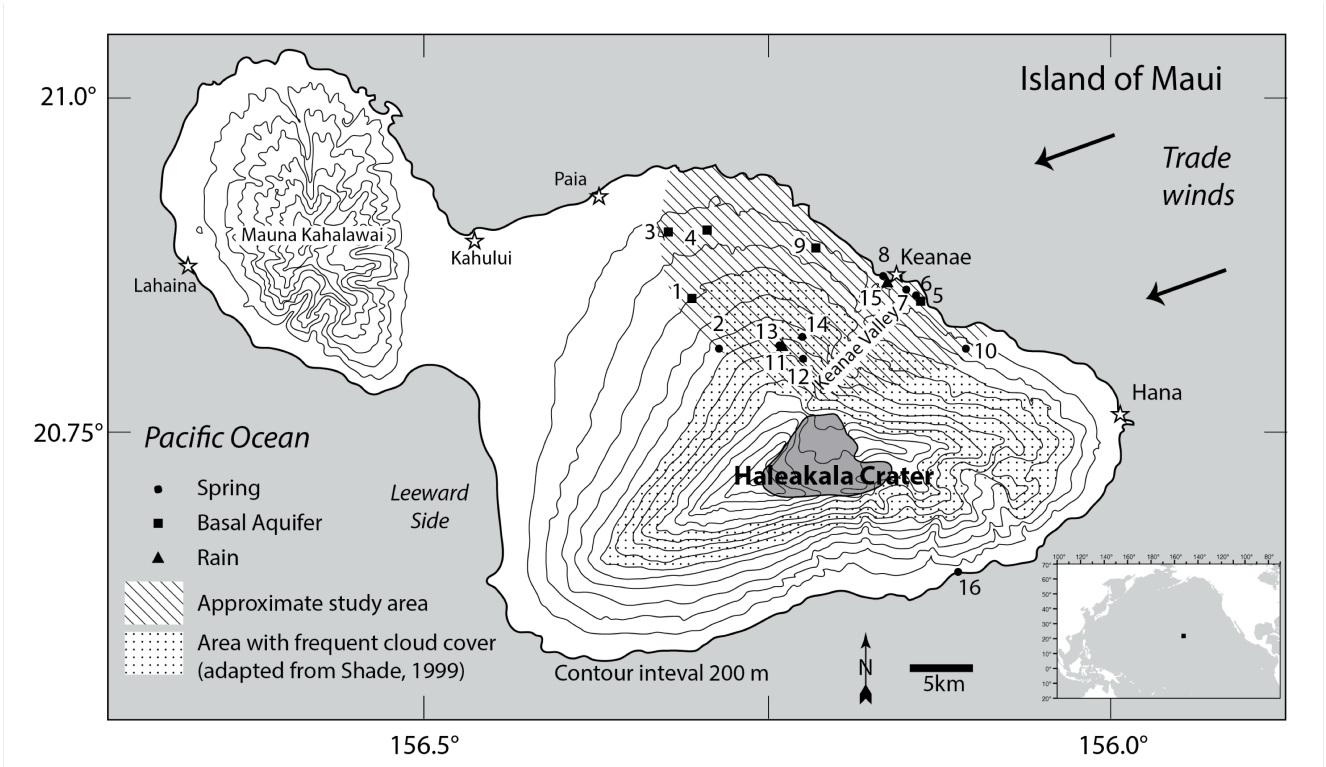

Figure 4.1 Map of the Island of Maui with approximate sampling locations (Modified from Gingerich et al. [1999a] and Scholl et al. [2007]). The square marker in the inset map shows the approximate location of Maui relative to the continents.

confirm its presence.

The Hawaiian Islands lie within the tropical trade wind belt and generally have a pleasant climate [Sanderson, 1993; Lau and Mink, 2006]. The mean annual air temperature (MAAT) in Maui ranges from 24.4°C at Lahaina near sea level (14 m) and 24.2°C at Kahului (14 m) to about 10°C at the Haleakalā summit [3055 m; Nullet and Sanderson, 1993; http://www.ncdc.noaa.gov/qclcd/QCLCD], yielding an average lapse rate in the island of about 4.7°C/km, the rate at which atmospheric temperature decreases with an increase in altitude. On average, annual variation (summer to winter) in air temperatures in Hawaii is about 4–5°C [Nullet and Sanderson, 1993]. Average air temperature at Kahului Airport, situated at 16 m above sea level (asl) was 23.5°C in spring (March, April, and May) 2005–2013 and 24.2°C in spring 2014. The average of daily maxi- mum air temperature in May 2014 was 30.1°C, and in the spring seasons between 2005 and 2014, the highest monthly average of daily maximum air temperature of 30.6°C occurred in May 2013 (http://www.ncdc. noaa.gov/qclcd/QCLCD). Climate on the windward side is dominated by trade winds which blow from the east-northeast generally 90% of the days during summer time, and 40–60% of the time in winter months [Blumenstock and Price, 1967; Sanderson, 1993; Garza et al., 2012; Wallsgrove and Penn, 2012]. Trade winds drive the majority of orographic rainfall which occurs mostly on the windward side of the islands. Rainfall above 2000 m is mostly from synoptic-scale storms [Schroeder, 1993]. On the windward side, the cloud belt extends from 600 to 2500 m [Giambelluca and Nullet, 1991; Loope and Giambelluca, 1998; Barnes et al., 2016] with the highest rainfall (11 m yr^{-1}) at 1600 m, 3 m yr^{-1} at 2300 m and <1 m yr^{-1} at the summit [Loope and Giambelluca, 1998; Scholl et al., 2002].

Orographic rainfall occurs when moist air is lifted along the windward slopes of Northeast Maui [Scholl et al., 2002], and it occurs the most at altitudes above 900 m asl [Wallsgrove and Penn, 2012]. Leeward areas receive most of their rainfall from winter cold fronts and low-pressure cyclonic (Kona) storms. In contrast to orographic rain, these storms tend to cover larger areas, but occur less frequently [Wallsgrove and Penn, 2012]. Synoptic-scale rain systems may extend several kilometers up into the atmosphere, with lower temperatures and ice as part of the precipitation process [Chu et al., 1993; Scholl et al., 2007]. Fog is a prominent feature on the windward slope of Northeast Maui and thought to be most frequent between 1000 m and 1900 m asl [Kitayama and Mueller-Dombois, 1994].

A radial drainage system is present in Northeast Maui with a dense network of stream valleys from the Haleakalā summit to the ocean [Gingerich, 1999a, 1999b]. Much of this drainage system has historically been collected in tunnels and drains and transported to other areas of the island for irrigation and municipal use [Gingerich, 1999b; Scholl et al., 2002]. Streams tend to be perennial at higher altitudes, but some go dry near the coast where they sink into the valley bottom. Streams are fed by springs at higher altitudes, runoff, and base flow, in addition to direct rainfall and fog drip [Gingerich et al., 1999b].

The lower Honomanu Basalt has higher hydraulic conductivity values than the overlying Kula Volcanics. Traditionally, the conceptual model was that most groundwater in the Hawaiian Islands occurs either as perched high-level water held up by relatively low-permeability units, or as freshwater lenses (basal aquifer system) floating on denser, underlying saltwater near sea level, or in limited areas, as dike-impounded aquifers [Gingerich, 1999b]. In northeast Maui, west of Keanae Valley (Figure 1), rocks beneath the contact between the Kula Volcanics and the underlying Honomanu Basalt and above the freshwater lens are thought to be unsaturated [Gingerich, 1999b; Scholl et al., 2002], with the basal aquifer system recharged through the discontinuous perched high-level water [Gingerich, 1999b]. The question as to whether or not high-level aquifers are perched or fully saturated down to sea level remains open. East of Keanae Valley, it was concluded that the rocks are saturated to over 600 m asl [Gingerich, 1999a; Scholl et al., 2002]. Ground- water recharge occurs directly by infiltration of rainfall and fog drip, which results from the impact of cloud droplets on vegetation. Fog was found to be a significant component of recharge to the mountain forests of East Maui. High and low altitude springs are a common feature of northeast Maui [Stearns and Macdonald, 1942]. Municipal and private groundwater wells are present in the basal aquifer and perched aquifers. Groundwater withdrawal from the perched aquifers is of concern due to the potential negative impact on streamflow.

4.3 Sampling and Analytical Procedures

A total of 27 water samples were collected at 16 sites on the Island of Maui in June 2014 for measurement of He, Ne, Ar, Kr, and Xe concentrations and their respective isotopic ratios (Figure 4.1 and Table 4.1). These include five wells tapping the basal aquifer, eight springs at different altitudes, seven on the windward side and one on the leeward side, as well as three

Table 4.1 Sampling location, sample type, measured water temperature, ambient air temperature, noble gas concentrations, R/R_a values, R_{exc}/R_a values, atmospheric He concentrations, and ratios of atmospheric He and Ne and their associated errors. Noble gas concentrations are presented in cm^3 per gram of water at STP. For samples 5a, 5b, 6a, 6b, 10a, 10b, and 16, atmospheric He concentrations (column "Atm. He 10^{-8}") are the sum of ASW and EA components (Appendix B1). For other samples, atmospheric He concentrations are measured total concentrations and are left blank in column "Atm. He 10^{-8}", and a Ne/He ratio is calculated based on measured Ne and He concentrations for these samples. Noble gas concentrations in ASW are given for an altitude of 0 m and temperatures between 15 and 30°C.

Sample Type and Number	Location	Latitude (North)	Longitude (West)	Elevation (m)	Water Temperature (°C)	Air Temperature (°C)	He 10^{-8}	Ne 10^{-7}	Ar 10^{-4}	Kr 10^{-8}	Xe 10^{-9}	R/R_a ($\pm1\sigma$)	R_{exc}/R_a ($\pm1\sigma$)	Atm. He 10^{-8}	Ne/He	Ne/He error (1σ)
Well																
1a	Pookela	20˚50'55"	156˚18'20"	581	18.5	26.7	4.55	1.81	2.87	6.25	8.14	1.04 (0.04)	-	-	3.97	0.08
1b							4.70	1.82	2.82	6.21	8.04	1.00 (0.01)	-	-	3.88	0.08
3a	Haiku	20°53'59"	156°19'29"	247	19.5	32.5	4.61	1.76	2.65	5.59	7.68	1.00 (0.01)	-	-	3.82	0.08
3b							4.62	1.79	2.76	5.87	8.24	1.07 (0.01)	-	-	3.86	0.08
4a	Kaupakalua	20°54'8"	156°17'13"	1233	20.0	26.5	5.29	1.87	2.62	5.75	7.84	1.02 (0.01)	-	-	3.54	0.07
4b							4.59	1.73	2.68	5.91	8.22	1.04 (0.02)	-	-	3.78	0.08
5a	Keanae	20°50'53"	156°8'7"	65	19.0	28.6	5.66	1.91	2.95	6.48	9.06	1.95 (0.02)	6.83 (0.96)	4.72		
5b							5.68	1.96	3.06	6.05	9.52	1.75 (0.02)	6.58 (3.16)	4.91		
9a	Ohanui	20°53'23"	156°13'0"	254	20.5	26.0	4.59	1.69	2.48	5.25	6.91	0.98 (0.01)	-	-	3.69	0.07
9b							4.69	1.86	2.99	6.48	9.32	0.93 (0.02)	-	-	3.97	0.08
Spring																
2	Waihou	20°48'21.20"	156°17'11.88"	1038	18.0	-	4.05	1.58	2.46	5.09	6.80	0.96 (0.02)	-	-	3.89	0.08
6a	Ohia	20°51'3.38"	156° 8'31.96"	63	17.9	-	5.11	2.00	3.10	6.81	9.35	1.29 (0.02)	9.90 (6.31)	4.93		
6b							5.16	2.06	3.30	7.27	10.5	1.35 (0.01)	13.7 (11.7)	5.01		
7	Keanae	20°51'29.505"	156°8'52.604"	6	20.9	-	4.52	1.85	2.96	6.38	8.37	1.01 (0.01)	-	-	4.09	0.08
8	Homomanu	20°51'37.49"	156°10'5.12"	0	21.7	29.4	4.51	1.72	2.60	5.61	7.79	0.99 (0.01)	-	-	3.82	0.08
10a	Big Spring	20°48'47.15"	156° 6'22.21"	189	15.3	26.5	8.97	1.94	3.32	7.40	10.5	3.82 (0.06)	6.89 (0.30)	4.66		
10b							8.36	1.97	3.39	7.71	11.1	4.27 (0.03)	8.49 (0.38)	4.70		
12a	Honomanu	20°48'11.954"	156°13'16.936"	1286	15.7	17.2	3.93	1.51	2.35	4.93	7.02	0.96 (0.01)	-	-	3.84	0.08
12b							3.94	1.47	2.21	4.65	6.45	1.00 (0.01)	-	-	3.73	0.07
14	Lower Kula Spring	20°49'28.808"	156°13'20.382"	939	16.4	19.5	4.24	1.69	2.81	6.29	9.10	0.94 (0.01)	-	-	3.99	0.08
16	Mokulau	20.64° *	156.11° *	0	19.2	27.1	4.54	1.55	2.21	4.52	5.75	1.32 (0.02)	4.20 (0.86)	4.06		
Rain																
11a	Waikamoi	20°48'31.408"	156°13'47.642"	1286	-	19.7	3.98	1.50	2.17	4.57	5.81	1.03 (0.01)	-	-	3.76	0.07
11b							3.99	1.48	2.19	4.54	6.03	0.99 (0.01)	-	-	3.70	0.07
13a	Lower Kula Rain Site	20°48.796'*	156° 14.302'*	1230	-	18.6	4.12	1.59	2.43	5.16	7.00	1.01 (0.01)	-	-	3.86	0.08
13b							4.28	1.59	2.38	4.93	6.82	0.93 (0.01)	-	-	3.71	0.07
15a	Road to Hana	20.86° *	156.16° *	71	-	25.0	4.42	1.72	2.53	5.39	6.94	0.97 (0.01)	-	-	3.89	0.08
15b							4.58	1.66	2.32	4.70	6.22	0.98 (0.01)	-	-	3.62	0.07
ASW																
15°C							4.55	1.93	3.45	7.94	11.2				4.24	-
20°C							4.48	1.85	3.12	6.98	9.57				4.13	-
25°C							4.41	1.78	2.84	6.20	8.27				4.04	-
30°C							4.36	1.72	2.60	5.54	7.22				3.94	-
Air							-	-	-	-	-				3.47	-

* from handheld GPS unit

rainwater samples from three distinct precipitation events. Samples were collected at altitudes between sea level and 1300 m asl with collection water temperatures ranging between 15.3 and 21.7°C.

Basal aquifer wells were sufficiently purged before sample collection to ensure the collection of formation water instead of recent precipitation in the well casing. The purge was considered completed when pH and electrical conductivity reached equilibrium. Groundwater samples were collected in standard refrigeration grade 3/8" copper tubing and cold-sealed using steel pinch-off clamps [Weiss, 1968] after water was allowed to flow through the system for 10 min. Rainwater was collected on a tarpaulin and transferred to a 0.5 L plastic bottle before being transferred to copper tubing in the field. The transfer of rainwater from the tarpaulin to the copper tubing took up to approximately 20 min. During this time, we expect that at least partial equilibration at surface collection conditions occurred. The noble gas analyses were performed in the Noble Gas Laboratory at the University of Michigan. Additional sampling, extraction, and purification procedures can be found in Castro et al. [2009] and Wen et al. [2015]. Analysis procedures are described briefly below.

After the extraction and purification phases, noble gases were trapped in a computer-controlled cryo-separator at 10 K. Subsequently, He, Ne, Ar, Kr, and Xe were sequentially released from the cryo-separator at temperatures of 42, 80, 205, 215, and 280 K, respectively, and allowed to enter a Thermo Scientific® Helix SFT mass spectrometer. Specifically, at the He release temperature, He was introduced into the mass spectrometer and the signal intensity of ^{4}He is determined for the He concentration estimate. This estimate was then used by the automated system to optimize the amount of He introduced for measurement of the ^{3}He/^{4}He ratio.

Complete measurement procedures involve estimating the concentration of each noble gas component as well as measuring He, Ne, Ar, Kr, and Xe isotopic ratios. Standard errors for concentrations are 1.5%, 1.3%, 1.3%, 1.5%, and 2.2%, respectively. First, a portion of a known volume of air was introduced into the molecular sieve section of the extraction system, and all noble gases were measured in turn with the mass spectrometer. This calibrated the mass spectrometer signal size for each noble gas. Subsequent to the air calibration run, the same measurement procedure was performed on a portion of the unknown sample. Except for ^{3}He, which was measured using an electron multiplier in ion counting mode, all noble gas isotopes

were measured using a Faraday detector.

4.4 Results

Figure 4.2a displays total noble gas concentrations for all samples normalized to ASW values corresponding to measured water temperatures for the basal aquifer and spring samples and to atmospheric temperatures for rainwater samples at the time of sample collection and at collection altitude (Table 4.1). Figure 4.2b displays the same normalized data except for measured He concentrations from which a significant mantle component was removed for samples 5a, b, 6a, b, 10a, b, and 16 (Appendix B1). Except for He, all isotopic ratios for all gases are atmospheric within a 2-sigma error. In order to highlight processes that control the

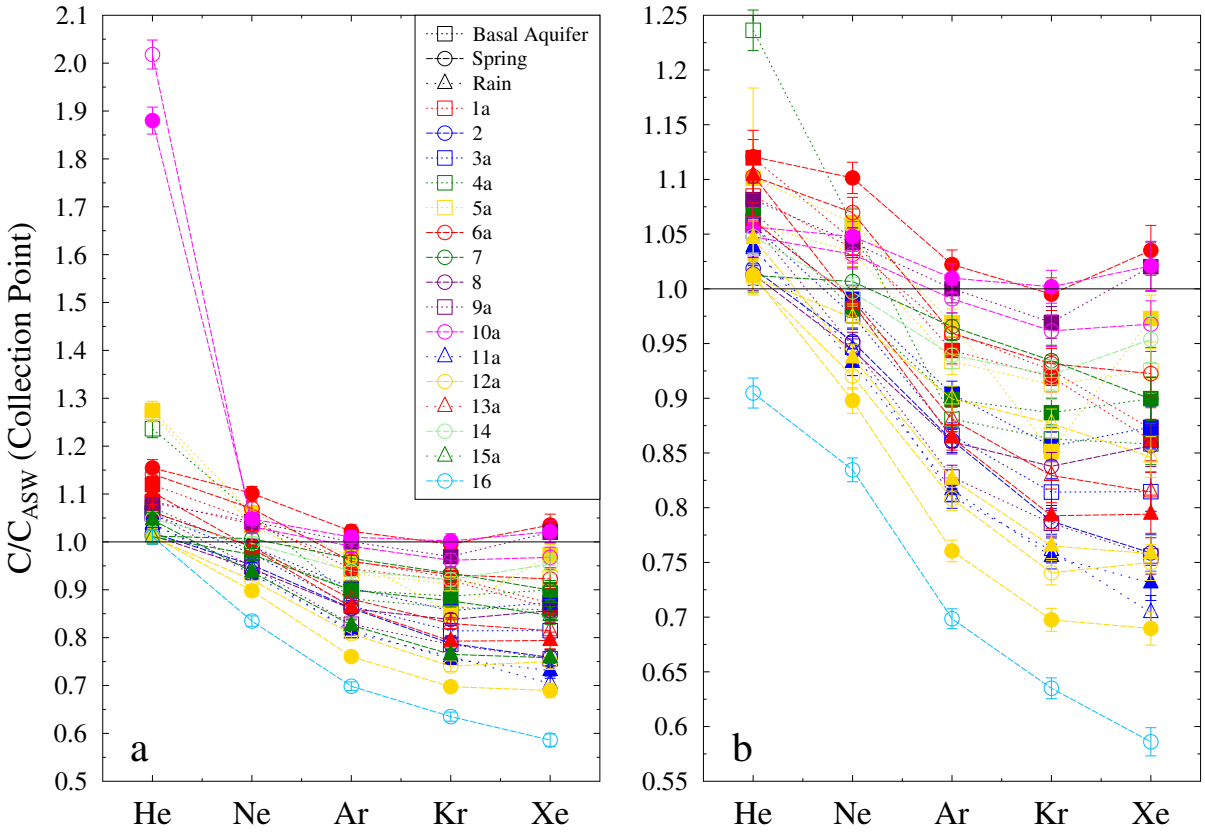

Figure 4.2 (a) Total measured noble gas concentrations normalized to ASW at collection temperatures (ambient air temperature for rainwater samples and water temperature for basal aquifer and spring samples) and altitudes. The solid black line indicates noble gas concentrations with no addition or loss of noble gases compared to ASW. Open symbols are for the first sample at each site and closed symbols in the same color are for the second sample, if applicable. (b) The mantle He component for samples from sites 5, 6, 10, and 16 are removed from the total He concentrations, and the atmospheric He components are normalized to ASW at collection temperatures. The keys are the same in both panels.

incorporation of noble gases from the atmosphere, Figure 4.2b displays only the atmospheric concentrations for all gases. It is apparent that most samples display depletion of all heavy (Ar, Kr, and Xe) noble gases. These deviations from ASW values ($C/C_{ASW} = 1$) suggest that most samples were not in equilibrium with the atmosphere under sample collection conditions. Five samples, samples 7, 8, 12a, 12b, and 15a exhibit He concentrations corresponding to those of ASW values ($\pm 1\sigma$), sample 16 displays a He depletion of 10%, while all other samples display atmospheric He excesses varying between 2% and 23% with respect to ASW values.
Ne enrichment in groundwater is generally linked to the presence of air bubbles that become incorporated in groundwater due to rapid fluctuations of the water table [Heaton and Vogel, 1981]. Ten samples are enriched in Ne, four are in equilibrium and 13 are depleted. As expected, given that rainwater samples were never below ground and subject to the incorporation of air bubbles below the water table, none of the rain- water samples exhibit Ne enrichment. Most samples exhibit Ar depletion ranging between 3% and 31%, three samples (9b, and 10a, b) are in apparent equilibrium, and sample 6b is enriched by 2%. Most samples display Kr depletions ranging between 3% and 26%, while Kr in samples 6b and 10b are apparently equilibrated with the atmosphere. Similarly, most samples exhibit Xe depletions ranging between 3% and 34%. Sample 6b presents a Xe concentration 3% higher than the ASW value and samples 9b and 10b display Xe concentrations in apparent equilibrium with the atmosphere at collection point. For most samples, a general mass-dependent pattern, where heavier noble gases are more depleted than the lighter ones, is observed. This mass-dependent depletion pattern was previously observed in Michigan rainwater and suggested to be linked to weather patterns [Warrier et al., 2013].

The origin of the He excesses is constrained through measured R/R_a and estimated R_{exc}/R_a values (Table 4.1), where R is the measured $^3He/^4He$ ratio in the samples, R_a is the atmospheric ratio and R_{exc} is the ratio from which the ASW and EA components are excluded (Appendix B1). Measured R/R_a values for all spring and basal aquifer samples vary between 0.93 ± 0.02 (Ohanui well, sample 9b) and 4.37 ± 0.11 (Big Spring, sample 10b), while R/R_a values for rainwater samples vary from 0.93 ± 0.01 to 1.03 ± 0.01. The R/R_a values for rainwater samples are close to the atmospheric value ($R/R_a = 1$), while all samples from sites 5, 6, 10, and 16 register R/R_a values higher than the atmospheric ratio ($R/R_a > 1$). Most samples yield negative R_{exc}/R_a values or values that are approximately equal to the atmospheric value ($R_{exc}/R_a = 1$)

within error, indicating that the He is entirely of atmospheric origin. R_{exc}/R_a values of samples from sites 5, 10, and 16 are significantly above 1 (>1σ), the atmospheric value. Samples 6a and 6b also display concentrations significantly above those of ASW, with R_{exc}/R_a values above 1, despite the significant errors associated with these ratio values. ASW He concentration at 0 m and 15°C (Table 4.1) is the maximum He concentration expected for these samples. These elevated R_{exc}/R_a values point to the presence of a significant mantle He component in these basal aquifer and spring samples and, in particular, in sample 10 (Big Spring). The He component separation and origin of this elevated R_{exc}/R_a is discussed in detail in the supporting information (Appendix B1).

In addition to He excesses resulting from the presence of a mantle component, sites 5 and 10 display atmospheric He excesses with respect to ASW. Sample 16, the sole spring sample collected on the leeward side exhibits a He depletion level of about 10% following removal of the mantle component. It is possible that we may have slightly overestimated the mantle component of this sample. The mantle component for samples with R/R_a values significantly above 1 was estimated to be the difference between total measured He volume and the sum of ASW and EA components fitted in the NGT model (Appendix B1). This sample may have mixed with older water carrying a crustal He component (average crustal values for R/R_a vary between 0.02 and 0.05; O'Nions and Oxburgh [1983]) leading to a low estimated R_{exc}/R_a ratio.

It is apparent that samples displaying a clear and significant presence of a mantle He component (samples 5, 6, 10, and 16) are all located on the easternmost portion of Maui, both on the windward and leeward side of the island, and are all relatively low-elevation groundwater. Additional sampling in this area is needed to assess the lateral extent of this mantle He source and potential mantle activity. The geology in the area is complex, with the youngest basalt formation, the Hāna Volcanics present at or in the vicinity of these sites [Langenheim and Clague, 1987].

4.5 Discussion

4.5.1 Noble Gas Patterns and Possible Origin

From Figure 4.2b, it is apparent that rainwater samples present atmospheric He excesses and a mass- dependent pattern, with greater depletion of the heavier noble gases, characteristics previously observed in rainwater in southeast Michigan [Warrier et al., 2013]. Similarly, all basal

aquifer samples present atmospheric He excesses. The noble gas patterns yielded by rainwater and basal aquifer samples resemble each other, suggesting that the basal aquifer is likely directly recharged from rain events, as opposed to being recharged by perched aquifers. In contrast, a number of spring samples display the most extreme noble gas concentration values for Ne, Ar, Kr, and Xe, both above (e.g., 6b) and below saturation (e.g., 16) for Ne, Ar, and Xe (Figure 4.2b). In addition, as shown below, except for He, less normalized concentration variability is observed among all gases within the same spring sample. This suggests that the spring samples, most of which are representative of perched aquifers, are recharged from a variety of distinct sources. This type of signature contrasts with that of basal aquifer samples. On the other hand, it is likely that the sources of each spring are more localized, leading to more extreme concentration variations among all spring samples as compared to those observed in the basal aquifer. The observed differences between basal aquifer and spring samples suggest a physical separation between most perched aquifers and the basal aquifer or, at least, poor mixing from perched aquifers to the basal aquifer. The basal and perched aquifers are thus, likely separate entities in the area west of Keanae Valley as suggested earlier by Gingerich [1999a]. Gingerich [1999a] also suggested the groundwater system is saturated to over 600 m asl east of Keanae Valley. Because only two windward spring samples from the same site are available east of Keanae Valley (Big Spring, site 10), it is not possible at this stage to determine the aquifer connectivity to the east of Keanae Valley.

The presence of different sources of water, i.e., high-altitude rainwater and low-altitude fog droplets, with different noble gas signatures was previously hypothesized for the island of San Cristobal in the Galápagos Archipelago to partially explain the saturation anomaly observed in high-altitude springs [Warrier et al., 2012]. There, one group of samples displays a mass-dependent depletion pattern, with heavier noble gases being more depleted than the lighter ones while the other group exhibits a relative Ne depletion with respect to Ar. This Ne-Ar anomaly was later observed in rainwater in southeast Michigan [Warrier et al., 2013], and was suggested to relate to the presence of fog and weather patterns, e.g., cloud heights and rainfall amount. These previous studies point out that the observed noble gas saturation pattern may result from a mixture of different end-members as opposed to one specific end-member and this appears to be also consistent with our observations on the island of Maui.

Warrier et al. [2013] further suggested that rainwater in southeast Michigan may

originate as ice in the atmosphere at high altitudes, as the rainwater samples exhibit a pattern similar to that previously observed in ice [Top et al., 1988; Malone et al., 2010]. Indeed, because of their large atomic radii, Ar, Kr, and Xe are highly incompatible with the ice structure and their measured concentrations in Antarctic ice are, on average 15%, 11% and 10%, respectively, that of ASW at 18.7°C and 0 m [cf., Malone et al., 2010]. On average, Ne in ice is depleted by 4% while He is enriched by 50% with respect to ASW at 18.7°C and 0 m [cf., Malone et al., 2010]. The temperature of 18.7°C is the average collection water temperature of all samples collected in this study. The distinct behaviors of light versus heavy noble gases were hypothesized to explain the observed normalized concentration pattern in Michigan rainwater, and might also be applicable to the He excess as well as Ar, Kr, and Xe depletion in Maui rainwater samples. As Ne solubilities in ice and ASW are similar, this hypothesis may not explain the samples with Ne depletions higher than 4%; however, the estimated depletion or excess in this model is dependent on the assumed equilibration altitude and temperature, which might cause an estimated Ne depletion more severe than what should have been present in ice.

In order to assess whether some Maui samples might originate as ice or have an ice-like signature of undetermined origin and to determine the various degrees of equilibration reached, Maui samples (rainwater and basal aquifer, Figure 4.3a; spring samples, Figure 4.3b) are compared with average noble gas concentrations of Antarctica ice normalized to ASW values at 18.7°C and 0 m (solid gray line, Figure 4.3; Malone et al. [2010]) as well as values representing different levels of partial equilibration of noble gases with the atmosphere assuming the initial composition to be that of Antarctica ice (dashed gray lines, Figure 4.3; Warrier et al. [2013]). By "partial equilibration", we mean a simple linear mixing of gas concentrations between two end-member components, an ice-like composition [cf., Malone et al., 2010] and ASW. In fact, true equilibration is likely to be a complex function of a multitude of factors, including temperature dependent diffusion coefficients in air and water for each noble gas. However, such complexities are beyond the current scope of this study and we will instead refer to linear mixtures of ice patterns with ASW as "partial equilibration". In Figure 4.3, dashed gray lines represent different degrees of partial equilibration. For example, the dashed gray line labeled 10% just above the solid gray line, represents the noble gas composition in a mixture of 10% ASW and 90% ice, in other words, 10% of the ice has melted and equilibrated with the atmosphere. In contrast, the solid black line connecting solid black circles parallel to the horizontal axis represents water

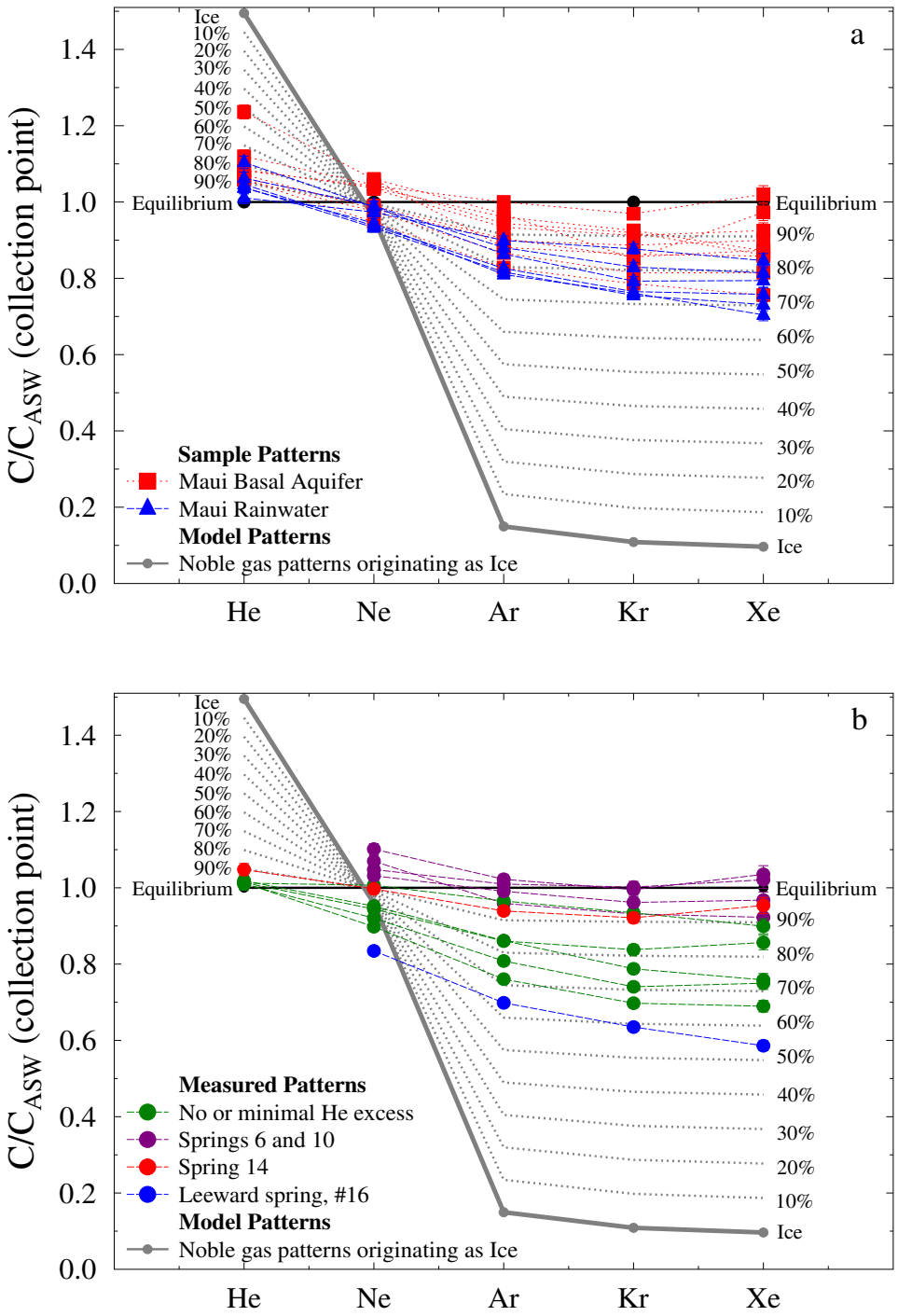

Figure 4.3 Saturation patterns of Maui samples compared with partial equilibration of ice with the atmosphere [Warrier et al., 2013]. The dashed gray line labeled 10%, represents the noble gas composition in a mixture of 10% ASW and 90% ice (mass percent), in other words, 10% of the ice has melted and equilibrated with the atmosphere. He concentrations of samples with elevated R_{exc}/R_a (samples 5, 6, 10, and 16) are not plotted. (a) Maui rainwater and basal aquifer samples; (b) Maui spring samples.

fully equilibrated with the atmosphere (ASW component). Samples with elevated R_{exc}/R_a values, i.e., samples 5, 6, 10, and 16, do not have He concentrations plotted in Figure 4.3, as their He components of non-atmospheric origin would not fit in this binary mixing model.

From Figure 4.3a, it is apparent that the Maui rainwater samples present a pattern similar to that of partially equilibrated ice with degrees of equilibration for Xe between 67% and 83%. If Warrier et al. [2013] are correct, this might suggest that some rainwater in Maui possibly starts as ice originating at higher altitudes or, alternatively, that it displays an ice-like signature of undetermined origin. The freezing altitude in Hawaii was about 5 km in July 1998 and 4.5 km in January 1998 [Harris et al., 2000] and as discussed below in detail, these are about the altitudes we expect the MAAT to be 0°C, extrapolated from MAATs in the island. Most basal aquifer samples exhibit Ar, Kr, and Xe concentrations which are consistent with a partially equilibrated ice pattern with samples varying between 76% equilibration and close to equilibrium values. The faster infiltration takes place, the greater the expected depletion level. It is also observed that overall basal aquifer samples have achieved greater degrees of partial equilibrium for Xe (76–102%) than rainwater samples (70–85%). This difference in degree of partial equilibrium indicates further equilibration may have occurred during infiltration. In contrast, in most samples, He and Ne concentrations are above those expected from the ice pattern curve, and could be due to the presence of excess air [e.g., Heaton and Vogel, 1981]. Alternatively, the presence of a mantle He component for some of these samples cannot be excluded as we were unable to determine whether or not a mantle component was present due to the large errors associated with the R_{exc}/R_a calculation of some of these samples (Table 4.1; Appendix B1). Overall, basal aquifer and rainwater samples yield similar atmospheric Ne/He ratios within error (Table 4.1). Specifically, basal aquifer sample Ne/He ratios vary between 3.54 ± 0.07 (4a) and 3.97 ± 0.08 (1a and 9b), and rainwater ratios vary between 3.62 ± 0.07 (15b) and 3.89 ± 0.08 (15a). The similar Ne/He ratios and He excess of basal aquifer and rainwater samples (all displaying atmospheric He excesses) suggest a possible direct linkage between the two types of samples.

In contrast to the basal aquifer samples, most spring samples that only contain atmospheric He display little or no He excess (Figure 4.3b). Spring samples 2, 7, 8, 12a, and 12b (green circles in Figure 4.3b) display He at ASW levels or less than 1% excess concentrations within 1σ error, while their Ar, Kr, and Xe concentrations exhibit significant depletion with

partial equilibration degrees varying between 66% and 89% (Figure 4.3b). Thus, these spring samples display a different pattern to that of rainwater, where most of the rainwater samples present 2–10% He excesses. Despite that, the Ne/He ratios for these springs have a range that overlaps that of rainwater. These springs are located either west of Keanae Valley or immediately in its vicinity (Figure 4.1). Overall, springs 6 and 10 are better equilibrated with respect to collection conditions than other springs, with concentrations normalized to ASW of Ar, Kr, and Xe deviating from equilibration by less than 8%. As samples from these two springs are fairly well equilibrated, they do not provide a possible distal water source. These springs are located to the east of Keanae Valley or near it. The different patterns dis- played by the windward spring and rainwater samples suggest these springs are not solely recharged by rainwater. Springs and their associated perched aquifers are likely to have more localized recharge sources than do the basal aquifer samples. It is also likely that the basal aquifer has a composite of many distinct source areas and has averaged spatial differences, whereas the springs from perched aquifers represent a small subset of recharge paths. Sample 16, the only sample collected on the leeward side, is the most depleted of all samples (Figures 4.2 and 4.3b), regardless of type. Because of the presence of terrigenic He sources, it is difficult to assess whether its atmospheric He component indicates a starting point as ice. The noble gas concentrations of sample 16 are consistent with a recharge source starting as ice higher up in the atmosphere with the possible addition of a minor terrigenic source with both crustal and mantle components (Appendix B1).

In summary, most windward springs that do not display elevated R/R_a values exhibit minimal He excesses and a distinct noble gas concentration pattern from that of the basal aquifer. This suggests that springs west of Keanae Valley, which are likely from perched aquifers, are largely separated from the basal aquifer, or the mixing/recharge from perched to basal aquifers is poor. It is not possible to infer the aquifer connectivity to the east of Keanae Valley due to the availability of only one sampling site (spring 10).

4.5.2 Apparent Equilibration Temperatures and Altitudes

Concentrations of atmospheric noble gases dissolved in water record various physical parameters (e.g., temperature, EA, altitude, salinity) at which final equilibration takes place. Although concentrations of all atmospheric noble gases dissolved in water decrease with

increasing temperature, their sensitivity to temperature increases with increasing atomic mass [Mazor, 1972]. Thus, while Xe concentrations are the most sensitive to temperature of equilibration, Ne concentrations are the least. When the ambient air pressure is not 1 atm, a uniform correction factor is applied to the solubility values at sea level for all noble gases [Mazor, 1972]. As the same correction factor for altitude is applied to all noble gases, the Ne/ Xe ratios in ASW are independent of altitude and are functions of temperature only. On the other hand, 1/Xe depends on both temperature and recharge altitude of equilibration. An increase in recharge altitude decreases concentrations of all dissolved noble gases due to a decrease in partial pressures of noble gases in the atmosphere. Our Maui data and the expected ASW values are compared in Figure 4 in order to place constraints on the possible equilibrium conditions indicated by the samples. The idea that Maui rainwater and basal aquifer samples are associated with high altitude and low temperatures, with possibly ice formation or at least an ice-like signature of undetermined origin is reinforced by looking at the apparent altitudes and NGTs displayed in Figure 4.4. Here calculated 1/Xe versus Ne/Xe values for a variety of altitudes (0–3000 m) and temperatures (10– 40°C) are plotted together with our Maui data. Such a simplified comparison with ASW does not account for the addition of the EA component resulting from dissolution of small air bubbles due to rapid water table fluctuations [Heaton and Vogel, 1981]. Because the presence of Ne in water is particularly indicative of the addition of EA [Herzberg and Mazor, 1979; Ozima and Podosek 2002], any addition of EA will move samples to the right-hand side of the diagram as indicated by arrows in Figure 4.4. Additional arrows illustrate how samples would deviate from ASW values if Ne is in equilibrium with the atmosphere while Xe concentrations are depleted by 10% from their ASW values. These arrows start from points corresponding to ASW values at altitudes of 1000 and 2000 m for temperatures at 15, 20, 25, and 30°C as well as temperatures at 10, 15, 20, and 25°C, respectively. A 10% Xe depletion results in a lower apparent equilibrium altitude of 300 m and an apparent equilibration temperature 4–5°C higher compared to a situation where Xe is fully equilibrated. More severe Xe depletion levels would yield proportionally lower equilibration altitudes and higher temperatures. The curved dashed pink line represents expected ASW values assuming a temperature of 31°C at sea level and a lapse rate of 4.7°C/km. This temperature was chosen as an upper limit of average temperatures observed in Maui. Indeed, the maximum air temperatures in May and June 2014 at Kahului Airport (16 m asl) were 30.1 and 30.8°C, respectively. The average maximum air

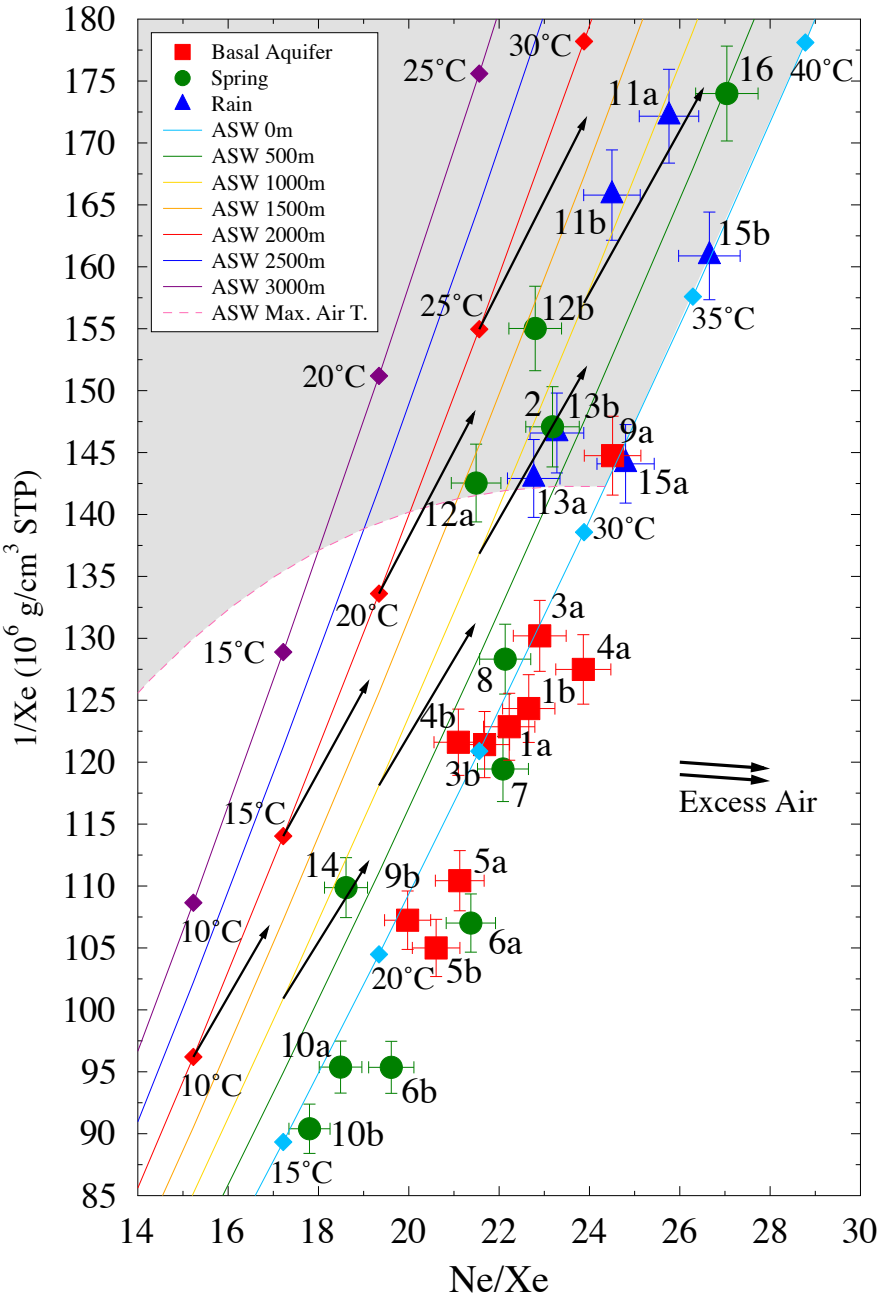

Figure 4.4 Preliminary estimation of equilibration temperatures and altitudes under the assumption that both Ne and Xe have equilibrated with surface conditions by comparing measured 1/Xe versus Ne/Xe for all Maui samples with theoretical ASW values. Colored solid lines indicate ASW values at altitudes between 0 and 3000 m asl, and colored markers indicate temperatures between 10 and 40°C. A dashed curved line indicates ASW values for average maximum air temperatures in May and June 2014, same as that of May and June 2005–2014. Shaded area marks incompatibly high temperatures. EA addition moves samples in the direction indicated by arrows. A 10% Xe depletion moves samples in the direction indicated by thin arrows originating from ASW values corresponding to temperatures between 10 and 30°C and altitudes of 1000 and 2000 m.

temperature in summer (June, July, August) 2005–2013 is 30.7°C, similar to that of June 2014. From right to left, the curved dashed pink ASW line represents progressively higher Xe concentrations (lower 1/Xe values) as altitude increases, which is caused by the decreasing temperature with increasing altitude that overwhelms the effect of decreasing partial pressure of Xe in air at increasing altitude. This means that, assuming ASW conditions, if a sample has a Xe concentration that is lower than the ASW value at its collection point (i.e., higher 1/Xe), it is not entirely because the sample originates from a higher altitude, assuming the average lapse rate on the island. The zone above the pink line is shaded, indicating apparent equilibration temperatures higher than the estimated maximum temperatures in the island. Samples plotting within this zone exhibit equilibration temperatures which are not compatible with surface conditions on Maui. Given the relative directions of the EA arrows, addition of EA moves a sample to higher apparent equilibration temperatures and lower altitudes, but it does not move a sample from the non-shaded zone to the shaded zone. In contrast, Xe depletion is the best candidate capable of moving a sample into the shaded zone where temperatures are incompatibly high with respect to surface conditions observed on the island.

Overall, samples exhibit apparent equilibration temperatures between 16°C (10b) and 36°C (15b and 16) and equilibration altitudes below 1500 m asl. Very high apparent temperatures (28–36°C) are displayed by Maui rainwater, which results from the significant depletion of heavy noble gases in these samples and point to Maui rainwater originating at high altitudes or at least displaying an ice-like signature of undetermined origin as a starting point [e.g., Warrier et al., 2013]. All of the Maui rainwater samples lie above the line of observed maximum temperatures in the area. Assuming the same lapse rate in the atmosphere as that on the island (4.7°C/km), the MAAT would decrease to 0°C at an altitude of 5.2 km. This lapse rate on the island is lower than the moist adiabatic lapse rate of 6.5°C/km [Wallace and Hobbs, 2006]. Assuming a lapse rate of 6.5°C/km above the summit of the island, the MAAT would decrease to 0°C at an altitude of 4.9 km. Both estimates are close to 5 km asl and this is close to the freezing altitude in the area [Harris et al., 2000]. Sample 16 is the only spring sample collected on the leeward side of the island, which is known to be recharged mostly through synoptic-scale storms [Giambelluca and Schroeder, 1998; Scholl et al., 2007; Giambelluca et al., 2011], i.e., rain occurring at high altitude and existing as ice during part of its history. Sample 16 displays the highest apparent equilibration temperature (36°C), which is consistent with recharge

by synoptic-scale, rather than local rainfall. This equilibration temperature is higher than or equal to those displayed by the windward rainwater samples. Specifically, all rainwater samples exhibit apparent equilibration temperatures varying between 28°C (13a) and 36°C (15b), higher than the average air temperature in May and June 2005–2014 (25.1°C) at Kahului Airport near sea level (16 m; http://www.ncdc.noaa.gov/qclcd/QCLCD). Assuming a lapse rate of 4.7°C/km, the average air temperature in June at 1286 m asl, where the highest rainwater sample was collected, is about 19.9°C, more than 8°C lower than the apparent equilibration temperature yielded by rainwater samples. This clearly indicates that heavy noble gases did not have enough time to dissolve in the rain droplets during rainwater formation, subsequent rainfall, and sample collection. As recharge occurs at a higher altitude than the collection point, the average air temperature is expected to be even lower and the discrepancy between the air temperature at recharge and the apparent equilibration temperature is thus larger. Rainwater samples from sites 11 and 15 exhibit temperatures higher than 31°C, higher than the average maximum air temperature in May and June 2005–2014 at Kahului Airport (http://www.ncdc.noaa.gov/qclcd/QCLCD), and over 6°C higher than the maximum temperature in June at 1286 m, which would be 24.8°C. These incompatibly high apparent equilibration temperatures clearly indicate that rainwater was not in equilibrium with the atmosphere at surface conditions or the conditions at spring recharge altitudes, which are higher than collection altitudes. Ne and Xe concentrations apparently reached their measured concentrations under different conditions. As the apparent altitudes are affected by Xe depletion and EA addition, the apparent altitudes are certainly lower than the real equilibration altitudes if both Ne and Xe are in equilibrium. Samples 1b, 4a, 5a, b, 6a, b, and 7 display equilibration altitudes below sea level within 1σ error, and thus, below their collection altitudes, suggesting the very likely presence of EA. Samples 1a, b, 3a, b, 4a, b, 7, and 8 plot between 25 and 30°C, temperatures over the MAAT but below the maximum temperature. This suggests that these samples are not recording the MAAT, but they retained the noble gas signatures representing high apparent temperatures.

Most of the basal aquifer samples yielded similar apparent equilibration altitudes, which are below sea level, suggesting they are well mixed compared to the springs. Most basal aquifer samples exhibit Ne excess with respect to Xe, likely resulting from incorporation of EA. Overall, rainwater samples display higher apparent equilibration temperatures than the basal aquifer samples, suggesting that here too the basal aquifer is in general better equilibrated with surface

conditions. Samples 10a and 10b plot at sea level with a 1σ error of about 350 m, which matches their collection altitude of about 200 m asl. Spring samples at sites 6 and 10, with high Xe concentrations, exhibit overall lower temperatures than the basal aquifer samples. These springs may have accumulated more noble gases because of their relatively low water temperatures and they are better equilibrated with the atmosphere than other spring and basal aquifer samples. Sample 14 exhibits an apparent equilibration altitude approximately equal to its collection altitude and a temperature lower than the local MAAT, which is compatible with surface conditions at the time of sample collection.

In conclusion, most samples yield apparent equilibration temperatures higher than the MAAT. Many samples display an addition of Ne resulting from the likely presence of EA and possibly a lack of Xe equilibration. All of the rainwater samples exhibit equilibration temperatures higher than the estimated MAAT at their collection altitudes, suggesting that they started as ice with very low heavy noble gas concentrations, especially Xe. The only leeward sample displays a very high equilibration temperature, suggesting that it is consistent with groundwater predominantly recharged by synoptic-scale rainfall from altitudes involving ice formation.

As equilibration is not always achieved by all gases, it is also useful to examine measured concentrations of Ar and Kr, in addition to Ne and Xe. Figure 4.5 shows Ar, Kr, and Xe concentrations versus Ne concentrations for all Maui samples together with Michigan rainwater samples [Warrier et al., 2013]. Expected ASW noble gas patterns for different altitudes, from sea level up to 5 km asl, as well as corresponding MAAT using sea level temperatures of 22.4, 24.4, and 26.4°C with a lapse rate of 4.7°C/km are also plotted. In addition, noble gas concentrations for ice from Lake Vida, Antarctica [Malone et al., 2010] are plotted. It is apparent that samples do not follow any of the expected theoretical curves for ASW values. Instead, samples fall along a linear pattern roughly between two likely end-members. One end-member appears to be represented by ice [Malone et al., 2010]. The addition of EA moves water samples and ice samples in the directions indicated by the arrows in plots a, b, and c. Therefore, the ice samples with lower noble gas concentrations are very likely to have less EA (e.g., air bubbles) and are closer to the pure ice or ice-like end-member. The other end-member of the Maui samples is likely an ASW component with the possible addition of a highly enriched mantle He component (Appendix B1) of which samples 10 (Big Spring; $R_{exc}/R_a = 6.89 \pm 0.30$ [10a] or 8.49 ± 0.38

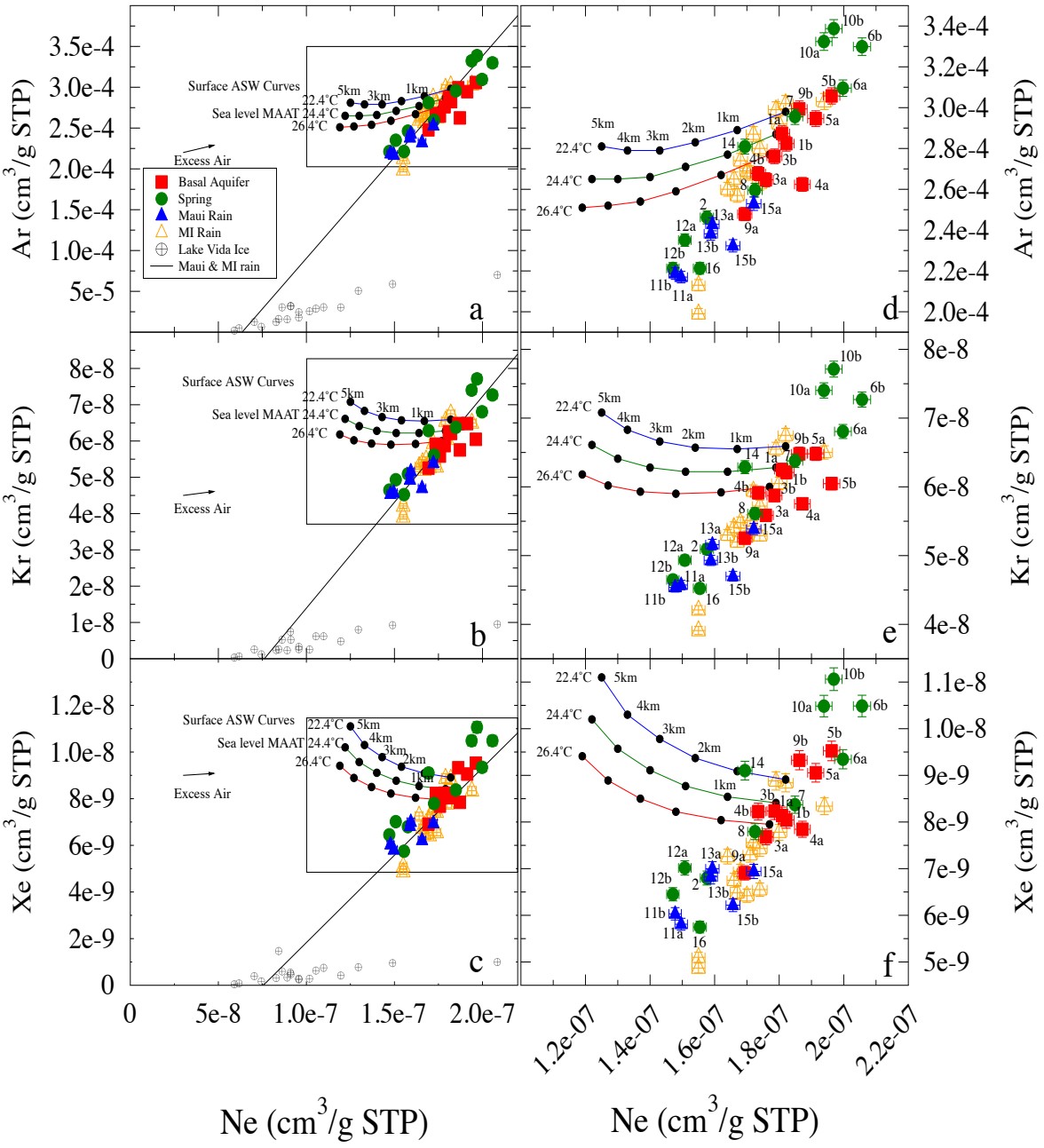

Figure 4.5 Comparison of atmospheric Ar, Kr, and Xe versus atmospheric Ne concentrations for Maui samples, together with southeast Michigan rainwater [Warrier et al., 2013] and Antarctica ice [Malone et al., 2010]. The normalized noble gas concentrations in ice are corrected for the difference in altitude between Lake Vida (340 m asl) and the likely altitude above Maui where MAAT drops to 0°C (5 km asl). (a) Ar versus Ne, (b) Kr versus Ne, and (c) Xe versus Ne. Colored curve lines indicate ASW values between sea level and 5 km asl and corresponding air temperature with a lapse rate of 4.7°C/km and temperatures of 22.4, 24.4, and 26.4°C at sea level. A least square regression line is shown for all Maui and Michigan rainwater samples. (d) Ar versus Ne, (e) Kr versus Ne, and (f) Xe versus Ne. (d–f) Zoom-in views of the corresponding plot in left column, displaying the samples relative to the ASW curves.

[10b]) and 6 (Ohia Spring; $R_{exc}/R_a = 9.90 \pm 6.31$ [6a]) are the most representative. Indeed, these samples appear, by far, to be the ones having reached the highest level of equilibration with air at the collection point altitude and measured water temperature, as previously shown in Figures 3 and 4. However, the temperature and altitude of this ASW component cannot be well determined at this stage. Nonetheless, the lowest collection water temperature in this study is that of spring 10 at 15.3°C. A least squares regression line for all Maui as well as Michigan rainwater samples is shown in Figures 4.5a, b, and c. Indeed, Michigan rainwater samples [Warrier et al., 2013], like Maui samples, do not follow an ASW pattern as expected and appear to also fall along a mixing line between two end-members, one represented by ice, the other by an undetermined ASW component. Zoom-in views of the samples are shown in the right column for the corresponding panel in the left column. It can be observed that some Michigan rainwater samples display more extreme depletion levels of the heavy noble gases as compared to Maui samples and thus, further approach the ice end-member. With respect to Maui samples, the closest samples to this end-member are the most depleted rainwater samples (11a, b) and the only spring sample collected on the leeward side (sample 16, Figure 4.5f). The leeward spring receives most of its recharge from synoptic- scale systems, so it is likely representative of groundwater predominantly from precipitation that involved ice formation. The noble gas signature of the leeward spring is consistent with that of the most depleted Michigan rainwater samples [nr3-1 and nr3-2; Warrier et al., 2013] which were collected during the passage of a mesoscale convective complex. The similarity in noble gas concentrations suggests the likelihood of a common origin of source and mechanism of the noble gas characteristics in the Maui rainwater, leeward spring, and Michigan rainwater.

Noble gas signatures of Maui rainwater samples overlap with that of a few spring samples in the linear array. This array suggests that the rainwater is continuously evolving toward equilibrium with the atmosphere as rain droplets form and fall. However, this cannot exclude the possibility of mixing with an ASW component at low temperatures for the perched and basal aquifer samples.

As previously mentioned, the other end of the spectrum is represented by spring samples that display a mantle He end-member with an R/R_a value of 8–8.5 (Appendix B1). Overall, springs 6 and 10 have the highest Ne and Xe measured concentrations of all samples and this is still consistent with the presence of mantle He in these springs. Basal aquifer samples plot in the

middle of the array, while spring samples display both extremely high and low noble gas concentrations. This is possibly because, as mentioned earlier, springs are recharged by more diverse and localized sources than the basal aquifer.

4.6 Conclusion

Results of noble gas analyses are presented from samples collected in springs, groundwater wells (basal aquifer), and rainwater on the windward side of northeast Maui. One spring sample was also collected on the leeward side. Most samples present atmospheric He excesses and a mass-dependent depletion pattern, with a greater depletion of the heavier noble gases, characteristics previously observed in spring water from the Galápagos Islands [Warrier et al., 2012] and rainwater in southeast Michigan [Warrier et al., 2013]. These patterns resemble those previously observed in ice [Top et al., 1988; Malone et al., 2010]. So far, this noble gas pattern has only been observed in fractured groundwater systems and it has been hypothesized that it is due to rapid infiltration of rainwater that prevents equilibration of noble gases with the atmosphere. Noble gas patterns yielded by rainwater and basal aquifer samples resemble each other and suggest that the basal aquifer is directly recharged from rain events as opposed to being recharged by perched aquifers. In contrast, a number of spring samples display the most extreme noble gas concentration values for Ne, Ar, Kr, and Xe, suggesting that the spring samples, most of which are representative of perched aquifers, are recharged from a variety of distinct sources. The observed differences between basal aquifer and spring samples suggest a physical separation between most perched aquifers and the basal aquifer or, at least, poor mixing/recharge from perched aquifers to the basal aquifer. The basal and perched aquifers are thus, likely separate entities in the area west of Keanae Valley as suggested earlier by Gingerich [1999a]. Connectivity between perched and basal aquifers east of Keanae Valley cannot be assessed due to the limited number of sites sampled in this area.

The easternmost spring and well sites on both windward and leeward sides of the island yield samples with a significant mantle He component and a few point to an almost pristine mantle Mid-Ocean Ridge Basalt (MORB) type signature.

From an analysis of Ne and Xe concentrations, it is clear that samples exhibit a wide range of apparent equilibration temperatures, between 16 and 36°C, and equilibration altitudes below 1500 m asl. Maui rainwater displays very high apparent equilibration temperatures (28–

36°C), incompatible with surface conditions. These result from the significant depletion of the heavy noble gases in these samples and point to Maui rainwater originating either at high altitudes or at least displaying an ice-like signature of undetermined origin [e.g., Warrier et al., 2013]. The only spring sample collected on the leeward side of the island, which is known to be recharged mostly through synoptic-scale storms, i.e., rain occurring at high altitude and existing as ice during part of its history, displays the highest apparent equilibration temperature (~36°C), consistent with an ice signature [Malone et al., 2010].

Based on Ne, Ar, Kr, and Xe concentrations, it is apparent that samples do not follow the expected theoretical curves for ASW values as commonly observed in sedimentary systems. Instead, samples fall along a linear pattern representing mixing between two likely end-members. One end-member is represented by an ice-like composition and displays a signature approaching that of ice [Malone et al., 2010]. The other end- member is likely an ASW component with the possible addition of a MORB-type mantle He component. Overall, it is apparent that in fractured, rapid infiltration systems, noble gases are providing information not on expected recharge altitudes and temperatures, as is the case of sedimentary systems where infiltration is slower, but instead, on recharge sources. Noble gases also appear to provide clues on connectivity between different types of aquifers. Further studies in fractured areas are needed to access the potential of noble gases in providing seasonality information as well as understanding the exact nature of the ice-like pattern. Development of new tracers in fracture groundwater systems is critical to improve knowledge of these complex hydrologic systems.

4.7 Acknowledgments

We thank the Editor and Associate Editor of Water Resources Research for their editorial handling of this manuscript as well as three anonymous reviewers for their thoughtful and constructive reviews. Financial support by the University of Michigan, the NSF Hydrological Sciences (award EAR-1344357), and the NSF Instrumentation & Facilities (EAR-1049822) is greatly appreciated. We thank Dave Taylor, Dean Tanimoto and Joe Mendonca at the Maui Department of Water Supply, Mark Vaught and Garret Hew at East Maui Irrigation Company, Ltd., Gladys Kanoa, and Ian Gingerich for their assistance in field.

CHAPTER V

Noble gases and water stable isotope signatures in the Island of Maui, Hawaii: Characterization of groundwater sources[1]

Abstract

A noble gas pilot study in the Island of Maui based on water samples collected from wells tapping the basal aquifer, springs from perched aquifers, and rainwater in June 2014 suggests that noble gases in rainwater and groundwater samples fall on a linear pattern between air-saturated water (ASW) and an ice-like end-member, rather than reflecting the mean annual air temperature (MAAT) as commonly observed in sedimentary systems (Niu et al., 2017b). The study presented here is a follow-up of Niu et al. (2017b), based on both the results from 2014 and a new sampling campaign in February 2016 also from the basal and perched aquifers as well as rainwater. This study assesses whether temporal variations are recorded in noble gases and water stable isotopes and explores the combined use of these two tracers to estimate the location and timing of recharge. In addition, groundwater ages based on tritium measurements from basal aquifer samples as well as a rainwater sample collected in 2014 are presented.

Noble gas signatures in basal aquifer samples are similar in both sampling campaigns, while rainwater and spring samples display temporal variations in noble gases. This is consistent with previous findings that the basal aquifer is recharged by more homogenized sources while springs are recharged by more diverse sources. He depletion with respect to ASW was observed in some 2016 rainwater and spring samples, but not in 2014. Overall, the 2016 samples exhibit greater deuterium excesses than those of 2014, an observation consistent with the drier climate during the strong 2015–2016 El Niño. Three 2016 rainwater samples display the highest deuterium excesses of all samples. Water source altitudes based on Ne for rainwater samples range from 0.1 to 3 km, while those for groundwater samples range from -0.5 to 2.4 km, possibly biased low due to the presence of excess air. Water source altitudes estimated based on $\delta^{18}O$ for most

groundwater samples range from 1.5 to 5.5 km. Source altitudes of the basal aquifer samples are higher than about half of the spring samples, consistent with the notion that basal aquifer is predominantly recharged by high altitude rain events, including synoptic-scale rain, while springs are recharged mostly by orographic precipitation. Tritium/^{3}He ages of basal aquifer samples range from 14 ± 6 years to 47 ± 14 years, while spring samples yield ages ranging from zero to 15 ± 3 years. Older ages of the basal aquifer are consistent with lower sensitivity to seasonal variations in this aquifer compared to perched aquifers. Perched aquifers' young ages likely allow for the observed variations in noble gases and stable isotopes in spring samples between 2014 and 2016.

[1]To be submitted to Water Resources Research.

5.1 Introduction

Previous studies in fractured groundwater systems and rainwater [Warrier et al., 2012; 2013] suggest that noble gas temperatures (NGTs) reflect the temperature of the air at ground level at the time of rainwater infiltration rather than the mean annual air temperature (MAAT). This is in contrast with sedimentary systems, where NGTs are commonly assumed to reflect the MAAT and have been routinely used as paleothermometers [e.g., Stute and Schlosser, 1993; Ballentine and Hall, 1999; Kipfer et al., 2002; Castro and Goblet, 2003; Kulongoski et al., 2004; Sun et al., 2010; Castro et al., 2012; Aeschbach-Hertig and Solomon, 2013]. This indicates that NGTs in fractured areas may record seasonality and information on the location and timing of recharge [Warrier et al., 2012]. This is potentially very useful for fractured volcanic islands, which are typically poorly characterized with respect to groundwater resources and suffer from freshwater scarcity because of their complex internal structures [e.g., Whittier et al., 2010; Kelly and Glenn, 2015; Swarzenski et al., 2017]. The Island of Maui has particularly extreme variations in rainfall both temporally and spatially [e.g., Loope and Giambelluca, 1998], suffering from freshwater shortage in some of the most densely populated areas of the island. Developing a new NGT application that can constrain the location and timing of recharge can potentially lead to a better understanding of these fractured groundwater flow systems in the island. This, in turn, could lead to improved water resource management, which is urgently needed in the State of Hawaii in general and Maui in particular [Gingerich, 1999a; 1999b; 2004; Scholl et al., 2002].

The first comprehensive noble gas study of the hydrological system in the Island of Maui was carried out in June of 2014 [Niu et al., 2017b]. This study included water samples collected from wells tapping the basal aquifer, springs from perched aquifers, as well as rainwater. It was aimed at improving our understanding of the applicability of NGTs in fractured, rapid infiltration systems and more specifically, at assessing connectivity between aquifers in the Island of Maui [Niu et al., 2017b]. This noble gas study revealed that concentrations in all rainwater and groundwater samples were in disequilibrium with the atmosphere at collection conditions and were not representative of the MAAT, findings similar to those reported by Warrier et al. [2012] in the basal aquifer and springs of the fractured, volcanic Galápagos Islands system. Niu et al. [2017b] further showed that noble gas concentrations in rainwater and the basal aquifer are consistent with mixing between ice-like and air-saturated water (ASW) end-members, an

indication that the basal aquifer is likely mostly recharged directly by rainwater. Spring and basal aquifer samples in Maui display distinct noble gas patterns, pointing to distinct recharge sources for the basal and perched aquifers and further suggesting that these two aquifer types are separate entities, as previously suggested by Gingerich [1999a]. Noble gas signatures in spring samples also suggest that perched aquifers are recharged by a diversity of sources [Niu et al., 2017b]. Among these sources, fog is a significant component accounting for ~37% of total precipitation on the windward side of Maui and ~46% on the leeward side [Scholl et al., 2007].

This study is a follow-up of our pilot noble gas study in Maui [Niu et al., 2017b] and aims at further exploring the information noble gases can provide in rapid rainwater infiltration systems. In particular, it assesses whether temporal variations are recorded in noble gas signatures and how NGTs can be applied to these systems to estimate the location and timing of recharge by taking advantage of the temperature and pressure dependency of noble gases in water. Estimating water source altitudes is possible because it was shown that rainwater can retain concentrations acquired in the atmosphere at high altitudes and is still in disequilibrium with the atmosphere at the collection points. This has now been shown in very distinct locations around the world, first in Israel [Mazor, 1972] and more recently in southeast Michigan [Warrier et al., 2013] and Maui [Niu et al., 2017b].

In addition to noble gases, this study is complemented by the analysis of stable isotopes of water (δD and $\delta^{18}O$) in an attempt to further constrain the location and timing of recharge. Studies of stable isotopes of the water have been carried out in oceanic islands across the globe to study the stable isotopic signature of cloud water [Scholl et al., 2002; 2007], rainfall and groundwater circulation in the volcanic structure of Tahiti-Nui [Hildenbrand et al., 2005], orographic precipitation effects on the isotopic composition of precipitations in Sicily [Liotta et al., 2006], subtropical humidity dynamics in the Island of Hawaii [Galewsky et al., 2007], as well as stable isotope amount effect and partitioning of cloud water in montane forests in Puerto Rico [Scholl et al., 2009; 2011]. This study uses δD and $\delta^{18}O$ to help constrain water sources and altitudes of the source water for rainwater and groundwater in Maui, and to explore the potential of the combined use of noble gases and stable isotopes at further constraining the water sources and recharge regime in these systems.

This study is also complemented by estimating water residence times for the basal aquifer and springs using tritium measurements and excess ^{3}He estimates. Preservation of seasonality is

dependent on short groundwater residence times among other factors [e.g., Stute and Schlosser, 1993; Thoma et al., 2011]. Water samples for tritium analysis were collected in our pilot study in June 2014 [cf. Niu et al., 2017b] from the basal aquifer and rainwater. Results show that the contrast in the estimated water ages in the basal aquifer and springs is consistent with the finding that seasonality in noble gases is less apparent in the basal aquifer than in the springs.

5.2 Geologic, Climatologic, and Hydrologic Background

Maui is the second largest island of the Hawaiian Archipelago, located in the Pacific Ocean about 4000 km off the coast of California (Figure 5.1). The island is composed of two volcanoes, mainly basaltic in composition. The volcano in West Maui (altitude 1764 m) is smaller and older than Haleakala (altitude 3055 m), which forms East Maui [Stearns and Macdonald, 1942; West et al., 1987; Bergmanis et al., 2000; Poland et al., 2014]. Ages of the oldest formation of Haleakalā range from 1.10 ± 0.05 to 0.97 ± 0.04 Ma [Chen et al., 1991], and those of the youngest eruptions range from 200 ± 15 to 45,000 ± 1800 years B.P. [Bergmanis et

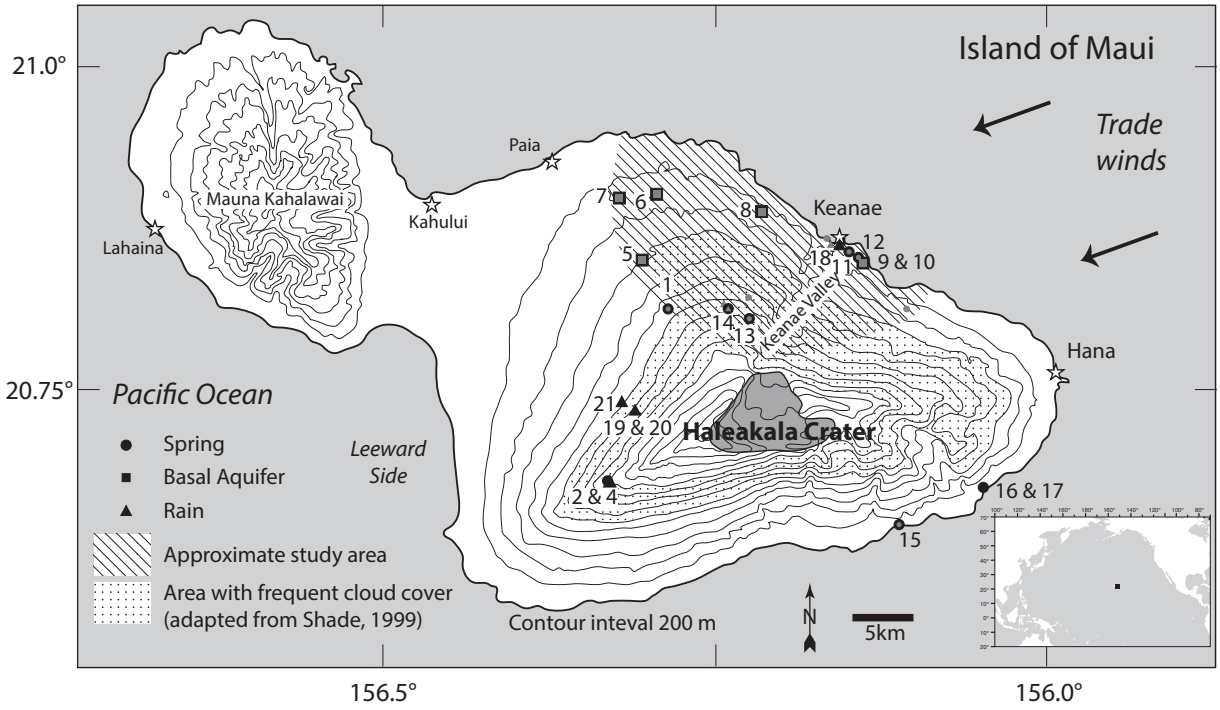

Figure 5.1 Map of the Island of Maui with approximate sampling locations (Modified from Gingerich et al. [1999a] and Scholl et al. [2007]). The square marker in the inset map shows the approximate location of Maui relative to the continents. Black markers in Maui show sampling locations in 2016 and gray markers in 2014.

al., 2000]. The presence of a robust hydrothermal system on Maui was suggested by Fercho et al. [2015], but could not be confirmed.

The Hawaiian Islands lie within the tropical trade wind belt [Sanderson, 1993; Lau and Mink, 2006]. The MAAT in Maui ranges from 24.4°C at Lahaina near sea level (14 m) and 24.2°C at Kahului (14 m) to 10°C at the Haleakala summit (3055 m; Nullet and Sanderson, 1993; http://www.ncdc.noaa.gov/qclcd/QCLCD). On average, annual variation (summer to winter) in air temperatures in Hawaii is about 4 – 5°C [Nullet and Sanderson, 1993].

Climate on the windward side is dominated by trade winds from the east-northeast ~90% of the time in summer and 40–60% of the time in winter months [Blumenstock and Price, 1967; Sanderson, 1993; Garza et al., 2012; Wallsgrove and Penn, 2012]. Trade winds drive the majority of orographic rainfall, which occurs mostly on the windward side of the islands of Northeast Maui [Scholl et al., 2002]. On the windward side, the cloud belt extends from an elevation of 0.6 km to 2.5 km [Giambelluca and Nullet, 1991; Loope and Giambelluca, 1998; Barnes et al., 2016], with the highest rainfall (11 m yr^{-1}) at 1.6 km, ~3 m yr^{-1} at 2.3 km and <1 m yr^{-1} at the summit [Loope and Giambelluca, 1998; Scholl et al., 2002]. Most orographic rain occurs at elevations between 0.9 and 2 km asl, and rainfall above 2 km is mostly from synoptic-scale storms [Schroeder, 1993; Wallsgrove and Penn, 2012]. Fog is a prominent feature on the windward side of Northeast Maui and thought to be most frequent between 1 and 1.9 km asl [Kitayama and Mueller-Dombois, 1994], roughly the elevations where orographic rain occurs the most. Leeward areas receive most of their rainfall from winter cold fronts and low-pressure cyclonic (Kona) storms. In contrast to orographic rain, these storms tend to cover larger areas, but occur less frequently [Wallsgrove and Penn, 2012]. Synoptic-scale rain systems may extend several kilometers up into the atmosphere, with lower temperatures and ice as part of the precipitation process [Chu et al., 1993; Scholl et al., 2007].

The 2015–2016 El Niño was one of the three strongest since 1950, tied with those of 1982–1983 and 1997–1998, based on monthly peak sea surface temperature anomalies [Huang et al., 2016]. According to the monthly precipitation measurements at eight stations in our study area, the 2015–2016 winter season (December 2015, January and February 2016) saw precipitation about 2 to 9 times lower than the corresponding months in 2013 – 2015 [http://www.ncdc.noaa.gov/qclcd/QCLCD].

A radial drainage system is present in Northeast Maui with a dense network of stream

valleys from the Haleakala summit to the ocean [Gingerich, 1999a; 1999b], overlapping with our study area. Streams tend to be perennial at higher altitudes, but some go dry near the coast where they sink into the valley bottom. Streams are fed by springs at higher altitudes, runoff, and base flow, in addition to direct rainfall and fog drip [Gingerich et al., 1999b]. Traditionally, the conceptual model was that most groundwater in the Hawaiian Islands occurs either as perched high-level water held up by relatively low-permeability units, or as dike-impounded aquifers in limited areas, or as freshwater lenses (basal aquifer system) floating on denser, underlying saltwater near sea level [Gingerich, 1999b]. In northeast Maui, west of Keanae Valley (Figure 5.1), rocks beneath the contact between the Kula Volcanics and the underlying Honomanu Basalt and above the freshwater lens are thought to be unsaturated [Gingerich, 1999b; Scholl et al., 2002], with the basal aquifer system recharged through the discontinuous perched high-level water [Gingerich, 1999b]. Although it is still unclear whether the high level aquifers are perched or fully saturated down to sea level, the most recent findings suggest that perched aquifers are not connected to the basal aquifer in Maui [Niu et al., 2017b]. Similar conclusions were reached in the Island of Hawaii, where some high-level confining layers block connections between perched aquifers and the basal aquifer, and form preferential flow paths from near the ground surface directly into the ocean [Thomas et al., 2017].

5.3 Sampling and Analytical Procedures

Thirty-two water samples were collected at 20 sites on the Island of Maui in February 2016 for measurement of He, Ne, Ar, Kr, and Xe concentrations and their respective isotopic ratios (Figure 5.1; Table 5.1). These include six wells tapping the basal aquifer, nine springs at different altitudes, six on the windward side and three on the leeward side, as well as five precipitation events. Samples were collected at altitudes between sea level and 1.9 km asl with collection water temperatures ranging between 11.3 and 21.5°C. Samples for analyses of stable isotopes of water (δD and δ^{18}O) were collected at all sites as well as during rain events both in June 2014 and February 2016 (Table 5.2). Water samples for analysis of tritium concentration were collected in June 2014 for a rain event in Waikamoi as well as all wells except the Kaupakalua well (Table 5.3).

Basal aquifer wells were purged before sample collection to ensure that water within the well casing, which could have equilibrated with the atmosphere, was entirely removed.

Table 5.1 Sampling Location, Sample Type, Measured Water Temperature, Ambient Air Temperature, Noble Gas Concentrations, R/R_a Values, and R/R_{exc} Values. Noble gas concentrations are presented in cm^3 per gram of water at STP. Coordinates with asterisk were measured in situ from handheld GPS unit. Dashes denote missing record.

Sample Type and Number	Location	Latitude (North)	Longitude (West)	Elevation (m)	Water Temperature (°C)	Air Temperature (°C)	He 10^{-8}	Ne 10^{-7}	Ar 10^{-4}	Kr 10^{-8}	Xe 10^{-9}	R/R_a (±1σ)	R_{exc}/R_a (±1σ)
Well / Basal Aquifer													
5	Pookela	20˚50'55"	156˚18'20"	581	18.7	20	4.59	1.88	2.88	6.19	8.22	1.02 (0.01)	
6a	Kaupakalua	20°54'8"	156°17'13"	1233	20.1	22.1	4.46	1.77	2.60	5.73	7.10	1.00 (0.01)	
6b							4.66	1.86	2.79	6.05	7.96	1.03 (0.02)	
7a	Haiku	20°53'59"	156°19'29"	247	19.9	21.7	4.28	1.71	2.54	5.66	7.03	1.01 (0.02)	
7b							4.51	1.80	2.69	5.71	7.64	1.04 (0.01)	
8a	Ohanui	20°53'23"	156°13'0"	254	20.6	22.1	4.29	1.69	2.44	5.26	6.40	1.03 (0.02)	
8b							4.50	1.79	2.71	5.84	7.89	1.03 (0.01)	
9a	Keanae 1	20°50'53"	156°8'7"	65	19.1	24.7	5.60	1.95	2.96	6.65	8.41	2.08 (0.04)	8.3 (0.9)
9b							5.58	1.90	2.88	6.29	8.71	2.09 (0.03)	7.3 (0.7)
10a	Keanae 2	20°50'53"	156°8'7"	65	18.3	24.7	5.15	1.77	2.61	5.59	7.81	2.19 (0.03)	10.1 (1.2)
10b							5.64	1.95	2.89	6.18	8.31	2.09 (0.02)	7.7 (0.7)
Spring													
1	Waihou	20°48'21"	156°17'12"	1038	15.7	15.6	3.95	1.54	2.28	5.06	6.36	1.03 (0.01)	
2a	Polipoli	20.68° *	156.33° *	1906	11.3	12.3	3.34	1.44	2.36	5.13	7.00	1.01 (0.02)	
2b							3.74	1.56	2.59	5.76	8.23	1.03 (0.01)	
11a	Keanae	20°51'30"	156°8'53"	6	21.2	29.5	4.46	1.80	2.74	6.04	7.55	0.92 (0.01)	
11b							4.54	1.84	2.88	6.33	8.72	0.99 (0.01)	
12a	Ohia	20°51'3"	156° 8'32"	63	18.7	25.8	4.51	1.76	2.69	5.77	8.07	1.17 (0.02)	17 (23)
12b							4.66	1.87	2.97	6.55	9.00	1.17 (0.02)	6.2 (2.8)
13	Honomanu	20°48'12"	156°13'17"	1286	19.6	24.9	4.51	1.88	2.86	6.08	8.18	0.99 (0.02)	
14	Waikamoi	20°48'31"	156°13'48"	1286	12.6	17.2	3.29	1.44	2.33	4.98	6.70	1.02 (0.02)	
15a	Mokulau	20.64° *	156.11° *	0	19.5	27.2	4.87	1.79	2.57	5.53	6.74	1.47 (0.03)	7.2 (1.4)
15b							4.88	1.82	2.57	5.28	6.70	1.35 (0.02)	5.5 (1.1)
16a	Near Pepeiaolepo Bay	20.67° *	156.04° *	91	21.5	25	4.36	1.75	2.59	5.53	7.65	0.98 (0.01)	
16b							4.56	1.80	2.64	5.64	7.47	1.00 (0.01)	
17a		20.67° *	156.04° *	96	19.9	25	4.27	1.69	2.42	5.00	6.63	1.02 (0.02)	
17b							4.43	1.80	2.76	6.03	8.09	1.00 (0.01)	
Rain													
4	Polipoli spring	20.68° *	156.33° *	1906	-	10.2	3.23	1.34	2.08	4.41	5.90	0.99 (0.02)	
18a	Near Keanae	-	-	100	-	21.5	4.33	1.69	2.29	4.46	5.41	1.02 (0.02)	
18b							4.51	1.75	2.52	5.22	6.81	1.04 (0.02)	
19	Near Kula Botanical Gardens	20.73° *	156.31° *	1415	-	15.4	3.74	1.48	2.20	4.58	6.08	1.03 (0.01)	
20		20.73° *	156.31° *	1415	15.8	15.9	3.80	1.57	2.58	5.70	8.06	1.03 (0.02)	
21		20.74° *	156.32° *	1102	16.9	15.8	3.37	1.36	1.97	4.05	5.26	0.96 (0.02)	

Groundwater samples were collected in ~14 cm^3 standard refrigeration grade 3/8" copper tubing and cold-sealed using steel pinch-off clamps [Weiss, 1968] after water was allowed to flow through the system for ~10 min. Rainwater was collected on a tarpaulin and transferred to a 0.5 L plastic bottle before being transferred to copper tubing in the field. The transfer of rainwater from the tarpaulin to the copper tubing took up to 20 min, except for sample #20, which took ~40 min. During this time, we expect that at least partial equilibration of noble gases at surface collection conditions occurred, and sample #20 is expected to achieve a higher degree of partial equilibration because of its longer collection time.

Noble gas analyses were carried out in the Noble Gas Laboratory at the University of Michigan. Analysis procedures are described briefly here. After extraction and purification, He and Ne are sequentially allowed to enter a Thermo Scientific® Helix SFT mass spectrometer while Ar, Kr and Xe are sequentially allowed into an ARGUS VI mass spectrometer using a computer-controlled double-head cryo-separator. He and Ne are pumped at ~10K into the low temperature chamber of the cryo-separator while Ar, Kr, and Xe are pumped at 104K into the high temperature chamber. The temperatures of both chambers are subsequently increased sequentially to release He, Ne, Ar, Kr, and Xe at temperatures of 49K, 84K, 210K, 245K, and 290K, respectively. Complete measurement procedures involve estimating the concentration of each noble gas component as well as measuring isotopic ratios. Standard errors for concentrations are 1.5%, 1.3%, 1.3%, 1.5%, and 2.2%, respectively. Additional sampling, extraction, and purification procedures can be found in Wen et al. [2016].

During both sampling seasons (June 2014 and February 2016) water samples for δD and $\delta^{18}O$ analyses were collected in 20-mL glass bottles with polyethylene seal caps and analyzed at the University of Michigan. Samples collected in 2014 were analyzed in the Stable Isotope Laboratory. Oxygen isotopic composition was analyzed using a Finnigan Gas Bench II coupled to the inlet of a Finnigan Delta V Plus mass spectrometer using continuous flow applications. Standard errors are ~0.12‰ based on VSMOW/VSLAP calibration [Nelson, 2000a; 2000b]. Hydrogen isotopic composition was determined via a Fignnigan H-Device coupled to a Finnigan Delta V Plus mass spectrometer with dual inlet. Standard errors are ~1.2‰, based on USGS standards 45, 46, 47, and 48, and VSMOW/VSLAP calibration [Nelson and Dettman, 2001]. Samples collected in 2016 were analyzed in the Climate Change Laboratory in a Picarro L2120-i Cavity Ringdown Spectrometer with an integrated A0211 high precision vaporizer and

autosampler. Standard errors are ~0.1‰ for $\delta^{18}O$ and ~0.4‰ for δD. Details on the analysis procedure can be found in Fiorella et al. [2015].

Samples for tritium analyses were collected in ~40 cm^3 standard refrigeration grade 3/8" copper tubing and cold-sealed using steel pinch-off clamps [Weiss, 1968], same as that for noble gas analyses. Analyses of tritium concentration were carried out at the Bremen Mass Spectrometric Facility following procedures in Sültenfuß et al. [2009].

5.4 Results and Discussion

5.4.1 Noble gas concentrations and isotopic ratios

Noble gas concentrations normalized to ASW values at collection altitude and water temperature for samples from basal and perched aquifers and air temperature for rainwater samples are displayed in Figure 5.2 for both sampling seasons, i.e., June 2014 [Niu et al., 2017b] and February 2016 (this study). It is apparent that most samples collected in both years display a mass-dependent depletion pattern, with concentrations of the heavier noble gases (Ar, Kr, and Xe) being less enriched or more severely depleted than those of the lighter noble gases (He and Ne) with respect to ASW values. Some patterns are, however, distinct for 2014 and 2016. While

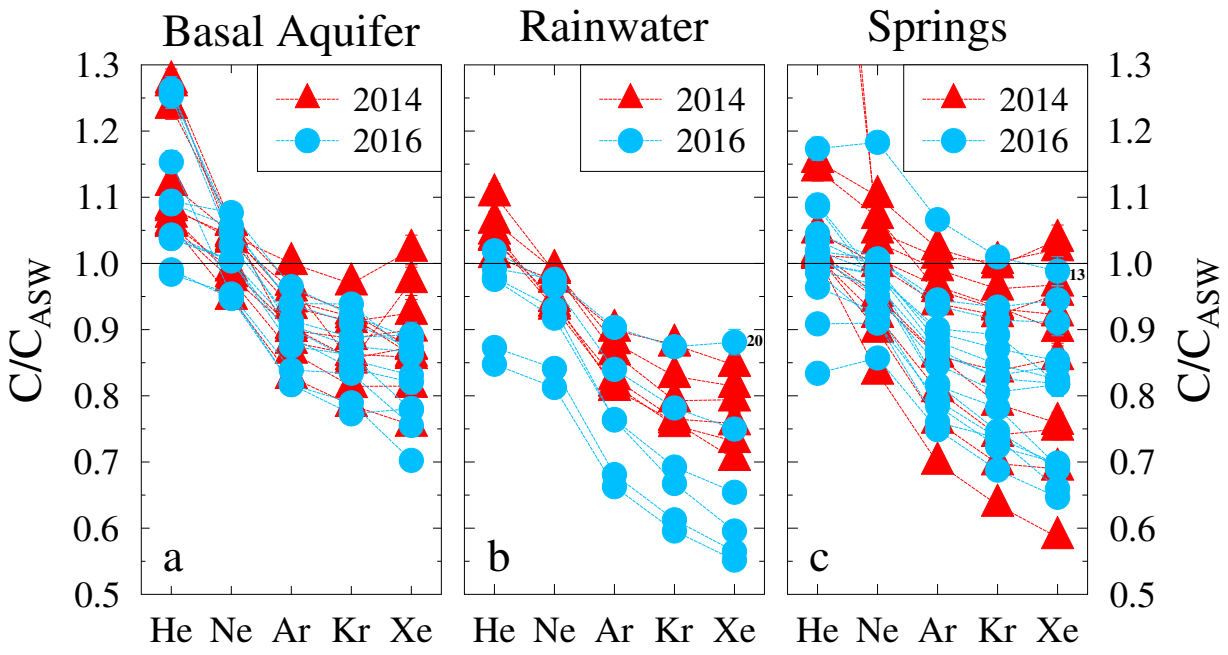

Figure 5.2 Total measured noble gas concentrations normalized to ASW at collection temperatures (ambient air temperature for rainwater samples and water temperature for basal aquifer and spring samples) and altitudes in both years for (a) basal aquifer, (b) springs, and (c) rainwater samples. The solid black line indicates noble gas concentrations with no addition or loss of noble gases compared to ASW.

basal aquifer samples display overall similar noble gas signatures in both years with He excesses up to 27% and Xe depletions up to 30% (Figure 5.2a), the same does not hold true for spring and rainwater samples. The most striking differences are found in rainwater with most 2016 samples being significantly more depleted than 2014 samples for all gases. In addition, while all of the 2014 rainwater samples display ASW He concentrations or He excesses, some of the 2016 samples display He depletions up to 15%, a signature not observed in 2014 (Figure 5.2b). The same holds true for spring samples (Figure 5.2c). Although it seems that the 2016 rainwater sample with highest Xe concentration (sample 20; Figure 5.2b) exhibits noble gas concentrations comparable to those in 2014, this sample took about twice the normal collection time to be collected. Therefore, it is expected that this sample has achieved a higher level of partial equilibration with the atmosphere than most other rainwater samples. With the exception of sample 20, it is apparent that rainwater noble gas concentrations in 2016 are overall significantly lower than those of 2014, indicating that noble gases in rainwater indeed record temporal variations caused by ambient temperature and pressure conditions.

Before discussing the measured He concentrations in all types of samples, it is useful to discuss the contributions of non-atmospheric components to the observed He excesses. The origin of the He excesses is constrained through measured R/R_a and estimated R_{exc}/R_a values (Table 5.1), where R is the measured $^3He/^4He$ ratio in the samples, R_a is the atmospheric ratio (1.384×10^{-6}; Clarke et al., 1976) and R_{exc} is the ratio from which the ASW and excess air (EA) components are excluded (cf., Appendix C1). The EA component results from air bubbles incorporated in groundwater due to rapid fluctuations of the water table [Heaton and Vogel, 1981]. R_{exc}/R_a provides the isotopic ratio of He excess that results either from crustal production or from the mantle as discussed in Text S1. Measured R/R_a values for all spring and basal aquifer samples vary between 0.92 ± 0.01 (Keanae Spring, sample 11a) and 2.19 ± 0.11 (Keanae Well 2, sample 10a), while R/R_a values for rainwater samples vary from 0.96 ± 0.02 to 1.04 ± 0.02, close to the atmospheric value ($R/R_a = 1$) within a 2σ error. All basal aquifer samples from sites 9, 10, 12, and 15 yield R/R_a values higher than the atmospheric ratio ($R/R_a > 1$), which are undistinguishable from corresponding values measured in 2014. These correspond to mantle He excesses which contribute between 13% and 18% of the total He concentrations measured in in both Keanae wells (sites 9 and 10), and ~1% – 8% of those from sites 12 and 15. Sample 11a yields an R/R_a value of 0.923 ± 0.014, lower than 1, and is expected to have a crustal He

component (average crustal values for R/R_a vary between 0.02 and 0.05; O'Nions and Oxburgh, 1983). However, it was not possible to estimate the R_{exc}/R_a value following the method discussed in Appendix C1, due to a negative estimated concentration of non-atmospheric He. Assuming a binary mixing between crustal and atmospheric He components and an R/R_a of 0.02 for the crustal end-member, it is estimated that crustal He contributes to ~8% of the total He concentration. The He component separation and origin of R_{exc}/R_a values are discussed in detail in Appendix C1.

He excesses and severe depletion in heavy noble gases in rainwater samples from 2014 were hypothesized to result from an ice-like signature and thus associated to synoptic-scale events. However, most rainwater samples collected in 2016 and thus, during the strong 2015–2016 El Niño period, present He depletions, a feature inconsistent with an ice-like signature. This is further discussed below. Ne concentrations in rainwater samples are 2% to 19% lower than ASW values, while Ar, Kr, and Xe in rainwater samples display more severe depletions, 10% to 34%, 13% to 40%, and 12% to 45% lower than the ASW values, respectively. In contrast, Ne concentrations in basal aquifer and spring samples from 2016 do not show a consistent pattern when compared with ASW. Five basal aquifer samples from 2016 display Ne excesses up to 18%, three basal aquifer samples and ten spring samples display Ne depletion up to 14%, and three basal aquifer samples and four spring samples display ASW Ne concentrations within 1σ errors. Ne excess in groundwater is generally linked to the presence of an EA component. Similar to rainwater samples, all basal aquifer samples and most spring samples from 2016 exhibit Ar, Kr, and Xe concentrations lower than ASW values, with depletion values ranging between 4% – 25%, 6% – 28%, and 5% – 35%, respectively. One spring (Figure 5.2b) from 2016 displays an Ar excess of 7% and Kr and Xe concentrations equal to ASW values. It is possible that this sample has a significant amount of excess air, which might explain its higher normalized Ne, Ar, Kr, and Xe concentrations compared to all other spring samples.

Figure 5.3 compares measured noble gas concentrations in 2016 with those from the same sites in 2014 for samples collected at the same sites on both sampling campaigns from the basal and perched aquifers. Because samples from well #10 were not collected in 2014, these are compared with those from well #9 in 2014 due to spatial proximity. Leeward springs #16 and #17 collected in 2016 only are compared with the only sample collected on the leeward side in 2014, spring #15. Overall, most basal aquifer samples lie close to the 1:1 line pointing to similar

concentrations in both years, consistent with findings displayed in Figure 5.2a, in which all samples are compared with their respective ASW noble gas concentrations. This suggests that, unlike rainwater, the basal aquifer does not preserve a record of seasonality in absolute noble gas concentrations, nor in level of equilibration with the atmosphere (concentrations normalized to ASW). These results are also consistent with ages calculated based on tritium concentrations

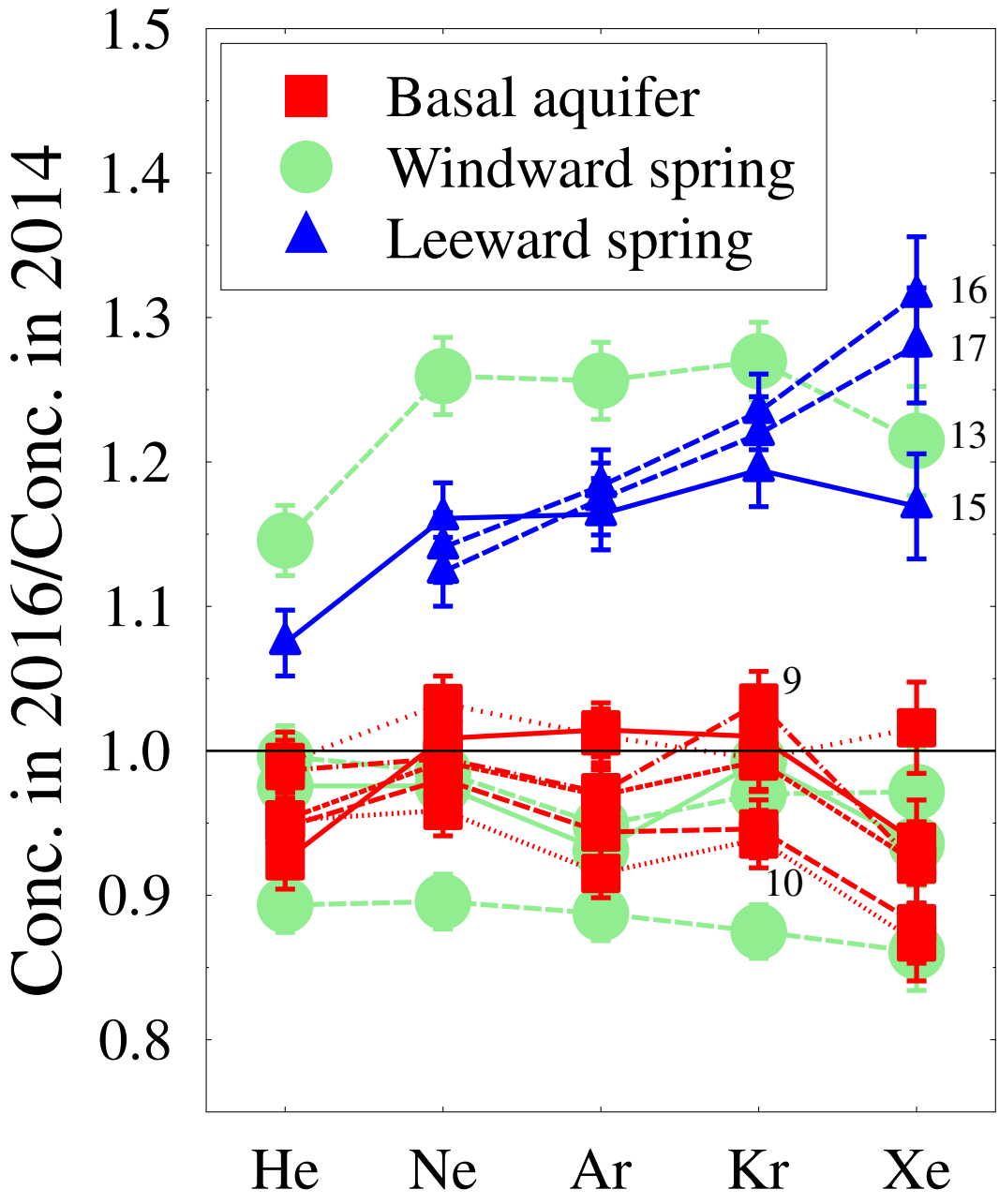

Figure 5.3 Total measured noble gas concentrations in 2016 normalized to samples from the same site or the closest site in 2014. The solid black line indicates noble gas concentrations being the same in both sampling seasons.

measured in the basal aquifer, discussed below. In contrast, spring samples display significantly higher variations in measured concentrations than the basal aquifer, the highest variation being ~30%. In particular, all of the leeward springs in 2016 display Ne, Ar, Kr, and Xe concentrations in excess relative to 2014, with excesses ranging between 10% and 30%. Sample #15 also displays He concentrations in excess relative to 2014. He concentrations of samples #16 and #17 are not compared to that of sample #15. This is because sample #15 (Mokulau spring) has terrigenic He contributions (up to 10% of total He; Niu et al., 2017b) while samples #16 and #17 lack these extra He sources. All three leeward springs display similar noble gas concentrations, indicating that they are likely recharged by more homogenized sources, with little variation between different sites on the leeward side. Most (three) windward springs display the opposite behavior of leeward springs, with 2016 noble gas concentrations being depleted with respect to 2014 while spring #13 displays normalized Ne, Ar, and Kr concentrations above all leeward springs. Windward springs display greater concentration variations among all samples, with highest and lowest normalized values with respect to 2014, an indication that windward springs are recharged by more diverse water sources than the leeward side of the island. These findings reinforce those presented by Niu et al. [2017b]. It is interesting to note that the only windward spring (site 13) that has higher noble gas concentrations in 2016 is the one with highest concentrations when normalized to ASW (Figure 5.2). These high concentrations might result from the presence of EA when air bubbles are incorporated due to significant water level variations during intense recharge periods. This reinforces the conclusion that local hydrology and recharge water sources are more diverse for windward springs than those for leeward springs.

In addition to concentrations, noble gas isotopic ratios can point to the occurrence of microscopic processes and help constrain noble gas sources. For example, Ar isotopic ratios of samples collected in 2016 show that noble gases were in the process of diffusing into raindrops at the time of collection. Figure 5.4 displays measured $^{40}Ar/^{36}Ar$ ratios versus $^{38}Ar/^{36}Ar$ ratios for these samples together with the expected mass-dependent fractionation line under disequilibrium conditions. It is apparent that all samples fall along an array close to the mass-dependent fractionation line, with both $^{40}Ar/^{36}Ar$ and $^{38}Ar/^{36}Ar$ ratios lower than the corresponding atmospheric values for most samples. This shows that the lighter isotopes are enriched in comparison to heavier ones, and that all samples are in disequilibrium with the atmosphere at the

collection point, as also observed with noble gas concentrations (Figure 5.2). Overall, rainwater samples exhibit Ar isotopic ratios similar to those displayed by basal aquifer and spring samples with one rainwater sample displaying the lowest Ar isotopic ratios (farthest away from atmospheric values) indicating the greatest depletion of the heavy isotopes and thus, the greatest disequilibrium compared to ASW. It is also interesting to point out that rainwater sample #20, which required by far the longest time to be collected and thus, the rainwater sample with the longest time available to equilibrate with the atmosphere, is also the one displaying the highest Ar isotopic ratios, i.e., the values the closest to atmospheric values indicating that time availability to equilibrate with the atmosphere will determine both isotopic ratios and concentrations of all samples. With the exception of this sample, it is apparent that rainwater samples represent the lower end in Ar isotopic ratio values in the array shown in Figure 5.4. As time goes by, the rainwater achieves a higher degree of partial equilibration. Similarly, the basal

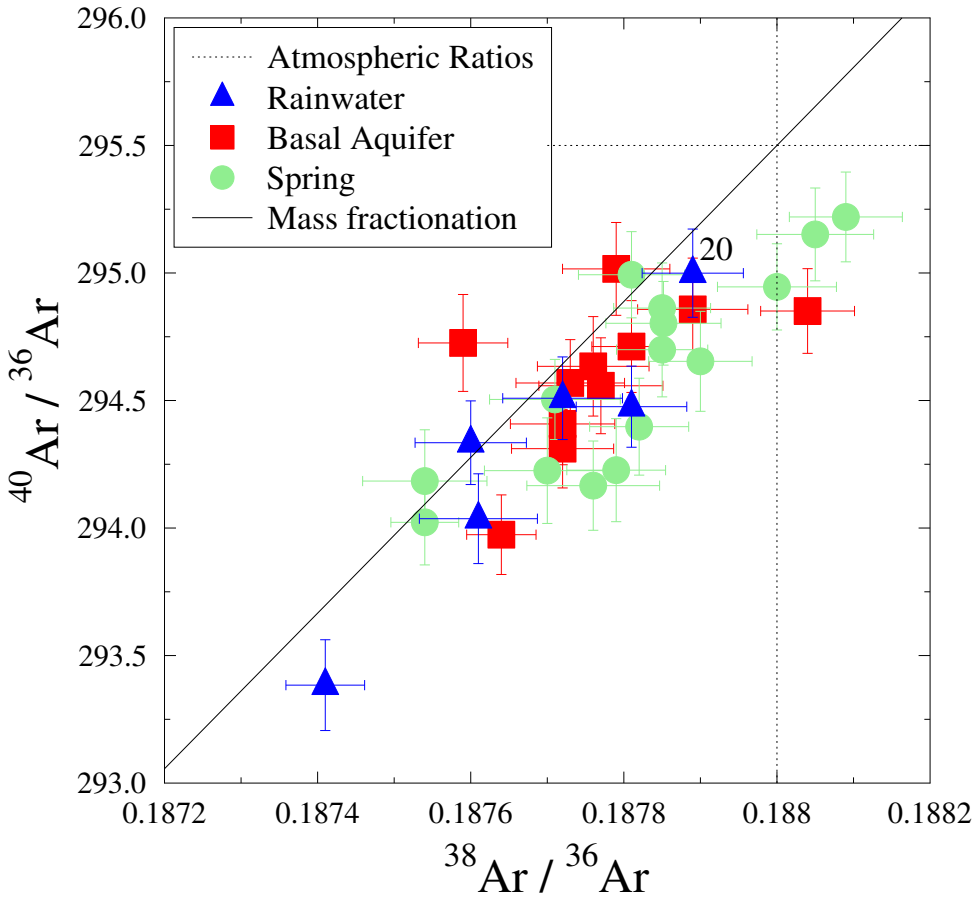

Figure 5.4 Measured $^{40}Ar/^{36}Ar$ ratios plotted against $^{38}Ar/^{36}Ar$ ratios for all samples in 2016, compared with the mass-dependent fractionation line.

aquifer and spring samples display Ar isotopic ratios closer to the atmospheric values than rainwater, which represents one of the water sources.

As most samples yield Ar isotopic ratios close to the mass-dependent fractionation line, measured $^{38}Ar/^{36}Ar$ and $^{40}Ar/^{36}Ar$ ratios may be used as a measure of the degree of partial equilibration. In Figs. 5a and 5b, measured $^{38}Ar/^{36}Ar$ and $^{40}Ar/^{36}Ar$ ratios, respectively, are plotted against their Ar concentrations normalized to expected ASW values (cf. Figure 5.2).

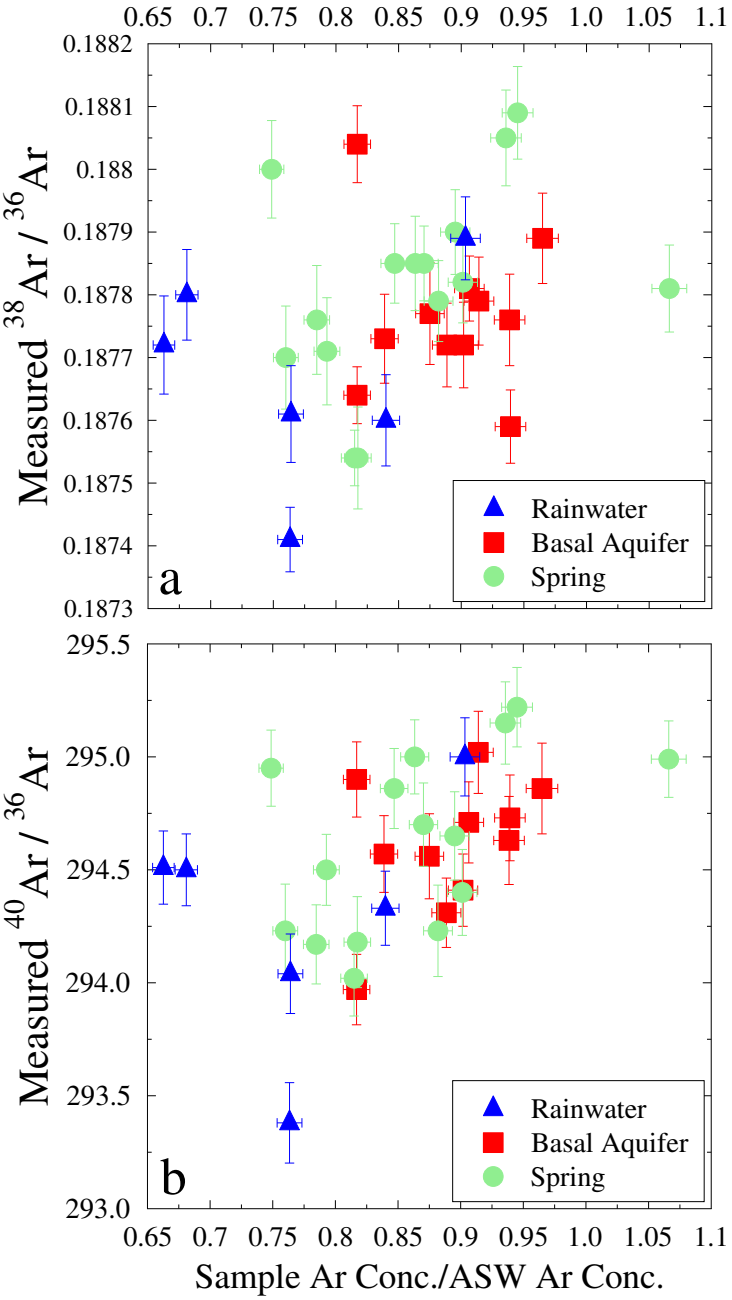

Figure 5.5 Measured Ar isotopic ratios versus Ar concentration normalized to ASW: (a) $^{38}Ar/^{36}Ar$, (b) $^{40}Ar/^{36}Ar$.

Overall, higher Ar concentrations correlate to higher measured $^{38}Ar/^{36}Ar$ and $^{40}Ar/^{36}Ar$ ratios, although the points are rather scattered. If a best-fitting line were to be drawn for all samples in either plot, the R^2 would be ~0.1 for Figure 5.5a and ~0.25 for Figure 5.5b. These low R^2 values indicate that although a correlation between Ar concentration and isotopic ratios might be possible, the relation is not linear. Further investigation is needed to fully understand noble gas behaviors in diffusion processes in both rain droplets and in groundwater reservoirs.

In summary, basal aquifer samples yield similar noble gas patterns in both sampling campaigns, while rainwater and spring samples display seasonal variations in noble gases, which may also be a reflection of the strong El Niño year during the 2016 sampling campaign. Leeward springs yield higher noble gas concentrations in 2016 while most windward springs yield lower concentrations. He depletion was observed in a subset of rainwater and spring samples collected during the 2015–2016 El Niño. To our knowledge, this is the first time that He depletion is observed in rainwater. Ar isotopic ratios of all samples seem to be consistent with a diffusion process where Ar diffuses from air into rain droplets and groundwater reservoirs. Ar isotopic ratios possibly correlate with total Ar concentration, but the relation is not yet clear.

5.4.2 Stable isotopes

Figure 5.6 displays measured δD versus $\delta^{18}O$ for all samples collected in both 2014 and 2016 (Table 5.2), compared with five Maui fog samples collected between 1.2 and 2 km asl [Scholl et al., 2002; 2007]. It is relevant to point out that the collection time for each fog sample by Scholl et al. [2002; 2007] was at least a week. Also represented is the global meteoric water line (GMWL; Craig, 1961). All samples from both sampling campaigns have higher deuterium excesses when compared to the GMWL, ranging from 13‰ to 29‰, where deuterium excess, denoted by *d*, is defined as:

$$d = \delta D - 8 * \delta^{18}O$$

[Dansgaard, 1964]. Overall, the 2016 samples have greater deuterium excesses (17‰ to 29‰) than those of 2014 (13‰ to 20‰). Deuterium excess averages about 10‰ on a global basis, but varies regionally due to variations in humidity during kinetic evaporation from the ocean surface [Clark & Fritz, 1997]. Deuterium excess increases as humidity decreases [Merlivat and Jouzel, 1979]. The observed higher deuterium excess values in 2016 are consistent with the drier El Niño climate of 2016 [Huang et al., 2016; http://www.ncdc.noaa.gov/qclcd/QCLCD, 2017].

Table 5.2 Measure $\delta^{18}O$ and δD and calculated deuterium excess and their associated errors for all samples from both years. Site numbers with the number 14 hyphenated after them refer to sites numbers in 2014 [Niu et al., 2017b]. Stable isotope samples collected at rain events #4 in 2016 were lost during transportation.

Sample Type and Number	June 2014			February 2016		
	$\delta^{18}O$ (±1σ)	δD (±1σ)	*d* (δD-8* $\delta^{18}O$) (±1σ)	$\delta^{18}O$ (±1σ)	δD (±1σ)	*d* (δD-8* $\delta^{18}O$) (±1σ)
Well						
5	-5.38 (0.05)	-29.68 (0.77)	13.36 (0.78)	-5.64 (0.07)	-24.44 (0.43)	20.68 (0.47)
6	-3.70 (0.05)	-11.69 (1.1)	17.91 (1.1)	-3.80 (0.05)	-8.53 (0.41)	21.87 (0.43)
7	-4.01 (0.04)	-16.66 (0.74)	15.42 (0.75)	-4.41 (0.06)	-14.09 (0.13)	21.19 (0.21)
8	-3.40 (0.05)	-8.26 (0.33)	18.94 (0.36)	-3.45 (0.05)	-5.01 (0.15)	22.59 (0.21)
9	-4.56 (0.04)	-19.75 (0.9)	16.73 (0.91)	-4.77 (0.03)	-16.11 (0.33)	22.05 (0.34)
10	-	-		-5.04 (0.06)	-17.88 (0.13)	22.44 (0.21)
Spring						
1	-4.96 (0.07)	-24.22 (0.16)	15.46 (0.25)	-5.17 (0.06)	-22.33 (0.50)	19.03 (0.53)
2	-	-		-6.96 (0.08)	-34.49 (0.53)	21.19 (0.58)
11	-2.99 (0.04)	-6.33 (0.39)	17.59 (0.41)	-3.04 (0.04)	-6.85 (0.30)	17.47 (0.32)
12	-4.21 (0.04)	-15.73 (0.36)	17.95 (0.38)	-4.28 (0.04)	-13.95 (0.25)	20.29 (0.27)
13	-3.35 (0.05)	-6.61 (0.74)	20.19 (0.75)	-3.17 (0.05)	-5.19 (0.21)	20.17 (0.25)
14	-	-		-3.69 (0.05)	-7.48 (0.21)	22.04 (0.25)
15	-4.28 (0.07)	-17.66 (0.64)	16.58 (0.67)	-3.99 (0.05)	-14.31 (0.25)	17.61 (0.29)
16	-	-		-2.89 (0.10)	-4.74 (0.28)	18.38 (0.40)
17	-	-		-2.74 (0.05)	-3.64 (0.16)	18.28 (0.21)
8-14	-3.20 (0.08)	-6.83 (0.53)	18.77 (0.58)	-	-	
10-14	-4.99 (0.05)	-20.35 (0.31)	19.57 (0.34)	-	-	
14-14	-3.45 (0.06)	-7.55 (0.23)	20.05 (0.29)	-	-	
Rain						
18	-	-		-0.2 (0.06)	15.28 (0.23)	16.88 (0.29)
19	-	-		-3.26 (0.10)	0.89 (0.70)	26.97 (0.75)
20	-	-		-3.44 (0.09)	1.03 (0.52)	28.55 (0.58)
21	-	-		-3.6 (0.06)	-1.02 (0.87)	27.78 (0.89)
11-14	-2.54 (0.06)	-3.53 (0.21)	16.79 (0.27)	-	-	
13-14	-3.29 (0.05)	-6.82 (0.29)	19.50 (0.32)	-	-	
15-14	-1.41 (0.06)	5.86 (0.31)	17.14 (0.35)	-	-	

Three 2016 rainwater samples are outliers and display significantly higher deuterium excesses (27‰ – 29‰) compared to all other samples. Overall, the fog samples are similar to the two rainwater samples collected in 2014 at altitudes of ~1.2 km asl, and are more enriched in heavy isotopes than most groundwater samples. The best fitting line (red dashed line, Figure 5.6) for all samples except the three rainwater outlier samples has a slope of 7.64, very close to that of the GMWL. In general, rainwater samples from both years are isotopically the heaviest, with one rainwater sample from each year being heavier than all of the basal aquifer and spring samples.

These rainwater samples are representative of the heavy end-member of sources contributing to both basal and perched aquifers. These two rainwater samples (#18 and #15-14) were collected near sea level (0 – 0.1 km asl) and it is expected that their $\delta^{18}O$ values are higher than the other rainwater samples, which were collected 1.1 – 1.4 km asl. Indeed, δD and $\delta^{18}O$ values in precipitation decrease with decreasing MAAT and increasing altitude. The depletion of ^{18}O

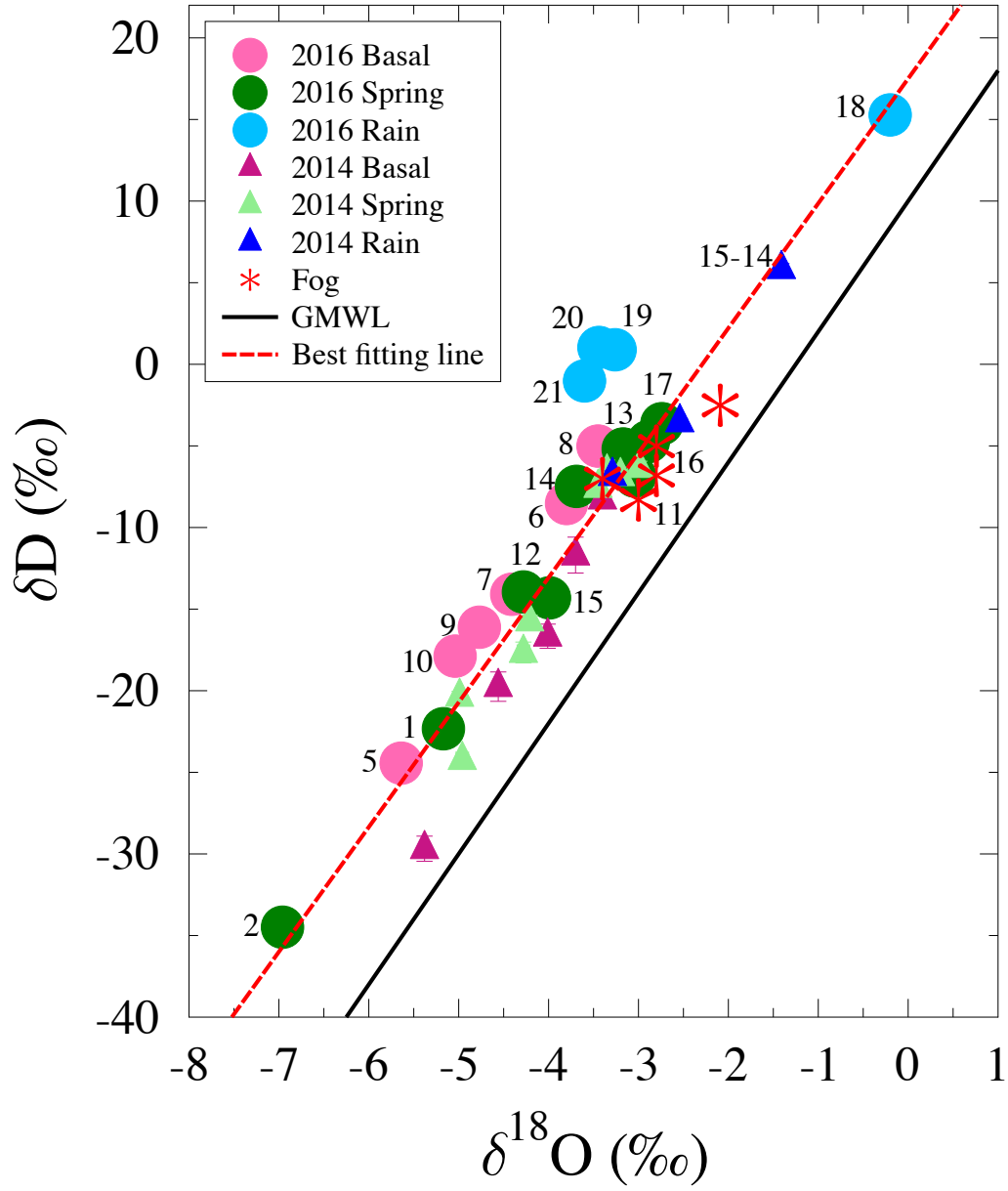

Figure 5.6 Measured δD plotted against $\delta^{18}O$ for all samples in both years, compared with the global meteoric water line (GMWL) and fog samples in Maui [Scholl et al., 2002; 2007]. A best fitting line ($\delta D = 7.64 * \delta^{18}O + 17.50$, $R^2 = 0.95$) for all samples except three rainwater samples farthest away from the GMWL is shown.

varies between -1‰ and -5‰ per km rise in altitude, and this gradient depends on local topography, proximity to surface water sources, etc. [Clark and Fritz, 1997]. Overall, the basal aquifer samples yield similar δD and $\delta^{18}O$ values as the spring samples in both years. The spring sample from the highest collection altitude (~1.9 km; site #2) is the lightest, as expected, with a δD value of -34.49‰ and a $\delta^{18}O$ value of -6.96‰. All of the basal aquifer samples from 2014 yield lower δD values than corresponding samples collected from the same well in 2016. The differences in δD in basal aquifer samples vary between 2.6‰ and 5.2‰. Only one spring sample (#15, Mokulau spring) displays an increase in δD within this range (3.4‰ higher in 2016 than in 2014), while three other springs display smaller increases, ranging between 1.4 and 1.9‰. Different from all other groundwater samples, spring #11 has a δD value 0.5‰ lower in 2016 than in 2014.

In summary, δD values increased from the collection season in 2014 to that in 2016 in all basal sample sites and four out of the five springs. On the other hand, all basal samples have $\delta^{18}O$ values lower than or approximately equal to those from the same sites in 2014, the values in 2016 being 0.05‰ – 0.4‰ lower than those in 2014. Spring samples do not show a consistent pattern in changes in $\delta^{18}O$ values between two collection seasons, with decrease of up to 0.2‰ or increase of up to 0.3‰ from 2014, consistent with the notion that springs are mainly recharged by localized and diverse sources. Overall, samples from wells tapping the basal aquifer yield lower $\delta^{18}O$ and higher δD values in 2016, while samples from springs do not display a specific trend. This suggests that the drier climate in Maui during the 2015–2016 El Niño may have affected water stable isotopic composition and the dissolved noble gas concentrations in different ways.

Figure 5.7 displays calculated deuterium-excess plotted against measured $\delta^{18}O$ for all samples collected in both years (triangles corresponding to 2014, circles to 2016). It is apparent that three rainwater samples in 2016 yield *d* values (27‰ – 29‰) significantly higher than all other samples (13‰ – 23‰). This may be due to the drier environment in February 2016 caused by the strong 2015–2016 El Niño [Liotta et al., 2006; Huang et al., 2016]. Indeed, Liotta et al. [2006] suggested that water droplets in orographic clouds may not have enough time to equilibrate with surrounding vapor and since orographic rain represents the first condensation of marine water vapor, it is expected to have a high deuterium excess. This likely accounts for the different *d* values observed in the two rainwater samples in 2014 and three rainwater samples in

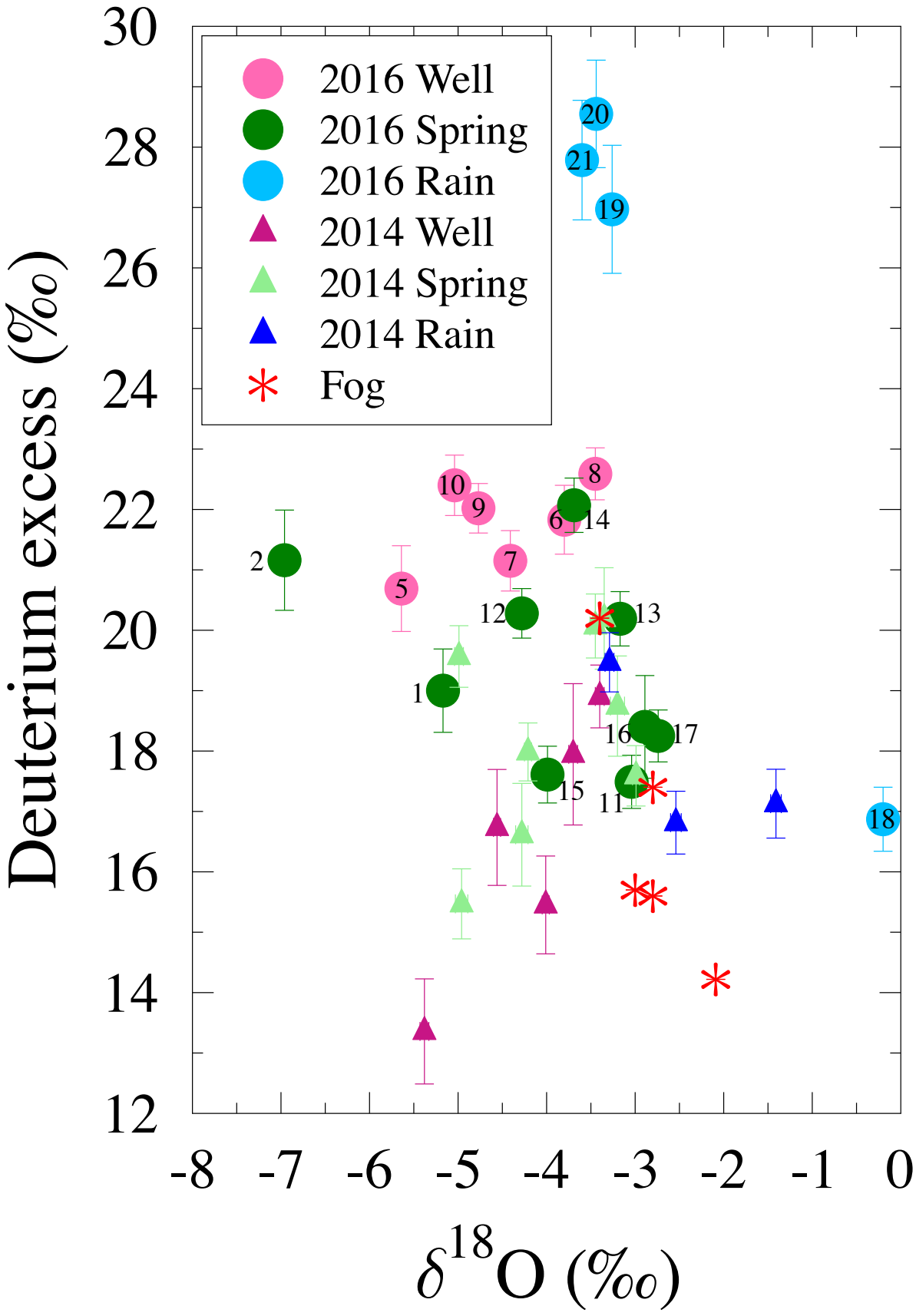

Figure 5.7 Calculated deuterium excess plotted against measured $\delta^{18}O$ for all samples in both years, compared with fog samples in Maui [Scholl et al., 2002; 2007].

2016, all of which were collected at altitudes between 1.1 and 1.4 km. The 2014 rainwater samples displayed an ice-like noble gas signature [Niu et al., 2017b], which would suggest rain originating at altitudes higher than orographic rain. In contrast, the 2016 rainwater samples do not exhibit an ice-like noble gas concentration pattern due to He depletion and might be representative of orographic rain. This is consistent with the stable isotope pattern exhibited by three 2016 rainwater samples that suggest an orographic rain signature. A combined dataset of noble gas and water stable isotopes appears to have the potential to aid in further constraining original water sources to groundwater reservoirs.

Overall, the 2016 basal aquifer samples display deuterium excesses ranging between 20.7‰ and 22.6‰, while most spring samples and 2014 basal samples yield deuterium excesses significantly lower, with values ranging between 15.5‰ and 20.3‰, with only one 2016 spring (#14) yielding $\delta^{18}O$ (-3.69‰) and *d* (22.1‰) values similar to those of 2016 basal samples. It is possible that the three rainwater samples with the highest deuterium excesses are representative of the orographic rain end-member of the water sources of the basal aquifer. The addition of rainwater with high *d* values causes the increase in basal aquifer's *d* values and points to a dominant, direct precipitation source as previously suggested by Niu et al. [2017b]. Five fog samples display *d* values between 14 and 20 [Scholl et al., 2002; 2007], close to the lower half of the *d* value spectrum of our Maui samples. Most of the groundwater samples from Maui display *d* values consistent with mixing between fog and rainwater with high *d* values. It should be noted that collection time for fog samples was at least a week [Scholl et al., 2002; 2007], likely allowing for some level of equilibration with the atmosphere under different climatic conditions over this time period.

In summary, the samples collected in 2016 yield overall higher deuterium excesses than those collected in 2014, all of which displaying higher deuterium excesses than the GMWL. Three 2016 rainwater samples are outliers and display the highest deuterium excesses of all the samples, and this may be due to the lack of equilibrium with surrounding vapor when water droplets form in orographic clouds.

5.4.3 Estimation of water source altitudes

As discussed above, both atmospheric noble gas concentrations and stable isotopic compositions are affected by the source altitude of the precipitation sources. In this section, we explore how to use both datasets to derive information on water source altitudes.

5.4.3.1 Water source altitudes based on Ne concentration

Although concentrations of all noble gases dissolved in water are affected by ambient pressure and temperature, He and Ne concentrations are minimally temperature-dependent [Mazor, 1972; Benson and Krause, 1976]. When clouds form and precipitation occurs, the lapse rate in the clouds and the surrounding atmosphere will be affected by condensation processes in the clouds. Estimating these lapse rates are difficult and beyond the scope of this study, but is required for the heavier noble gases (Ar, Kr, and Xe), as their concentrations in water are highly temperature-dependent. This renders, in principle, He and Ne potential proxies to estimate water source altitudes. However, He concentrations in groundwater are prone to mixing with terrigenic He sources, rendering it less desirable as an altitude proxy than Ne. In particular, it was shown that a significant mantle component is clearly present in some of the Maui groundwater samples, of which R/R_a values are significantly over 1 (this study, Table 5.1 and Appendix C1; Niu et al., 2017b). In addition, it was hypothesized that He concentrations may be affected by an ice-like signature [Niu et al., 2017b]. Thus, Ne is the best candidate for a proxy for water source altitudes. For this estimation, a temperature of 15°C, close to the median water temperature at collection point, is assumed. Under this assumption, the ASW Ne concentration is only dependent on ambient pressure or altitude. For each sample's Ne concentration, an altitude can thus be estimated following Ballentine and Hall [1999]. Figure 5.8 shows estimated altitudes based on Ne plotted against collection altitudes. The solid line represents Ne altitudes that are equal to collection altitudes. All of the rainwater samples yield Ne altitudes above their collection altitudes, with estimates between 0.8 and 2.9 km. As trade wind orographic clouds are typically limited to altitudes 0.6 – 2.4 km [Giambelluca and Nullet, 1991], the two estimated altitudes ~2.9 km are unlikely for orographic rain events. It is possible that these two rainwater samples result from mixing of clouds at different altitudes, and this calls for more studies to further test this Ne altitude proxy. All basal aquifer samples' Ne altitude range between -0.1 and 1.1 km. Eighteen out of 26 spring samples yield Ne altitudes are between -0.5 and 1.3 km, close

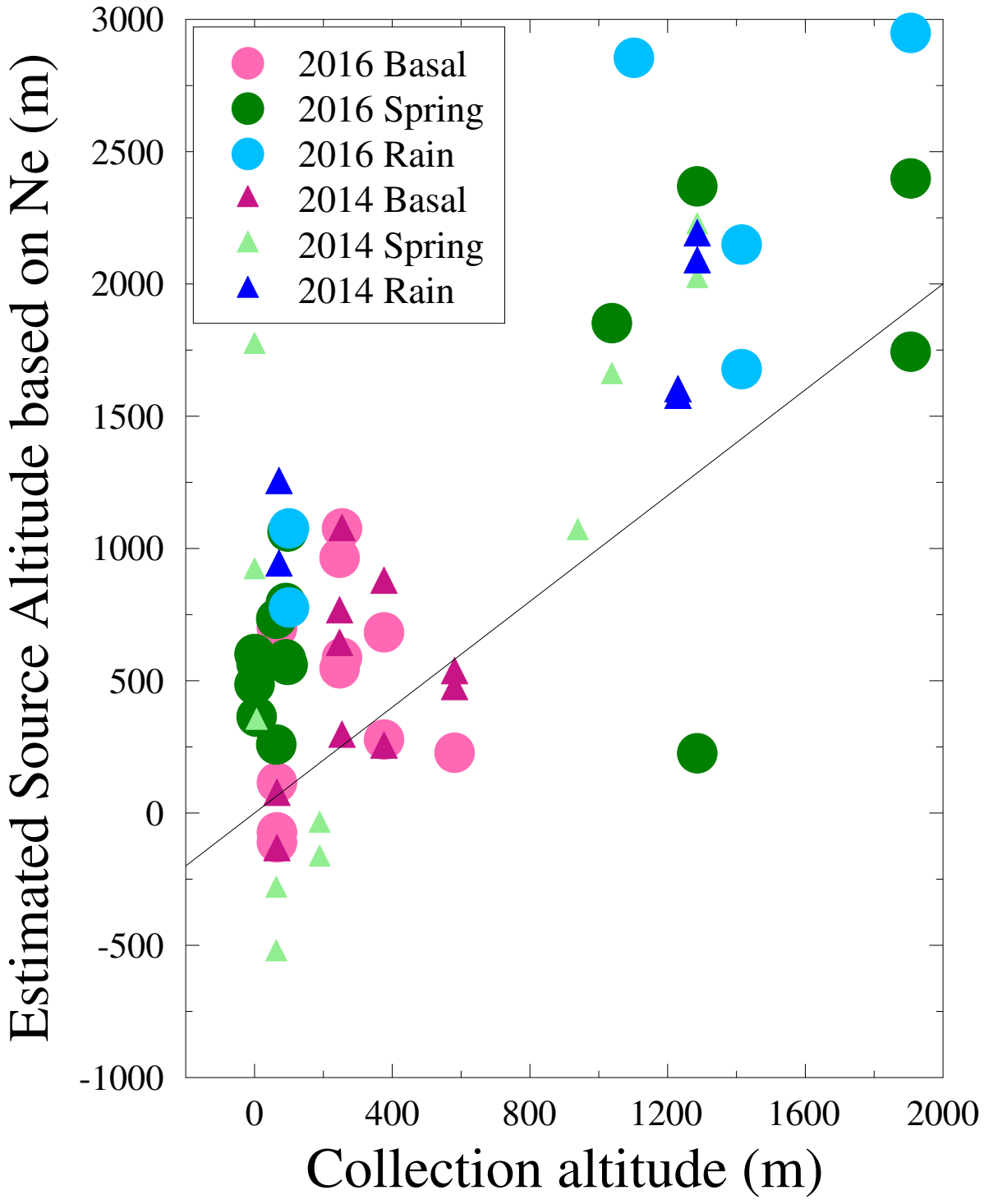

Figure 5.8 Estimated water source altitude based on Ne concentration versus collection altitude for all samples in both years. Source altitudes are estimated based on each sample's measured Ne concentration and assuming equilibration at 15°C. The solid line indicates equal values on both axes.

to the basal aquifer sample's altitude range, while eight spring samples yield estimates ranging between 1.7 and 2.4 km. Overall, rainwater samples collected at higher altitudes yield higher estimated source altitude. Similarly, most groundwater samples display Ne altitudes higher than their collection altitudes, and higher collection altitude correlate with higher Ne altitudes. However, some groundwater samples yield Ne altitudes lower than their collection altitudes, in particular, Ne altitude estimates that are below sea level, as mentioned above. This is likely due to EA, which biases groundwater's estimated altitudes low but it is unlikely to affect rainwater's estimates. It should be noted that once rain droplets exit the clouds, noble gases continue to diffuse into the water droplets, as differences between noble gases dissolved in water and ASW noble gas compositions persist. Therefore, these Ne altitude estimates are a means to provide constraints on the lower limit of the water source altitudes. For rainwater samples, the altitude estimates are expected to constrain the cloud's altitude, and for groundwater samples, the estimates constrain recharge altitudes. However, again, these Ne altitudes correspond to a minimum. Recharge altitudes for both spring and basal water are likely significantly higher than those reported here. This represents a first attempt to use Ne as an altitude proxy and it is thus an exploratory exercise. More studies are needed to further constrain the physical parameters like equilibration temperature, lapse rate, and EA, in order to use atmospheric noble gases to reconstruct equilibration altitude.

5.4.3.2 Water source altitude based on stable isotopes

Figure 5.9 displays water source altitudes based on $\delta^{18}O$, estimated by assuming a starting point of $\delta^{18}O = 0$ at sea level. Altitudes are based on two $\delta^{18}O$ gradients. The lower line, indicating minimum possible altitudes, is bounded by the average of five fog samples in Maui [Scholl et al., 2002; 2007] that yielded a gradient value of -1.8‰ / km, which happens to be the same value in Sicily, Italy, in the Mediterranean [Liotta et al., 2006]. The upper line, providing an upper altitude value, is based on a $\delta^{18}O$ gradient of -1‰ / km, the lowest value observed across the globe [Clark, 1987; Clark & Fritz, 1997]. This model assumes a linear relationship between water source altitude and the $\delta^{18}O$ value found in a sample.

Based on the two possible $\delta^{18}O$ gradients, source altitudes for most groundwater samples range between ~1.5 and 5.5 km asl with the highest spring sample likely originating between 4 and 7 km asl. Basal aquifer samples exhibit estimated water source altitudes between 1.9 and 3.1

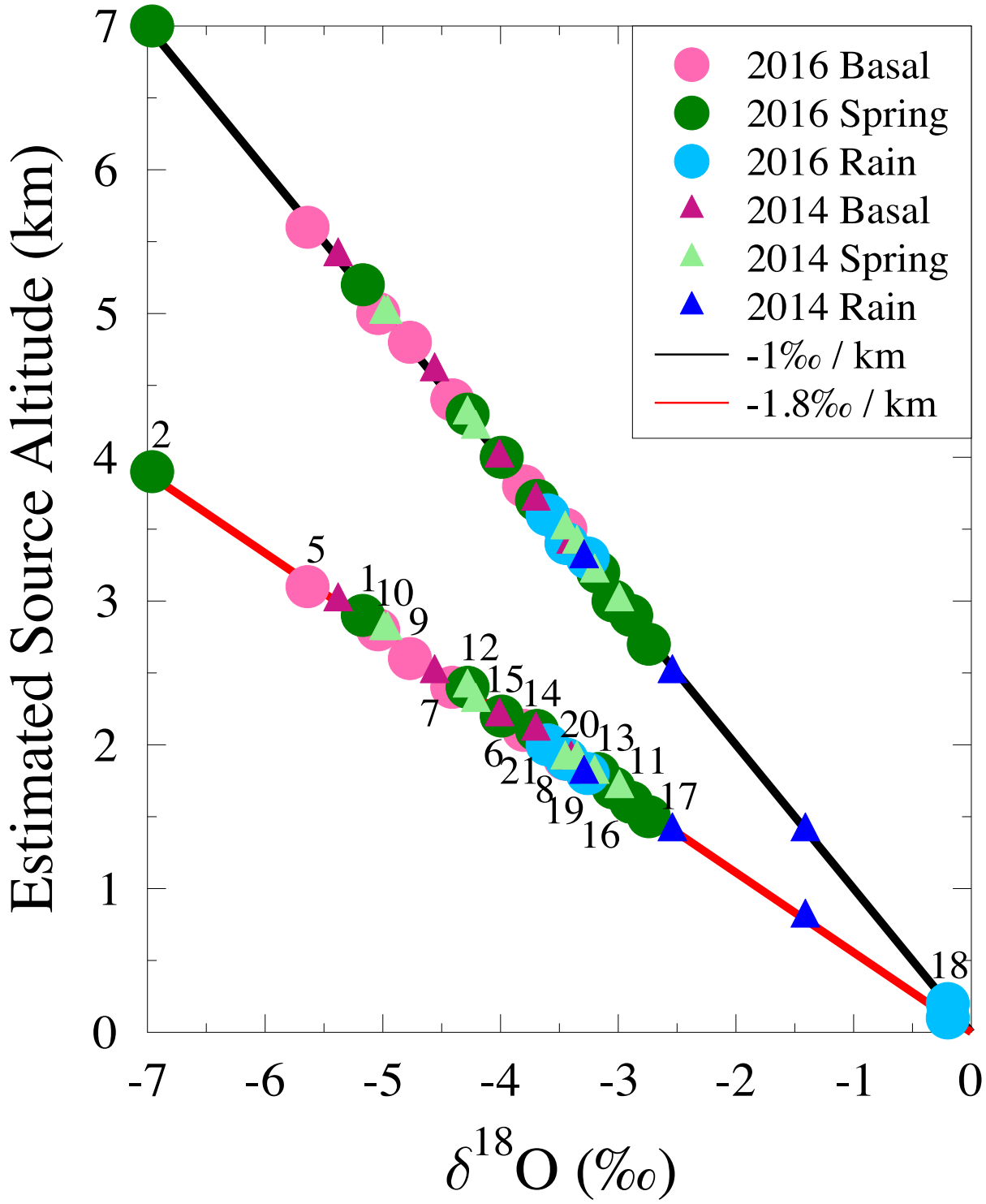

Figure 5.9 Estimated water source altitude based on $\delta^{18}O$ versus measured $\delta^{18}O$ for all samples in both years. The lower line assumes an average $\delta^{18}O$ gradient bounded by fog samples in Maui [Scholl et al., 2002; 2007]. The upper line assumes the lowest gradient observed across the globe [Clark, 1987; Clark & Fritz, 1997].

km. In contrast, eight spring samples exhibit estimated source altitudes between 2.1 and 2.9 km while eight other spring samples yield elevations between 1.5 and 1.9 km. Sample #2 from the Polipoli spring at 1.9 km asl yield an estimated elevation of ~4 km. Overall, about half of the spring samples yield similar source altitudes as the basal samples, while about half of the springs yield much lower water source altitudes than the basal samples. This corroborates with the observation in both sampling seasons that spring samples display more diverse noble gas concentration patterns, representing more diverse water sources, while the basal aquifer likely receives water from more homogenous sources. Although the estimated source altitudes for basal aquifer samples (1.9 – 3.1 km) are lower than the typical altitudes where synoptic-scale events occur, the possibility of mixing between synoptic-scale rain from higher altitudes and orographic rain from lower altitudes cannot be excluded. If the contrast between estimated source altitudes of the basal aquifer and half of the spring samples is because of mixing between different fractions of synoptic-scale and orographic precipitation, this is consistent with the notion that the basal aquifer is predominantly recharged by synoptic-scale precipitation while springs are recharged by more localized orographic rain.

In Figure 5.10, the source altitude estimates based on both Ne concentration and $\delta^{18}O$ values assuming a gradient of -1.8‰ / km are plotted against each other, with a black solid line showing equal values on both axes. The red dotted line in Figure 5.9 represents the best fitting line of all rainwater samples. Overall, estimates for rainwater based on the two sets of data agree with each other far better than those for the basal aquifer and spring samples, with an R^2 value of 0.60 for all of the rainwater samples and a slope of ~0.7. This best fitting line suggests that for source altitudes around 2.5 km asl, the two estimates agree very well. The estimated source altitudes of rainwater samples from the two methods range between 0.1 and 3 km, roughly the same altitude range of the island (0–3.1 km asl). The mixing between synoptic-scale rain and orographic precipitation inevitably leads to lower estimated source altitude for the synoptic-scale rain end-member, which originates above the island, i.e., from altitudes higher than 3 km asl. However, it is not possible to quantify this mixing effect at this point. Most basal aquifer and spring samples yield $\delta^{18}O$ altitudes higher than their respective Ne altitudes. This is partially because Ne altitudes of groundwater can be biased to low values due to the presence of EA, as discussed in section 4.3.1. Thus, the presence of EA and possible equilibration with the

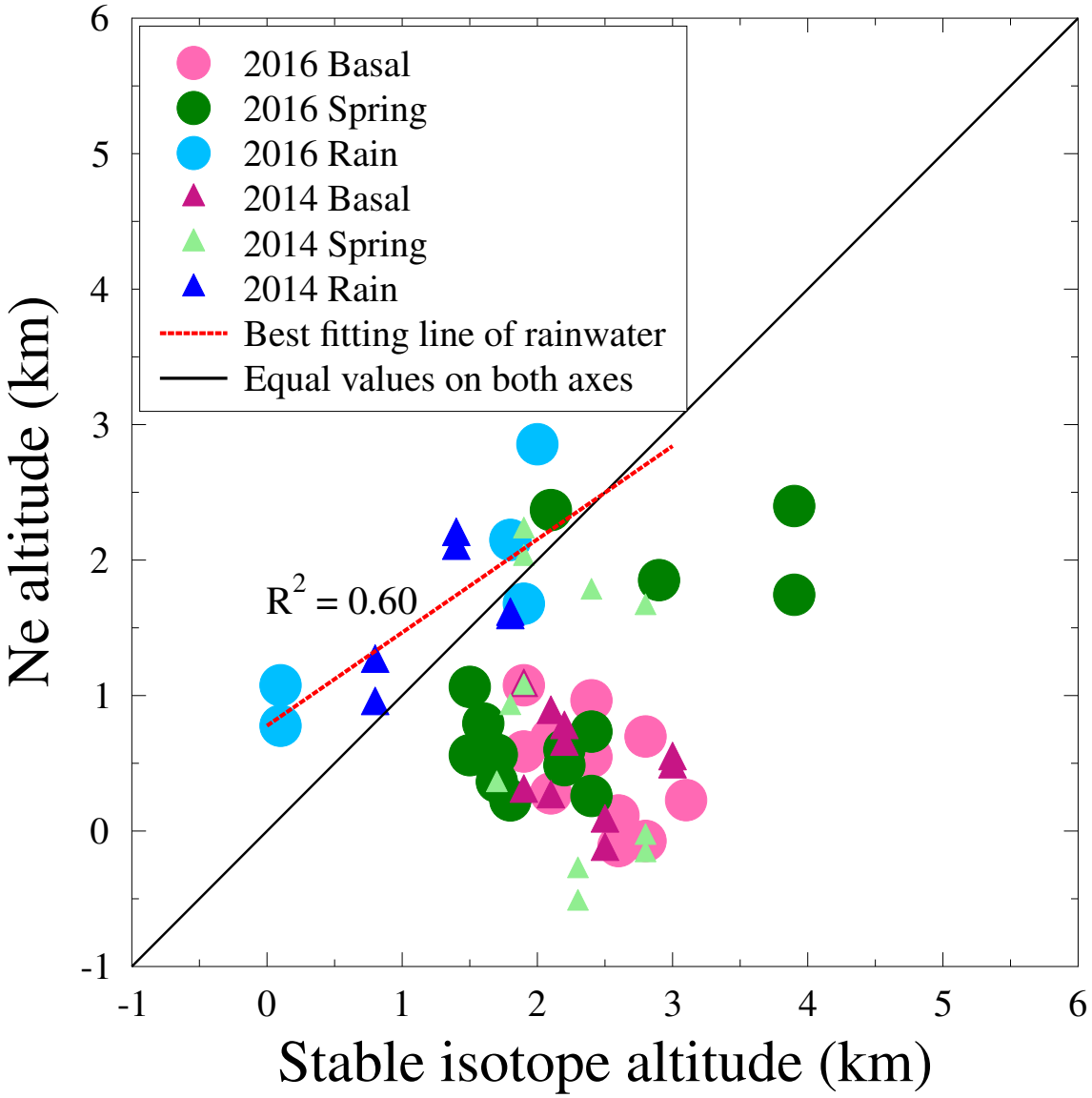

Figure 5.10 Estimated source altitude based on Ne concentration (cf. Figure 5.8) and that based on $\delta^{18}O$ values assuming a gradient of -1.8‰ / km (cf. Figure 5.9) are plotted against each other. The best fitting line for all rainwater samples is expressed by y = 0.6882*x + 0.7771, where x and y denote the altitude estimates based on $\delta^{18}O$ and Ne concentration, respectively.

atmosphere over time appear to be the limiting factor when it comes to the use of Ne as a tracer of source altitudes.

5.4.4 Tritium/^{3}He ages (groundwater residence times)

The noble gas and stable isotope analyses record seasonal climatic signals for all samples, except for noble gases in the basal aquifer. Preservation of seasonality is dependent on short

groundwater residence times among other factors [e.g., Stute and Schlosser, 1993; Thoma et al., 2011]. Below, we provide an estimate of groundwater residence times for both basal aquifer and spring samples based on the presence of tritiogenic ^{3}He ($^3He_{trit}$), which results from decay of natural tritium. Overall, we conclude that spring samples display relatively young ages while the basal aquifer display older ages, which might explain why a seasonal noble gas signature is less obvious in the basal aquifer.

As pointed out by Warrier et al. [2012] in a study of the basal aquifer and springs in the Galápagos Islands, the basal aquifer samples are more prone to mixing of mantle He, which renders the estimation of $^3He_{trit}$ more difficult and inaccurate than those of the spring samples. Therefore, Warrier et al. (2012) opted not to make such estimation for the basal aquifer samples. In this study, however, tritium measurements are available for four wells tapping the basal aquifer (Pookela, site #5, Haiku, site #7, Ohanui, site #8, and Keanae, site #9; Figure 5.1) and a rain event at Waikamoi, site #14, which were collected in June 2014 (Table 5.3; Figure 5.1). Below, we present apparent tritium/^{3}He age estimates for basal aquifer samples in 2014 using measured tritium concentrations when available, and age estimations using assumed tritium concentrations for the basal aquifer and spring samples when measured tritium concentrations are not available.

As mentioned above, basal aquifer samples are prone to mixing of mantle He, as is observed in selected wells in Maui in both sampling campaigns. In addition, because the atmospheric He and Ne components in these basal aquifer samples may be affected by an ice-like end-member, the methods used for $^3He_{trit}$ estimation [Jenkins, 1987; Schlosser et al., 1989] are subject to larger errors in these samples. Therefore, it is of interest to start with the assumption that all ^{4}He is of atmospheric origin and that all excess ^{3}He is tritiogenic and gradually refine the assumptions concerning EA and mantle He components to assess how each assumption affects the estimated tritium age for samples that are not well equilibrated with the atmosphere.

An apparent tritium/^{3}He age can be calculated for each sample as follows [Jenkins, 1987; Schlosser et al., 1988]:

$$[\,^3He]_{trit} = 4.021 * 10^{14} * [He_s * \left({}^{R}/_{R_a} - 1\right) * R_a + He_s * R_a * (1 - \alpha)] \qquad (5.1)$$

and

$$\tau = T_{1/2} / \ln 2 * \ln(1 + [^3He]_{trit}/[^3H]) \qquad (5.2)$$

Table 5.3 Apparent tritium/^{3}He ages calculated based on measured tritium concentrations for basal aquifer samples collected in June 2014 and on assumed tritium concentrations for basal aquifer and spring samples collected in 2016. All excess ^{3}He is assumed to be tritiogenic and EA is assumed to be zero. Measured tritium concentrations of samples collected from four wells tapping the basal aquifer and a rain event in 2014 are listed in the fourth column.

Sample	R/R_a (±1σ)	$^3He_{exc}$ (TU) (±1σ)	Tritium (TU) (±1σ)	Age (years) (±1σ)	Sample	R/R_a (±1σ)	$^3He_{exc}$ (TU) (±1σ)	Assumed Tritium (TU) (±1σ)	Age (years) (±1σ)
2014 Basal					**2016 Basal**				
Pookela-1	1.04 (0.01)	1.37 (0.33)	0.11 (0.09)	47 (14)	Pookela	1.02 (0.01)	0.88 (0.32)	0.10 (0.08)	42 (14)
Pookela-2	1.00 (0.01)	0.52 (0.34)	0.11 (0.09)	32 (16)					
Haiku-1	1.00 (0.01)	0.49 (0.28	0.41 (0.09)	14 (6)	Haiku-1	1.01 (0.02)	0.64 (0.41)	0.37 (0.08)	18 (8)
Haiku-2	1.07 (0.01)	2.16 (0.28)	0.41 (0.09)	33 (4)	Haiku-2	1.04 (0.01)	1.52 (0.32)	0.37 (0.08)	29 (4)
Ohanui-1	0.98 (0.01)	-	0.35 (0.10)	-	Ohanui-1	1.03 (0.02)	1.22 (0.58)	0.32 (0.09)	28 (8)
Ohanui-2	0.93 (0.02)	-	0.35 (0.10)	-	Ohanui-2	1.03 (0.01)	1.16 (0.33)	0.32 (0.09)	27 (6)
Keanae1-1	1.95 (0.02)	30.6 (0.8)	0.69 (0.10)	68 (2)	Keanae1-1	2.08 (0.04)	34.3 (1.2)	0.63 (0.09)	72 (3)
Keanae1-2	1.75 (0.02)	24.2 (0.7)	0.69 (0.10)	64 (2)	Keanae1-2	2.09 (0.03)	34.3 (1.1)	0.63 (0.09)	72 (3)
					Keanae2-1	2.19 (0.03)	34.7 (0.9)	0.63 (0.09)	72 (2)
					Keanae2-2	2.09 (0.02)	34.8 (0.9)	0.63 (0.09)	72 (2)
2014 Rain									
Waikamoi	-	-	0.99 (0.10)	-					
					2016 Springs				
					1a	1.03 (0.01)	1.13 (0.30)	0.90 (0.09)	15 (3)
					2a	1.01 (0.02)	0.58 (0.3)	0.90 (0.09)	9 (4)
					2b	1.03 (0.01)	0.94 (0.30)	0.90 (0.09)	13 (3)
					11a	0.92 (0.01)	-	0.90 (0.09)	-
					11b	0.99 (0.01)	0.07 (0.35)	0.90 (0.09)	1 (6)
					12a	1.17 (0.02)	4.67 (0.51)	0.90 (0.09)	33 (2)
					12b	1.17 (0.02)	4.78 (0.46)	0.90 (0.09)	33 (2)
					13	0.99 (0.02)	0.19 (0.45)	0.90 (0.09)	3 (7)
					14	1.02 (0.02)	0.61 (0.27)	0.90 (0.09)	9 (3)
					15a	1.47 (0.03)	13.3 (0.7)	0.90 (0.09)	49 (2)
					15b	1.35 (0.02)	9.87 (0.51)	0.90 (0.09)	44 (2)
					16a	0.98 (0.01)	-	0.90 (0.09)	-
					16b	1.00 (0.01)	0.40 (0.36)	0.90 (0.09)	7 (5)
					17a	1.02 (0.02)	0.89 (0.43)	0.90 (0.09)	12 (4)
					17b	1.00 (0.01)	0.45 (0.32)	0.90 (0.09)	7 (4)

where $[^3He]_{trit}$ is the estimated tritiogenic ^{3}He concentration in TU (tritium unit); He_s is the measured He concentration of the sample in cm^3 per gram of water at STP (cf., Table 5.1); α is the solubility isotopic fractionation (0.983) to account for the slightly higher solubility of ^{4}He than that of ^{3}He in water [Benson and Krause, 1980]. The correction term for salinity of the water sample following Schlosser et al. [1988] is omitted, because reported helium and tritium concentrations are both normalized to zero salinity. In this calculation, it is assumed that all ^{4}He is of atmospheric origin and that all excess ^{3}He with respect to an R/R_a value of 0.983 is tritiogenic. This assumption will overestimate the ages for samples with significant mantle He

contributions. However, as discussed below, we cannot accurately separate the mantle He components and such attempts yield negative estimates of $^3He_{trit}$. Therefore, age estimates following this assumption are presented in Table 5.3. Age estimates for two samples from the Pookela well are close to each other and yield ages of 47 ± 14 years and 32 ± 16 years, while the two samples from Haiku wells are distinct, being 14 ± 6 years and 33 ± 4 years. Because the R/R_a values of Keanae well 1 are around 1.9, it is likely that mantle He has a significant contribution, as discussed in Niu et al. [2017b]; therefore, the age estimates for these two samples, ~66 ± 2 years are expected to be overestimates. It is relevant to note that Eq. 5.1 is a simplification of Eq. 5.3 below, after Schlosser et al. [1988], by assuming that $He_s = He_{eq}$:

$$[\,^3He]_{trit} = 4.021 * 10^{14} * [He_s * \left({}^{R}/_{R_a} - 1\right) * R_a + He_{eq} * R_a * (1 - \alpha)] \qquad (5.3)$$

where He_{eq} is the He concentration in solubility equilibrium with the atmosphere.
When it is assumed that there are no terrigenic He sources, He_{eq} is estimated according to [Schlosser et al., 1989]:

$$He_{eq} = He_s - (Ne_s - Ne_{eq}) * (He/Ne)_{atm} \qquad (5.4)$$

where Ne_s is measured Ne concentration and Ne_{eq} is ASW Ne concentration at the collection point (cf. Figure 5.2) and $(He/Ne)_{atm}$ is the He to Ne concentration ratio in the atmosphere of ~0.2882 [Ozima and Podosek, 2002]. Both samples from the Haiku well yield Ne concentrations lower than expected ASW Ne values, so no corrections on He_{eq} are needed or possible for this well. Both samples from the Pookela well yield essentially identical age estimates to those according to Eq. 5.1 of 47 ± 14 years and 31 ± 16 years. With measured Ne concentrations close to ASW values, the correction for an EA component has negligible effect on the estimated ages for these samples. For samples with R/R_a values lower than 0.983 (Ohanui well) or significantly higher than 1 (Keanae well 1), the assumption of an absence of terrigenic He sources does not hold, and tritiogenic ^3He is estimated following Schlosser et al. [1989]. However, the two samples from Keanae well 1 and one sample from Ohanui well yield negative estimated tritiogenic ^3He, while the other sample from Ohanui well yields an apparent age of 27 ± 38 years, or approximately zero when considering the relatively large error. These negative values may result from the estimation of EA component based on Ne excess with respect to assumed ASW values. An age of 47 ± 14 years for a sample collected at Pookela well in 2014 indicates that this sample started with a tritium concentration of ~1.5 TU (sum of estimated $^3He_{exc}$ and measured ^3H; Table 5.3) in the year 1967 or any time between 1953 and 1981, considering the time range

encompassing the 1σ error. This tritium concentration is far less than the measured values in precipitation in Maui in 1969 – 1970, the average value being ~19 TU [International Atomic Energy Agency, https://nucleus.iaea.org/wiser/, 2017]. This indicates that the tritium concentration in local precipitation does not reflect that found in groundwater at the same time. Indeed, of all five samples collected in June 2014 for tritium analysis, the rainwater sample has the highest tritium concentration, 0.99 ± 0.10 TU, compared to the values for the basal aquifer samples, between 0.11 ± 0.09 TU and 0.69 ± 0.10 TU (Table 5.3). It is likely that the relatively high tritium concentration in precipitation is diluted to a lower value when precipitation mixes with groundwater. In summary, the apparent ages of basal aquifer samples are about a few decades old and these estimates are consistent with the fact that a seasonal noble gas signature is less apparent in the basal aquifer. These preliminary conclusions require further in-depth studies in the future.

Apparent water ages for samples collected in 2016 were also estimated based on assumed tritium concentrations. For Pookela, Haiku, Ohanui, and Keanae 1 wells, it is assumed that their tritium concentrations are the remaining tritium from the decay of the measured tritium concentration in 2014 in the corresponding wells. Keanae well 2 (site #10) is assumed to have the same tritium concentration as site #9 based on proximity. Apparent ages are calculated based on Eq. 5.1, and range between 18 ± 8 years and 42 ± 14 years. The four samples from site #9 and #10 yield ages ~72 ± 2 years. All age estimates are similar for the same well in both sampling seasons, again, indicating that noble gases in the basal aquifer do not record temporal variations.

For the 2016 spring samples, tritium concentrations are assumed to be the remaining tritium from the decay of the measured tritium concentration in 2014 in rain (Table 5.3), following the methods described in Warrier et al. (2012). As discussed above, this likely overestimates the tritium concentrations in springs and underestimates the apparent ages of spring samples. Tritiogenic ^{3}He is also estimated following Eq. 5.1. Most spring samples yield ages ranging between 1 ± 6 years (approximately zero) and 15 ± 3 years, while two samples yield negative ages due to R/R_a values below 0.983. Such young ages are likely to allow for the observed variations in noble gases and stable isotopes in these samples. However, these estimates are meant to provide lower limits of the water residence times.

Overall, age estimates of the basal aquifer samples for both years are in agreement within error. Spring samples yield younger ages than basal samples. However, these ages are expected

to represent lower limits. More studies are needed to further constrain the age estimates for springs representing perched aquifers with measurements on both tritium and noble gases.

5.5 Conclusions

This study is a follow-up of a pilot noble gas study in Maui [Niu et al., 2017b] which uses water samples collected in 2014. It further explores the information noble gases and stable isotopes of water can provide in rapid rainwater infiltration systems. In particular, it assesses whether noble gas signatures record temporal variations and how NGTs can be applied to these systems together with stable isotopes to estimate water source and recharge locations.

Most samples collected in both years display a mass-dependent depletion pattern, with concentrations of the heavier noble gases (Ar, Kr, and Xe) being less enriched or more severely depleted than those of the lighter noble gases (He and Ne) with respect to ASW values. Overall, basal aquifer samples display similar noble gas concentration patterns in both years, while rainwater and spring samples display distinct signatures in both sampling seasons. Some rainwater samples in 2016 yield He depletion with respect to ASW and, to our knowledge, this is the first time that He depletion is observed in rainwater. Three rainwater samples from 2016 display stable isotope data consistent with orographic rain and noble gas concentrations inconsistent with an ice-like signature, which would suggest rain originating at altitudes higher than orographic rain. Springs display greater variations in noble gas concentrations between the two sampling seasons than the basal aquifer. Leeward springs yield higher noble gas concentrations in 2016, while most windward springs yield lower noble gas concentrations in 2016 than in 2014. This likely indicates that different water sources, i.e., synoptic-scale and orographic rain, are affected by changes in weather conditions in different manners. Wells and springs where elevated R/R_a values were registered in 2014 yield similar R/R_a values in 2016, and the estimated R/R_a values for the terrigenic He component from both years, ~8 – 10, are close to that of MORB type mantle He source.

The water stable isotope samples display deuterium excess ranging between 13‰ and 29‰. Overall, the 2016 samples have greater deuterium excess than the 2014 samples, consistent with the drier El Niño climate of 2016 [Clark & Fritz, 1997; Huang et al., 2016]. Three rainwater samples in 2016 display significantly higher deuterium excess (~28‰) compared to all others. Rainwater samples from both years are isotopically the heaviest, representative of the heavy end-

member of the groundwater sources. Overall, basal aquifer samples yield lower $\delta^{18}O$ and higher δD values in 2016 than in 2014, while spring samples do not display a specific trend.

Estimated source altitude based on Ne concentrations range between 0.8 and 2.9 km for rainwater samples, all higher than each sample's collection altitude. However, two rainwater samples yield altitude estimates ~2.9 km, where orographic clouds are typically absent [Giambelluca and Nullet, 1991]. These altitude estimates may result from mixing of water sources from different altitudes. Overall, estimated source altitude for rainwater samples correlates well with the collection altitude. Most samples from the basal aquifer and springs display Ne altitudes higher than their collection altitudes, but some yield Ne altitudes lower than their collection altitudes, likely because the presence of EA biases their estimated altitudes low. Estimated source altitudes based on measured $\delta^{18}O$ and possible $\delta^{18}O$ gradients for most groundwater samples range between 1.5 and 5.5 km asl. Overall, basal aquifer samples have higher source altitudes than about half of the spring samples, consistent with previous findings that the basal aquifer is predominantly recharged by synoptic-scale rain originating from higher altitudes than localized precipitation forming within the island. In summary, a combined dataset of noble gas concentrations and water stable isotopic compositions appears to have the potential to identify water sources and estimated water source altitudes. Additional studies are required to further test the assumptions in these altitude proxies.

Water samples were collected in 2014 for tritium analyses from the basal aquifer in addition to a rain event. Tritium/^{3}He ages of the basal aquifer samples range between 14 ± 6 years and 47 ± 14 years. These relatively long water residence times are consistent with the finding that a temporal noble gas signature is less apparent in the basal aquifer. Spring samples show younger ages ranging approximately from zero to 15 ± 3 years. Such young ages are likely to allow for the observed temporal variations in noble gases and stable isotopes in these samples. These preliminary conclusions require further in-depth studies in the future.

5.6 Acknowledgments

Financial support by the University of Michigan, the NSF Hydrological Sciences (award EAR-1344357), and the NSF Instrumentation & Facilities (award EAR-1049822) is greatly appreciated. We thank Lora Wingate and Phoebe Aaron for the analyses of $\delta^{18}O$ and δD. We thank Dr. Jürgen Sültenfuß for analyses of tritium.

CHAPTER VI
Conclusions

This final chapter provides a summary of the major results of each chapter and a brief concluding remarks of the overall work presented.

6.1 Summary of Major results

Chapter 2: This chapter presents the first comprehensive stable noble gas study in glacial meltwater. It utilizes stable noble gases in meltwater from the Greenland Ice Sheet (GrIS) to explore the information noble gases can provide in glacial environments. Most GrIS glacial meltwater samples are in disequilibrium with surface conditions. A partially equilibrated air-saturated water (ASW) component dominates over any possible excess air (EA) component including one originating from the trapped air in glacial ice for Ne, Ar, Kr, and Xe. Overall, one group of samples displays a mass-dependent depletion pattern with stronger depletion of the heavier noble gases compared to the lighter ones. The second group displays a relative Ne depletion with respect to Ar, Kr, and Xe. Much of the GrIS glacial meltwater originates at altitudes between 1 and 2 km above sea level (asl), as indicated by their Ne and Xe concentrations. Two samples suggest an origin as melted ice with complete lack of equilibration with surface conditions. A helium component analysis suggests that this glacial meltwater was isolated from the atmosphere prior to the 1950s, with most samples yielding residence times between 110 and 420 years, and two samples yielding ~1900 years and 3600 years. Most samples represent a mixture between a predominantly atmospheric component originating as precipitation and basal meltwater or groundwater, which has accumulated crustal ^{4}He over time.

Chapter 3: This study represents the first comprehensive noble gas study in meltwater of an alpine glacier, which is from the Athabasca Glacier meltwater (AGMW), Columbia Icefield, Canada. Both the mass-dependent depletion pattern and relative Ne depletion with respect to Ar

Kr, and Xe are observed, previously seen in the GrIS meltwater [cf., Chapter 2]. Different gases have different degrees of equilibration and samples are far from equilibration with the atmosphere at any temperature compatible with the glacial environment. Xe concentrations alone suggest that all samples equilibrated with the atmosphere at altitudes between 2500 m and 3400 m asl, compatible with the altitude range (1900 – 3500 m) of the Columbia Icefield. Most samples display Xe equilibration altitudes above the maximum altitude of the AG (~2700 m), suggesting that a significant portion of the current AGMW originates in the Columbia Icefield. All samples are largely dominated by surface melt as opposed to basal melt, similar to the finding at GrIS [Chapter 2]. Basal melt and/or groundwater represent at most 4% – 29% of the total glacial meltwater. With the exclusion of one present day sample, the bulk of the AGMW is likely a mixture between pre-bomb and present time GMW with a most likely average residence time of ~160 years.

Chapter 4: This study represents the first comprehensive stable noble gas study in the Island of Maui, Hawaii, to explore the potential for noble gases in characterizing fractured hydrologic systems in volcanic islands. Noble gases in Maui rainwater and the basal aquifer display an ice-like signature and are not representative of the mean annual air temperature. The distinct noble gas patterns for the basal aquifer and springs suggest that basal and perched aquifers are separate entities, reinforcing the findings from previous studies in Maui. Noble gases of all samples fall on a mixing trend between an ice-like and an ASW end-member with the possible addition of a mantle He source in the groundwater samples. A mantle He component was observed in springs and well sites on both the windward and the leeward sides of the Island and this He component appears to be an almost pristine Mid-Ocean Ridge Basalt (MORB) source.

Chapter 5: This study is a follow up of the pilot noble gas study conducted in Maui and further explores the information noble gases and stable isotopes of water can provide in rapid rainwater infiltration systems in terms of temporal variations and water source altitudes. It is complemented by estimating water residence times for the basal aquifer and springs using tritium measurements and excess ^{3}He estimates. Overall, basal aquifer samples display similar noble gas concentration patterns in both years, while rainwater and spring samples display distinct signatures in both sampling seasons. Springs display greater variations in noble gas concentrations between the two sampling seasons than the basal aquifer. Basal aquifer samples

yield lower $\delta^{18}O$ and higher δD values in 2016 than in 2014, while spring samples do not display a specific trend. The estimated source altitudes of rainwater samples from Ne concentration and $\delta^{18}O$ range from 0.1 to 3 km. A combined dataset of noble gas and water stable isotopes appears to have the potential to identify water source and altitude. Tritium/^{3}He ages of basal aquifer samples range from 14 ± 6 years to 47 ± 14 years, while spring samples yield ages ranging from zero to 15 ± 3 years. Older ages of the basal aquifer are consistent with lower sensitivity to seasonal variations in this aquifer compared to perched aquifers. Perched aquifers' young ages likely allow for the observed variations in noble gases and stable isotopes in spring samples between 2014 and 2016.

6.2 Overall Conclusions

This dissertation focuses on applications of stable noble gases in hydrogeology in fractured flow systems with rapid infiltration. It explores the information that noble gases can provide in glacial environments in terms of glacial hydrology near the terminus area, water source altitude, and groundwater residence times, as well as in basaltic fractured systems in terms of aquifer connectivity, precipitation types, and water source altitudes. This dissertation investigated thirteen glacial meltwater samples from five outlet glaciers of the Greenland Ice Sheet, 8 glacial meltwater samples from Athabasca Glacier of Columbia Icefield in the Canadian Rocky Mountains, fifty-nine water samples from eleven springs, six wells tapping the basal aquifer, and eight rain events in the Island of Maui, Hawaii, over the course of two sampling campaigns. Stable noble gases in glacial meltwater prove to be a useful tool in investigating the glacial hydrology and glacier dynamics. The study of dissolved noble gases in rainwater and groundwater, combined with the water stable isotopic composition, provided a better understanding of the local hydrogeology and developed new applications of noble gases in fractured groundwater flow systems. This dissertation has important societal relevance in both glacial environment and tropical islands and can contribute to better understanding of the hydrology in both types of regions, as well as dynamics of glacial meltwater in response to climate change and improved water management plans in tropical islands. This dissertation has important scientific implications in glaciology, hydrogeology, and meteorology.

6.3 Future Research Questions

I propose the following questions and potential focuses for future research in both the glacial environments and fractured systems with rapid infiltration.

1. Is it possible to estimate the rate of basal melting and/or surface melting based on current understanding of the glacier dynamics and interactions between glacier and bedrock, e.g., rate of internal deformation (creep), rate of basal sliding and topography of bedrock, rate of soft bed subglacial deformation, geothermal flux, etc.? How would these compare to the finding in the noble gas studies presented in this thesis?
2. The studies in Maui presented in this thesis assumed a binary mixing model between ice-like and ASW end-members, which was over-simplified, as acknowledged in Chapter 4. The true equilibration process is likely to be a complex function of multiple factors, including temperature dependent diffusion coefficients in air and water for each noble gas. A model of this equilibration process of noble gases starting from the ice-like end-member may help us get a better understanding of disequilibrium of noble gases between air and both the rainwater and groundwater samples.
3. Karstic systems, like basaltic islands, also have preferential flow paths. What information can noble gases provide in these systems with respect to water sources and seasonal or annual records? Given that the carbonate rocks readily react with the water in karstic systems, what information can water stable isotopes provide? Do the water-rock interactions play a major role in dictating the water compositions? Or do water source types and/or source altitudes have large influence on water compositions, given the relatively short water transit time due to the preferential flow paths?

APPENDICES

Additional text, tables, and figures that support the main results presented in Chapters 2, 4, and 5 are provided in Appendices A, B, and C, respectively.

Appendix A includes supplementary text A1 (Separation of He components) and A2 (Calculation of ^{4}He production rates and residence times).

Appendix B includes supplementary text B1 (He component separation) and three figures (Figures B1 – B3).

Appendix C includes supplementary text C1(He component separation) and one figure (Figure C1).

APPENDIX A

Supplementary materials for Chapter 2

A1. Separation of He components.

This analysis is typically done by plotting R_{noea}/R_a versus $^4He_{eq}/^4He_{noea}$ [e.g., Castro, 2004], where R_{noea} and $^4He_{noea}$ are the $^3He/^4He$ ratios and total measured ^4He concentration at collection conditions after removal of EA, and $^4He_{eq}$ is the ASW ^4He concentration under collection conditions (Figure 2.7). The EA components are estimated using Ne, Ar, Kr, and Xe concentrations in the NGT model described in Ballentine and Hall [1999] for the four samples with Ne excess and assumed to be 0 for the nine samples with Ne depletion. More details and applications can also be found in Saar et al. [2005]. R/R_a crustal and mantle end-members are assumed to be 0.02 [O'Nions and Oxburgh, 1983] and 8 [Farley and Neroda, 1998], respectively (Figure 2.7). Lines with varying contributions of crustal and mantle He as well as tritiogenic ^3He are represented. In this graphic, a sample displaying a value of 1 in the horizontal axis points to a component of atmospheric origin in its entirety, while a value approaching 0 points to a solely crustal origin. Increasing values on the left vertical axis denote increasing mantle contributions, while increasing values on the right vertical axis reflect increasing tritiogenic ^3He amounts (in tritium units, TU). Samples plotting along a particular line represent varying contributions of these components.

A2. Calculation of ^4He production rates and residence times.

^4He production rates in basement rocks are calculated as follows [Ballentine et al., 1991]:

$$P\,(^4He)_{rock} = 1.207\times10^{-13}\,[U] + 2.867\times10^{-14}\,[Th]\ cm^3\ STP\ g_{rock}^{-1}\ yr^{-1}$$

where [U] and [Th] represent the U and Th concentrations in average granodiorite and granite formations [Parker, 1967] which are among the most common rocks in our study area [Baadsgaard, 1973; Friend and Nutman, 2005; Dawes, 2009; Klint et al., 2013]. U and Th concentrations, which are higher in felsic granites and granodiorites ([U] = 3.5ppm; [Th] =

18ppm) are used to estimate minimum water ages and those in high calcium granites, with lower U and Th concentrations ([U] = 3ppm; [Th] = 17ppm), are used to estimate maximum water ages. ^{4}He accumulation rates in water, P (^{4}He)$_{H2O}$, were subsequently estimated according to:

$$P\,(^4\mathrm{He})_{H2O} = P\,(^4\mathrm{He})_{rock} * \rho_r * \Lambda * (1-\omega)/\omega \ \mathrm{cm}^3\ \mathrm{STP}\ \mathrm{cm}_{H2O}^{-3}\ \mathrm{yr}^{-1}$$

where ρ_r is the mass density of the rock, assumed to be 2.7g/cm^3; ω is the porosity of the basement rock, assumed to be 2.5%, the average value of unweathered, dense crystalline rocks [Domenico and Schwartz, 2008]. Λ, which is the transfer efficiency of ^{4}He from the rock to the water is assumed to be 1 [Torgersen et al., 1989].

Using ^{4}He production rates, residence times can be estimated based on ^{4}He$_{exc}$. It is plausible to assume that both groundwater and surface water have comparable ASW values. This assumption should be applicable in the terminus area of glaciers where temperature and altitude at the surface are not very different from those on the bottom. The build up of radiogenic 4He in the groundwater component is used to differentiate groundwater from surface water and to calculate the respective fractions. The calculated residence times will correspond to the mixing water as a whole, i.e., surface and groundwater/basal water.

APPENDIX B

Supplementary materials for Chapter 4

B1. He component separation.

The separation and quantification of different He components, i.e., atmospheric, crustal and/or mantle, under certain assumptions, allows for the characterizations of the crustal and mantle He sources. This analysis is typically done by plotting R_{noea}/R_a versus $^4He_{eq}/^4He_{noea}$ [e.g., Weise and Moser, 1987; Stute et al., 1992; Castro, 2004]. We specify

$$He_{noea} = He_s - He_{ea}, \quad (B1)$$

$$He_{exc} = He_s - He_{eq} - He_{ea}, \quad (B2)$$

where He_s are measured total He concentrations, He_{eq} and He_{ea} are the ASW and EA components, respectively, estimated using the unfractionated air (UA) model following Ballentine and Hall [1999]. He_{noea} are the He components excluding excess air. Concentrations of ^3He are given by $^3He_s = {}^4He_s * R$, $^3He_{eq} = {}^4He_{eq} * R_{eq}$, and $^3He_{ea} = {}^4He_{ea} * R_a$, where $R_{eq} = (1.360 \pm 0.006) * 10^{-6}$ [Benson and Krause, 1980] and R are the $^3He/^4He$ ratios for ASW and total measured He, respectively. In addition, we specify [Castro, 2004]:

$$R_{noea} = \frac{^3He_{noea}}{^4He_{noea}} \quad (B3)$$

and

$$R_{exc} = \frac{^3He_{exc}}{^4He_{exc}}. \quad (B4)$$

The ASW and EA components are simultaneously estimated based on Ne, Ar, Kr and Xe concentrations following Ballentine and Hall [1999], assuming equilibration altitudes to be collection altitudes. Although the ASW He component changes with altitude, the sum of He_{eq} and He_{ea} is very insensitive to input altitude. The sum varies by less than 0.5% with input altitude between the collection altitude and the summit (3055 m). Additional details and applications of EA estimation and He component separation can be found in Saar et al. [2005] and Niu et al. [2015; 2017a].

One caveat of this approach is that when the sample retains some of the noble gas signatures of ice, this model will underestimate He_{eq} and therefore the sum of He_{eq} and He_{ea}. Specifically, if Ar, Kr and Xe concentrations of a sample are far from equilibrium with the atmosphere, i.e., far from being ASW, it is likely that the starting point for the water sample was ice or, at least, an ice-like end-member of undetermined origin. As ice has more He with respect to Ar, Kr and Xe than ASW does, the He_{eq} component estimated in an ASW model is lower than that present in the ice structure, and the He_{ea} component is overestimated. This particularly affects spring sample 16, which has the lowest normalized Ar, Kr and Xe concentrations. The estimated sum of He_{eq} and He_{ea} is about 90% of the total measured He concentration. However, it is expected that at least part of the 10% difference results from the bias of the NGT model when applied to a sample with an ice or ice-like signature.

The R_{exc}/R_a estimates (see Table 4.1) are under the assumption that all of the water from springs and basal aquifer are very recent, so they contain no tritiogenic ^3He; this is discussed in detail below and in Figure B1. Most samples, i.e., basal aquifer samples 1a, 1b, 3a, 3b, 4a, 4b, 9a, spring samples 8, 12a, 12b, and rainwater samples 11a, 11b, 13a, 15b, yield R_{exc}/R_a values approximately equal to 1 within 1σ error while sample 13b has an R_{exc}/R_a value of 0.03 ± 0.52, still within a 2σ error of a value of 1. The relatively large errors are a result of the minimal He excesses. With these relatively large errors, the He excesses in these samples are considered to be of atmospheric origin. Samples 9b, 2, 7, 14, and 15a yield negative R_{exc}/R_a estimates reflecting the absence of terrigenic He. Unlike samples 10a, b, which display an almost pure MORB-type mantle He component with R_{exc}/R_a ratios of ~6.9 and 8.5, R_{exc}/R_a ratios for samples 5, 6, and 16 are ill-constrained due to significant errors associated with estimation of these values. Sample 16 has an R_{exc}/R_a value of 4.20 ± 0.86. It possible that mixing between a mantle and a crustal component accounts for this lower R_{exc}/R_a value. If we neglect the possible bias of the NGT model, then a pure mantle component with no crustal He source cannot explain such a low R_{exc}/R_a value in sample 16. Alternatively and more likely, the underestimated atmospheric He concentrations (NGT model bias) lead to low R_{exc}/R_a estimates.

Figure B1a shows a plot of R_{noea}/R_a versus $^4He_{eq}/^4He_{noea}$ for all Maui samples. Colored solid lines indicate the expected position for samples with tritiogenic ^3He levels varying from 0 to 13 TU and 0% mantle contribution while red dashed and/or dotted lines indicate mantle

contributions ranging from 20% to 100% and tritiogenic ^{3}He level of 0 TU. The lines are calculated based on

$$R_{noea}/R_a = \frac{{}^4He_{eq}R_{eq} + {}^4He_{exc}R_{exc} + {}^3He_{trit}}{{}^4He_{noea}R_a} \quad \text{(B5)}$$

and rearranged to

$$R_{noea}/R_a = (kx + R_{exc}) / R_a \quad \text{(B6)}$$

where, $k = R_{eq} - R_{exc} + {}^3He_{trit} / {}^4He_{eq}$, (B7)

$$x = {}^4He_{eq} / {}^4He_{noea}, \quad \text{(B8)}$$

and

$$R_{exc} = f_m R_m + (1- f_m)R_c. \quad \text{(B9)}$$

The term f_m, indicated near the red lines, corresponds to the fraction of the mantle contribution and $(1-f_m)$ is the crustal fraction of the terrigenic end-member. R_c is the crustal end-member of ^{3}He/^{4}He ratio and is assumed to be 0.02 [O'Nions and Oxburgh, 1983], and R_m is the mantle end-member of ^{3}He/^{4}He ratio. Mantle R/R_a (R_m/R_a) values in Mid Ocean Ridge Basalts (MORB) and Ocean Island Basalts (OIB) are ~ 8 and 50, respectively [Graham, 2002; Starkey et al., 2009]. Different R_m/R_a values were assigned in order to find the appropriate value that makes the red dotted line plot in the vicinity of samples 10a and 10b. The x coordinate indicates the He fraction contributed by ASW. The fraction of terrigenic end-member is (1-x). In this graphic, a sample displaying a value of 1 on the horizontal axis points to a component of purely atmospheric origin, while a value approaching 0 points to a solely terrigenic origin. Increasing values on the left vertical axis denote increasing mantle contributions, while increasing values on the right vertical axis reflect increasing tritiogenic ^{3}He levels (in TU; 1 TU is equivalent to $2.5 * 10^{-15}$ cm^3 of ^{3}He per gram of water). Samples plotting along a particular mixing line represent varying contributions of these components.

Most samples plot near the right-axis and are thus dominated by an atmospheric component. Samples 5a, 5b, 10a, and 10b exhibit significant mantle He components. In fractured systems like Maui, infiltration is very rapid. Therefore, the accumulation of radiogenic ^{4}He produced in the basaltic bedrock is likely minimal. Consequently, if a sample with a significant terrigenic He source plots on a line representing a mixture of atmospheric and a pure mantle source with no crustal He, the ^{3}He/^{4}He ratio in the mantle end-member can be estimated from the slope of the line. From Figure B1a, it is apparent that when R_m/R_a is assumed to be 8.5, sample 10b plots very close the line representing a pure mantle component corresponding to a MORB

source (R/R_a = 7 – 9) [Farley and Neroda, 1998]. Assuming a crustal component is negligible, 8.5 represents the mantle end-member in this area. According to Kurz et al. [1987], R/R_a values of the Hanā Basalt are indeed about 8, indistinguishable from that of MORB. Within error, sample 5b lies on the line representing a pure mantle component with an R/R_a value of 8.5, similar to that of sample 10b. These values fall in the range of $^3He/^4He$ ratios (R/R_a = 6 – 36) found in Hawaii by earlier studies compiled in Farley and Neroda [1998], although we did not observe values higher than those corresponding to a MORB source in our Maui samples. Figure B1b is a zoom-in view of the samples dominated by ASW. A solid orange line representing 2 TU of $^3He_{trit}$ is also shown. All rainwater samples are compatible with $^3He_{trit}$ levels between 0 and 2 TU. Given these levels, it is expected that rainwater has negligible tritiogenic ^3He. A value of 2 TU is likely overestimated given the errors associated with these estimations. Because rainwater shows almost complete absence of tritiogenic ^3He, it is unlikely that spring samples 6a, 6b, and 16, with R_{noea}/R_a values of 1.32 ± 0.04, 1.40 ± 0.05, and 1.31 ± 0.03, respectively, would display apparently higher tritiogenic ^3He levels, between 10 TU and 12 TU (Figure B1b). These slightly higher than atmospheric R_{noea}/R_a values are more likely to result from a mixture between a minor crustal component and mantle sources, accounting for 4%, 3%, and 10% of the He concentrations without the EA component for samples 6a, 6b, and 16 respectively.

The above discussions are based on the assumption that heavy noble gases, especially Xe, are in equilibrium with the atmosphere at a certain altitude and temperature. However, this is not the case for the Maui samples. And as discussed above, the caveat of the NGT model is that the EA component is overestimated. Therefore, it is necessary to provide constraints on the He components by underestimating the EA component. A plot of He/Ar versus Ne/Ar is consistent with no EA being present in most samples (Figure B2). Almost all of the samples plot above the line representing ASW values between 20°C and 35°C, while the EA arrows originating from points presenting ASW values are below the ASW line. However, one caveat of this plot is that the EA in any sample may be masked by the addition of mantle He, which moves a sample vertically up. Therefore, it is possible to assume no EA when attempting to separate the He components and this is an absolute lower bound on actual EA values. Assuming no EA, $^4He_{eq}/^4He_{noea}$ on the horizontal axis in Fig. 1 reduces to $^4He_{eq} / {}^4He_s$, and R_{noea}/R_a on the vertical axis reduces to measured R/R_a values for the samples. Results in Figure B3 suggest that sample 10b falls on the line assuming binary mixing of ASW and a mantle He end-member with R/R_a =

8. This estimate of mantle R/R_a under the assumption that there is no EA in samples is close to that under the assumptions which overestimate the amount of EA. This suggests that the mantle He that mixes with selected springs and groundwater wells has an R/R_a of about 8 to 8.5.

Based on the considerations above, a mantle He component corresponding to 17%, 14%, 3%, 3%, 48%, 44%, and 10% for samples 5a, b, 6a, 6b, 10a, b, and 16, respectively, was removed from the total He concentrations in Figure 4.2b, following the results estimated in the UA model following Ballentine and Hall [1999].

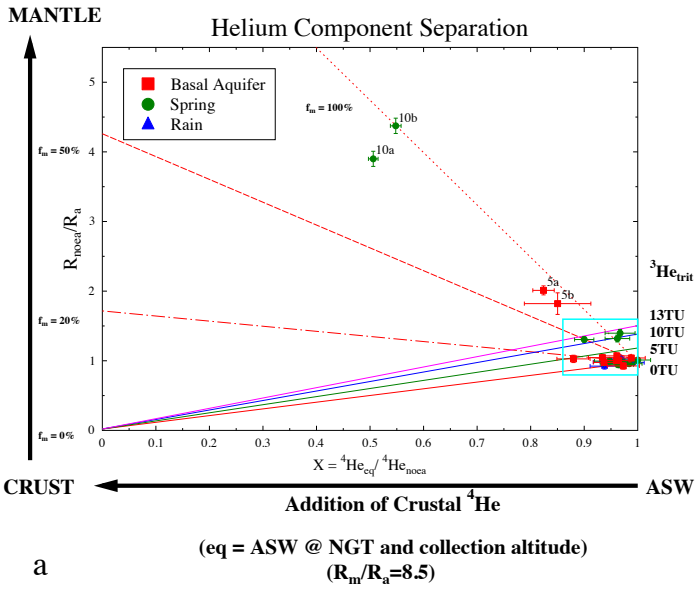

a

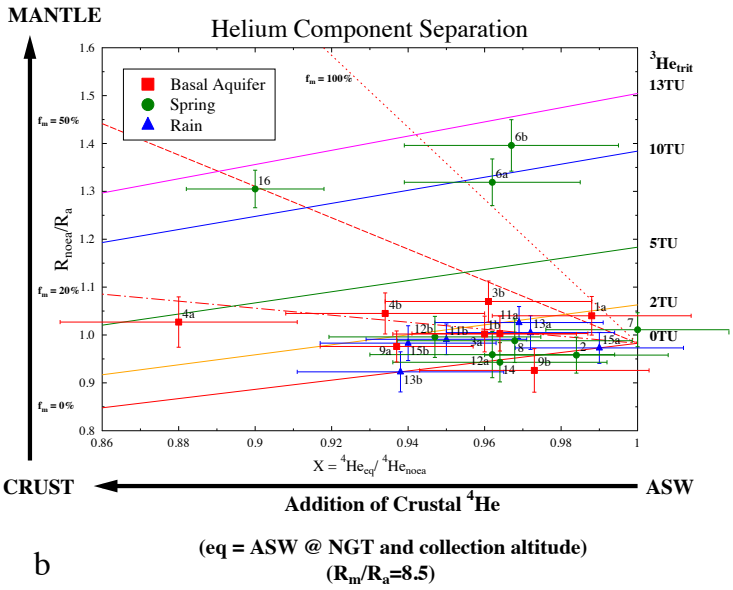

b

Figure B1. R_{noea}/R_a versus $^4He_{eq}/^4He_{noea}$ for (a) all Maui samples; (b) zoomed-in view of the bottom right corner (blue box) of panel (a). R/R_a values for the crust and the mantle are assumed to be 0.02 and 8.5, respectively. Lines corresponding to 0%, 20%, 50%, and 100% mantle helium and 0 TU, 2 TU, 5 TU, 10 TU, and 13 TU tritiogenic ^3He are shown. The He_{eq} and He_{ea} components are estimated in an NGT model following Ballentine and Hall [1999].

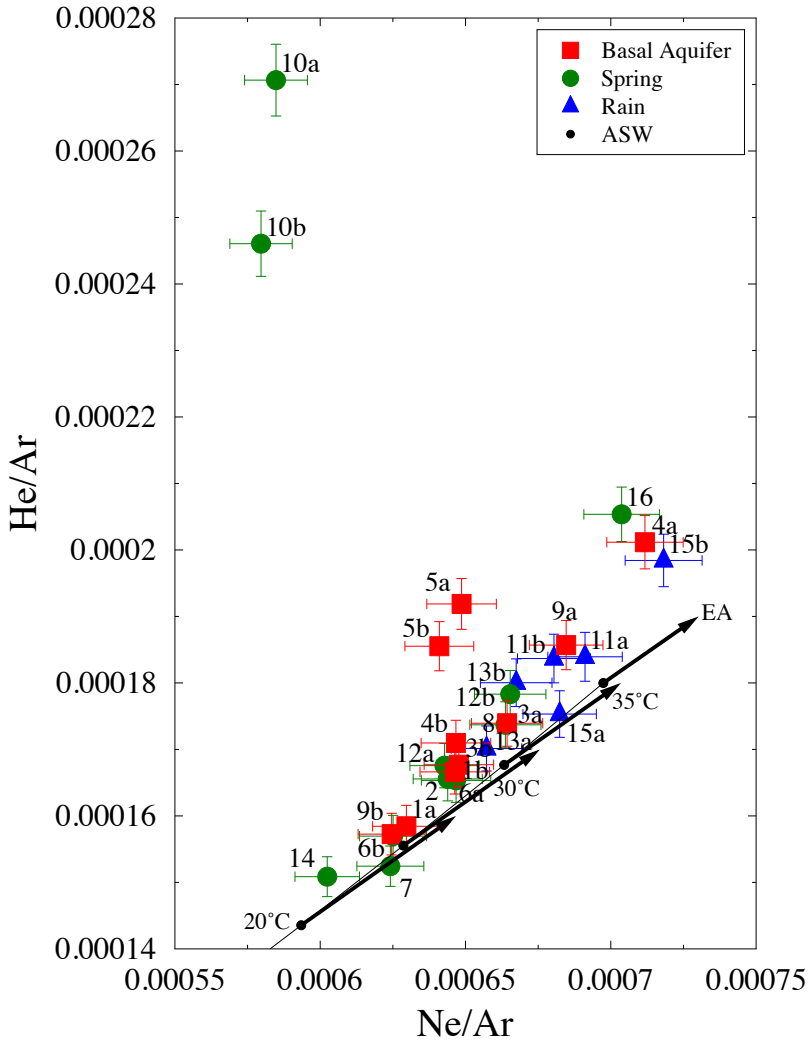

Figure B2. Comparison of measured He/Ar versus Ne/Ar for all Maui samples with theoretical ASW values between 20°C and 35°C. EA addition moves samples in the direction indicated by arrows originating from expected ASW values.

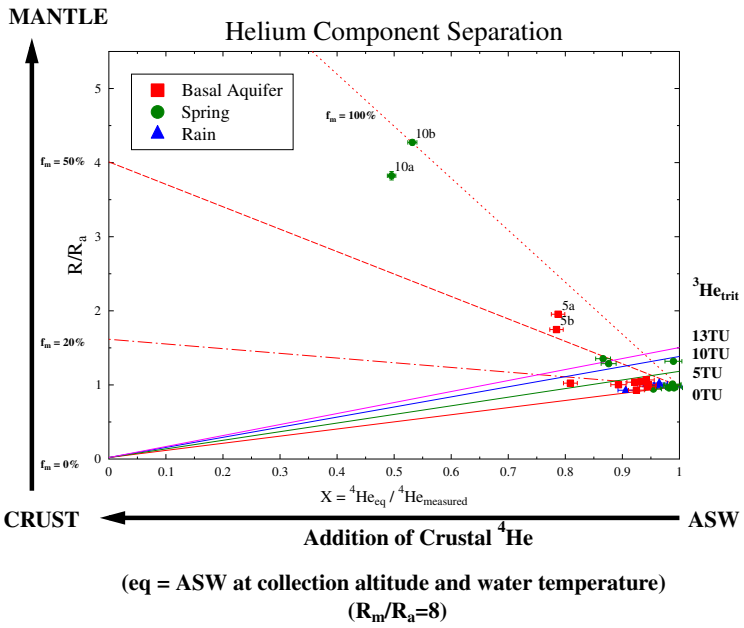

Figure B3. R/R_a versus $^4He_{eq}/^4He_s$ for all Maui samples. R/R_a values for the crust and the mantle are assumed to be 0.02 and 8, respectively. The He_{eq} component is estimated based on collection altitude and water temperature, and EA is assumed to be 0.

APPENDIX C

Supplementary materials for Chapter 5

C1. He component separation

The separation and quantification of different He components, i.e., atmospheric, crustal and/or mantle, under certain assumptions, allows for the characterizations of the crustal and mantle He sources. This analysis is typically done by plotting R_{noea}/R_a versus $^4He_{eq}/^4He_{noea}$ [e.g., Weise and Moser, 1987; Stute et al., 1992; Castro, 2004]. We specify

$$He_{noea} = He_s - He_{ea}, \quad (C1)$$

$$He_{exc} = He_s - He_{eq} - He_{ea}, \quad (C2)$$

where He_s is measured total He concentration, He_{eq} and He_{ea} are the ASW and EA components, respectively, He_{noea} is the He concentration excluding EA component and He_{exc} is the measured He concentration without both the ASW and EA He components. He_{ea} is estimated following Eq. C3 [Kipfer et al., 2002]:

$$He_{ea} = (He/Ne)_{atm} * (Ne_s - Ne_{eq}), \quad (C3)$$

where Ne_s is measured total Ne concentration and Ne_{eq} is the ASW component at collection altitude and water temperature. $(He/Ne)_{atm}$ is the ratio of He and Ne in the atmosphere and is equal to 0.2882 ± 0.0028 [Ozima and Pososek, 2002]. Samples with Ne concentrations lower than the ASW values at collection points are assumed to have no EA components. Concentrations of ^3He are given by $^3He_s = {}^4He_s * R$, $^3He_{eq} = {}^4He_{eq} * R_{eq}$, and $^3He_{ea} = {}^4He_{ea} * R_a$, where $R_{eq} = (1.360 \pm 0.006) * 10^{-6}$ [Benson and Krause, 1980] and R are the $^3He/^4He$ ratios for ASW and total measured He, respectively. In addition, we specify [Castro, 2004]:

$$R_{noea} = \frac{^3He_{noea}}{^4He_{noea}} \quad (C4)$$

and

$$R_{exc} = \frac{^3He_{exc}}{^4He_{exc}}. \quad (C5)$$

where R_{noea} and R_{exc} are the $^3He/^4He$ ratio without the EA component and that without both the ASW and EA components, respectively. Additional details and applications of EA estimation and He component separation can be found in Saar et al. [2005] and Niu et al. [2015; 2017a; 2017b].

The R_{exc}/R_a estimates (Table 5.1) are under the assumption that all of the water from springs and basal aquifer are very recent, so they contain no tritiogenic ^3He. Most samples, i.e., those from basal aquifer sampling sites 5, 6, 7, 8, spring sites 1, 2, 11, 13, 14, 16, 17, and all rainwater samples, yield either negative R_{exc}/R_a ratios or values approximately equal to 1 within 1σ error, as a result of the negative estimated He excesses or the minimal He excesses. With the relatively large errors on R_{exc}/R_a or negative estimates, the He excesses in these samples are considered to be of atmospheric origin.

Samples 9a, 9b, 10a, and 10b, from the two adjacent wells in Keanae, display R_{exc}/R_a ratios between 7.3 ± 0.7 and 10.1 ± 1.2, nearly identical to that of pure MORB-type mantle He ($R/R_a = 7 – 9$) [Farley and Neroda, 1998], and close to the R_{exc}/R_a estimates of the water samples collected in 2014 (6.4 ± 0.6 and 5.8 ± 0.6) from one of these two wells [Niu et al., 2017b]. It is relevant to note that the ASW and EA He components, and thus R_{exc}/R_a ratios, were estimated following Ballentine and Hall [1999] in our first study, and R_{exc}/R_a estimates obtained in Niu et al. [2017b] were 6.8 ± 1.0 and 6.6 ± 3.2 for these two samples, respectively, near identical to the estimates obtained here by estimating the EA He component based on Ne excess following Kipfer et al. [2002]. Sample 15a and 15b have R_{exc}/R_a values of 7.2 ± 1.4 and 5.5 ± 1.1, close to the R_{exc}/R_a ratio of the sample collected in 2014 (4.2 ± 0.9). As discussed in Niu et al. [2017b], the ratio of 4.2 ± 0.9 may have been underestimated by the model in Ballentine and Hall [1999] because of the exceptionally low Ar, Kr, and Xe concentrations of the sample. Samples 12a and 12b, from Ohio spring, yield measured R/R_a (1.17 ± 0.02 for both samples) and estimated R_{exc}/R_a (17 ± 23 and 6.2 ± 2.8) similar to those collected in 2014, with R/R_a values being1.29 ± 0.02 and 1.35 ± 0.01 and R_{exc}/R_a being 7.0 ± 2.2 and 14 ± 8, respectively, following Kipfer et al. [2002]. The R_{exc}/R_a estimates, following Ballentine and Hall [1999], reported in Niu et al. [2017b], are very close to these, being 9.9 ± 6.3 and 14 ± 12, respectively. The big errors are a result of the small amount of terrigenic He compared to the atmospheric He sources.

Figure C1 shows a plot of R_{noea}/R_a versus $^4He_{eq}/^4He_{noea}$ for all spring and basal samples from both sampling seasons. Colored solid lines indicate the expected position for samples with

tritiogenic ^{3}He levels varying from 0 to 20 TU and 0% mantle contribution while red dashed and/or dotted lines indicate mantle contributions ranging from 20% to 100% and tritiogenic ^{3}He level of 0 TU. The lines are calculated based on

$$R_{noea}/R_a = \frac{^4He_{eq}R_{eq} + {}^4He_{exc}R_{exc} + {}^3He_{trit}}{^4He_{noea}R_a} \quad \text{(C6)}$$

and rearranged to

$$R_{noea}/R_a = (kx + R_{exc}) / R_a \quad \text{(C7)}$$

where,

$$k = R_{eq} - R_{exc} + {}^3He_{trit} / {}^4He_{eq}, \quad \text{(C8)}$$

$$x = {}^4He_{eq} / {}^4He_{noea}, \quad \text{(C9)}$$

and

$$R_{exc} = f_m R_m + (1- f_m)R_c. \quad \text{(C10)}$$

The term f_m, indicated near the red lines, corresponds to the fraction of the mantle contribution and $(1-f_m)$ is the crustal fraction of the terrigenic end-member. R_c is the crustal end-member of ^{3}He/^{4}He ratio and is assumed to be 0.02 [O'Nions and Oxburgh, 1983], and R_m is the mantle end-member of ^{3}He/^{4}He ratio. Mantle R/R_a (R_m/R_a) values in Mid Ocean Ridge Basalts (MORB) and Ocean Island Basalts (OIB) are ~ 8 and 50, respectively [Graham, 2002; Starkey et al., 2009]. Different R_m/R_a values were assigned in order to find the appropriate value that makes the green line representing mixing between ASW and pure mantle component to plot in the vicinity of sample 10a. The x coordinate indicates the He fraction contributed by ASW. The fraction of terrigenic end-member is (1-x). In this graphic, a sample displaying a value of 1 on the horizontal axis points to a component of purely atmospheric origin, while a value approaching 0 points to a solely terrigenic origin. Increasing values on the left vertical axis denote increasing mantle contributions, while increasing values on the right vertical axis reflect increasing tritiogenic ^{3}He levels (in TU; 1 TU is equivalent to ~2.5 * 10^{-15} cm^3 of ^{3}He per gram of water). Samples plotting along a particular mixing line represent varying contributions of these components.

Most samples plot near the right-axis and are thus dominated by an atmospheric component. Samples 9a, 9b, 10a, and 10b exhibit significant mantle He components, similar to the samples collected at the same site in 2014. In fractured systems like Maui, infiltration is very rapid. Therefore, the accumulation of radiogenic ^{4}He produced in the basaltic bedrock is likely minimal. Consequently, if a sample with a significant terrigenic He source plots on a line representing a mixture of atmospheric and a pure mantle source with no crustal He, the ^{3}He/^{4}He

ratio in the mantle end-member can be estimated from the slope of the line. From Figure C1, it is apparent that when R_m/R_a is assumed to be 10, samples 9a, 9b, 10a, and 10b plot on or close to the line, representing a mantle component very close to a MORB source ($R/R_a = 7 – 9$) [Farley and Neroda, 1998]. Assuming that a crustal component is negligible, 10 represents the mantle end-member in this area, close to the estimate of 8.5 in the first sampling campaign. According to Kurz et al. [1987], R/R_a values of the Hanā Basalt are indeed about 8, indistinguishable from that of MORB.

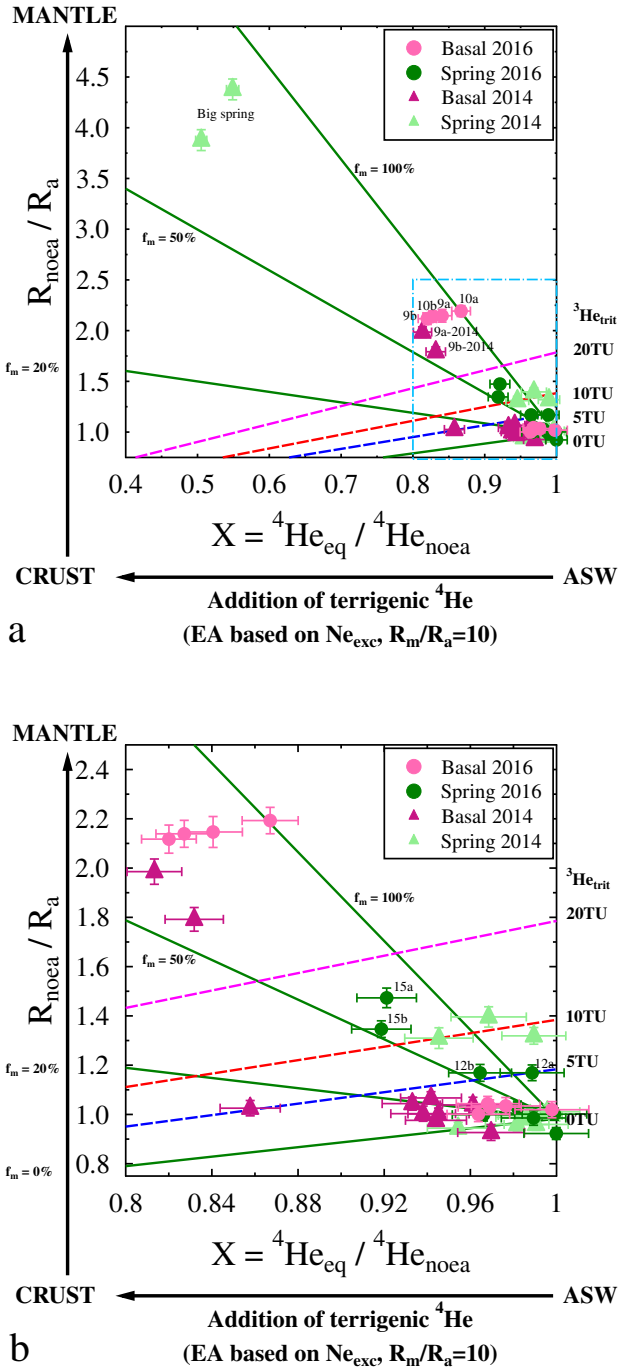

Figure C1. R_{noea}/R_a versus $^4He_{eq}/^4He_{noea}$ for all spring and basal samples from both years; panel (b) is zoomed-in view of the bottom right corner (blue box) of panel (a). R/R_a values for the crust and the mantle are assumed to be 0.02 and 10, respectively. Lines corresponding to 0%, 20%, 50%, and 100% mantle helium and 0 TU, 5 TU, 10 TU, and 20 TU tritiogenic ^{3}He are shown. Labels with "-2014" are for samples from 2014. The Big spring was only sampled in 2014 but not in 2016. Site numbers are those in the 2016 sampling campaign (cf., Table 5.1).

REFERENCES

Aeschbach-Hertig, W., and Solomon, D. K. (2013). Noble gas thermometry in groundwater hydrology, in *The Noble Gases as Geochemical Tracers, Adv. Isotope Geochem.*, edited by P. Burnard, pp. 81–122, Springer, Berlin.

Aeschbach-Hertig, W., Stute, M., Clark, J. F., Reuter, R. F., and Schlosser, P. (2002). A paleotemperature record derived from dissolved noble gases in groundwater of the Aquia Aquifer (Maryland, USA). *Geochim. Cosmochim. Acta*, *66*(5), 797–817.

Alberta Climate Information Service. On November 13, 2015. Retrieved from http://agriculture.alberta.ca/acis/alberta-weather-data-viewer.jsp.

Andrews, J. N. (1985). The isotopic composition of radiogenic helium and its use to study groundwater movement in confined aquifers. *Chem. Geol.*, *49*(1), 339–351.

Andrews, J. N., and Lee, D. J. (1979). Inert gases in groundwater from the Bunter Sandstone of England as indicators of age and palaeoclimatic trends. *J. Hydrol.*, *41*(3-4), 233–252.

Arendt, C. A. (2015). *The Hydrologic Evolution of Glacial Meltwater: Insights and Implications from Alpine and Arctic Glaciers*. Doctoral dissertation, University of Michigan, Ann Arbor, MI, USA. Retrieved from. https://deepblue.lib.umich. edu/bitstream/handle/2027.42/113348/carliana_1.pdf.

Arendt, C. A., Aciego, S. M., Hetland, E. (2015). An open source Bayesian Monte Carlo isotope mixing model with applications in earth surface processes. *Geochem., Geophys., Geosystems, 15*, doi:10.1002/2014GC005683.

Ballentine, C. J., and Hall, C. M. (1999). Determining paleotemperature and other variables by using an error-weighted, nonlinear inversion of noble gas concentrations in water. *Geochim. Cosmochim. Acta*, *63*(16), 2315–2336.

Ballentine, C. J., O'Nions, R. K., Oxburgh, E. R., Horvath, F., and Deak, J. (1991). Rare gas constraints on hydrocarbon accumulation, crustal degassing and groundwater flow in the Pannonian Basin. *Earth Planet. Sci. Lett.*, *105*(1–3), 229–246.

Barnes, M., Miura, T., and Giambelluca, T. W. (2016). An assessment of diurnal and seasonal cloud cover changes over the Hawaiian Islands using Terra and Aqua MODIS. *J. Clim.*, *77*(1), 77–90.

Barnett, T. P., Adam, J. C., and Lettenmaier, D. P. (2005). Potential impacts of a warming climate on water availability in snow-dominated regions. *Nature*, *438*(7066), 303–309.

Baadsgaard, H. (1973). U-Th-Pb dates on zircons from the early Precambrian Amîtsoq gneisses, Godthaab district, West Greenland. *Earth Planet. Sci. Lett.*, *19*(1), 22–28.

Bamber, J. (2001). *Greenland 5 km DEM, Ice Thickness, and Bedrock Elevation Grids*. NASA Nat. Snow and Ice Data Center Distrib. Active Archive Center, Boulder, Colo.

Benson, B. B., and Krause D. Jr. (1976). Empirical laws for dilute aqueous solutions of nonpolar gases. *J. Chem. Phys.*, *64*(2), 689–709.

Benson, B. B., and Krause, D., Jr. (1980). Isotopic fractionation of helium during solution: a probe for the liquid state. *J. Solut. Chem.*, *9*(12), 895–909.

Bergin, M. H., Jaffrezo, J. L., Davidson, C. I., Caldow, R., and Dibb, J. (1994). Fluxes of chemical species to the Greenland ice sheet at Summit by fog and dry deposition. *Geochim. Cosmochim. Acta*, *58*(15), 3207–3215.

Bergmanis, E. C., Sinton, J. M., and Trusdell, F. A. (2000). Rejuvenated volcanism along the southwest rift zone, East Maui. Hawai‘i, *Bull. Volcanol.*, *62*(4–5), 239–255.

Blumenstock, D. I., and Price, S. (1967). *Climates of the States: Hawaii: Climate of Hawaii*, Environ. Data Serv., U.S. Gov. Print. Off., Washington, D. C.

Brown, L. E., Hannah, D. M., and Milner, A. M. (2007). Vulnerability of alpine stream biodiversity to shrinking glaciers and snowpacks. *Glob. Change Biol.*, *13*(5), 958–966.

Burnard, P. ed. (2013). *The Noble Gases as Geochemical Tracers* (p. 391). New York: Springer.

Cameron, E. M., and Garrels, R. M. (1980). Geochemical compositions of some Precambrian shales from the Canadian Shield. *Chem. Geol.*, *28*, 181–197.

Carey, A. E., and Dowling, C. B., and Poreda, R. J. (2004). Alabama Gulf Coast groundwaters: ^{4}He and ^{14}C as groundwater-dating tools. *Geology*, *32*(4), 289–292.

Castro, M. C. (2004). Helium sources in passive margin aquifers — New evidence for a significant mantle ^{3}He source in aquifers with unexpectedly low in situ ^{3}He/^{4}He production. *Earth Planet. Sci. Lett.*, *222*(3), 897–913.

Castro, M. C., and Goblet, P. (2003). Calibration of regional groundwater flow models—Working toward a better understanding of sitespecific systems.*Water Resour. Res.*, *39*(6), 1172, doi:10.1029/2002WR001653.

Castro, M. C., Jambon, A., Marsily, G., and Schlosser, P. (1998a). Noble gases as natural tracers of water circulation in the Paris Basin: 1. Measurements and discussion of their origin and mechanisms of vertical transport in the basin. *Water Resour. Res.*, *34*(10), 2443–2466, doi: 10.1029/98WR01956.

Castro, M. C., Goblet, P., Ledoux, E., Violette, S., and Marsily G. (1998b). Noble gases as natural tracers of water circulation in the Paris Basin: 2. Calibration of a groundwater flow model using noble gas isotope data. *Water Resour. Res.*, *34*(10), 2467–2483, doi:10.1029/98WR01957.

Castro, M. C., Stute, M., and Schlosser, P. (2000). Comparison of ^{4}He ages and ^{14}C ages in simple aquifer systems: Implications for groundwater flow and chronologies. *Appl. Geochem.*, *15*(8), 1137–1167.

Castro, M. C., Hall, C. M., Patriarche, D., Goblet, P., and Ellis, B. R. (2007). A new noble gas paleoclimate record in Texas—Basic assumptions revisited. *Earth Planet. Sci. Lett.*, *257*(1), 170–187.

Castro, M. C., Ma, L., and Hall, C. M. (2009). A primordial, solar He–Ne signature in crustal fluids of a stable continental region. *Earth Planet. Sci. Lett.*, *279*(3), 174–184.

Castro, M. C., Warrier, R. B., Hall, C. M., and Lohmann, K. C. (2012). A late Pleistocene–Mid-Holocene noble gas and stable isotope climate and subglacial record in southern Michigan. *Geophys. Res. Lett.*, *39*, L19709, doi:10.1029/2012GL053098.

Chen, C. Y., Frey, F. A., Garcia, M. O., Dalrymple, G. B., and Hart S. R. (1991) The tholeiite to alkalic basalt transition at Haleakala Volcano, Maui, Hawai‘i. *Contrib. Mineral. Petrol.*, *106*(2), 183–200.

Chevallier, P., Pouyaud, B., Suarez, W., and Condom, T. (2011). Climate change threats to environment in the tropical Andes: glaciers and water resources. *Reg. Environ. Change*, *11*(1), 179–187.

Chu, P. S., Nash, A. J., and Porter, F. Y. (1993). Diagnostic studies of two contrasting rainfall episodes in Hawaii: Dry 1981 and wet 1982. *J. Clim.*, *6*, 1457–1462.

Chylek, P., Dubey, M. K., and Lesins, G. (2006). Greenland warming of 1920–1930 and 1995–2005. *Water Resour. Res.*, *33*, L11707, doi:10.1029/ 2006GL026510.

Clark, I. D., and Fritz, P. (1997). Environmental Isotopes in Hydrogeology. CRC press.

Clark, I. D., Fritz, P., Quinn, O. P., Rippon, P. W., Nash, H., and al Said, S. B. (1987). Modern and fossil groundwater in an arid environment: a look at the hydrogeology of southern Oman. *Isotope Techniques in Water Resources Development*. Int. At. Energy Agency Symposium, March 1987, Vienna, 167–187.

Clarke, W. B., Jenkins, W. J., and Top, Z. (1976). Determination of tritium by mass spectrometric measurement of ^{3}He. *Int. J. Appl. Radiat. Isot.*, *27*(9), 515–522.

Craig, H. (1961). Isotopic variations in meteoric waters. *Science*, *133*(3465), 1702–1703.

Craig, H., and Lal, D. (1961). The production rate of natural tritium. *Tellus*, *13*(1), 85–105.

Craig, H., and Wiens, R. C. (1996). Gravitational enrichment of $^{84}Kr/^{36}Ar$ ratios in polar ice caps: A measure of firn thickness and accumulation temperature. *Science*, *271*(5256), 1708–1710.

Croff, A. G., Lomenick, T. F., Lowrie, R. S., and Stow, S. H. (2003). *Evaluation of Five Sedimentary Rocks Other than Salt for Geologic Repository Siting Purposes* (No. ORNL/TM-2003/256/V1). Oak Ridge National Laboratory (ORNL), Oak Ridge, TN.

Crowley, J. L., and Parrish, R. R. (1999). U-Pb isotopic constraints on diachronous meta-morphism in the northern Monashee complex, southern Canadian Cordillera. *J. Metamorph. Geol.*, *17*, 483–502.

Cuffey, K. M., and Paterson, W. S. B. (2010). *The Physics of Glaciers*, Academic, Amsterdam.

Dansgaard, W. (1964). Stable isotopes in precipitation. *Tellus*, *16*(4), 436–468.

Das, S. B., Joughin, I., Behn, M. D., Howat, I. M., King, M. A., Lizarralde, D., and Bhatia, M. P. (2008). Fracture propagation to the base of the Greenland ice sheet during supraglacial lake drainage. *Science*, *320*(5877), 778–781.

Dawes, P. R. (2009). The bedrock geology under the Inland Ice: The next major challenge for Greenland mapping. *Geol. Surv. Denmark and Greenland Bull.*, *17*, 57–60.

de Marsily, G., Goncalves, J., Violette, S., and Castro, M. C. (2002) From nuclear fuels to waste: Current Research; Migration mechanisms of radionuclides from a clay repository toward adjacent aquifers and the surface. *C. R. Phys.*, *3*, 945–959.

Domenico, P. A., and Schwartz, F. W. (1998). *Physical and chemical hydrogeology* (Vol. 44). New York: Wiley.

Dowling, C. B., Poreda, R. J., and Lyons, W. B. (2014). The effects of high meltwater on the limnology of Lake Fryxell and Lake Hoare, Taylor Valley, Antarctica, as shown by dissolved gas, tritium and chlorofluorocarbons. *Antarct. Sci.*, *26*(04), 331–340.

Evans, S. G., and Clague, J. J. (1994). Recent climatic change and catastrophic geomorphic processes in mountain environments. *Geomorphology*, *10*(1), 107–128.

Farley, K. A., and Neroda, E. (1998). Noble gases in the earth's mantle. *Annual Rev. Earth Planet. Sci.*, *26*(1), 189-218.

Fercho, S., Owens, L., Walsh, P., Drakos, P., Martini, B., Lewicki, J. L., and Kennedy, B. M. (2015). Blind geothermal system exploration in active volcanic environments; multi-phase geophysical and geochemical surveys in overt and subtle volcanic systems, Hawai'i and Maui, *Tech. Rep. DE-EE0002837*, U.S. Department of Energy – Geothermal Technologies Program, Washington, D. C.

Fiorella, R. P., Poulsen, C. J., Zolá, R. S. P., Jeffery, M. L., and Ehlers, T. A. (2015). Modern and long-term evaporation of central Andes surface waters suggests paleo archives underestimate Neogene elevations. *Earth Planet. Sci. Lett.*, *432*, 59–72.

Friend, C. R., and Nutman, A. P. (2005). New pieces to the Archaean terrane jigsaw puzzle in the Nuuk region, southern West Greenland: Steps in transforming a simple insight into a complex regional tectonothermal model. *J. Geol. Soc.*, *162*(1), 147–162.

Galewsky, J., Strong, M., and Sharp, Z. D. (2007). Measurements of water vapor D/H ratios from Mauna Kea, Hawaii, and implications for subtropical humidity dynamics, *Geophys. Res. Lett.*, *34*, L22808, doi:10.1029/2007GL031330.

Gardner, W. P., Susong, D. D., Solomon, D. K., and Heasler, H. P. (2010). Using noble gases measured in spring discharge to trace hydrothermal processes in the Norris Geyser Basin, Yellowstone National Park, U.S.A. *J. Volcanol. Geotherm. Res.*, *198*, 394–404.

Garza, J. A., Chu, P. S., Norton, C. W., and Schroeder, T. A. (2012). Changes of the prevailing trade winds over the islands of Hawaii and the North Pacific. *J. Geophys. Res.*, *117*, D11109, doi:10.1029/2011JD016888.

Giambelluca, T. W., and Nullet, D. (1991). Influence of the trade-wind inversion on the climate of a leeward mountain slope in Hawaii. *Clim. Res.*, *1*(3), 207–216.

Giambelluca, T. W., and Schroeder, T. A. (1998). Climate, in *Atlas of Hawaii*, 3rd ed., edited by S. P. Juvik and J. O. Juvik, pp. 49–59, Univ. of Hawai‘i Press, Honolulu, HI.

Giambelluca, T. W., DeLay, J. K., Nullet, M. A., Scholl, M. A., and Gingerich, S. B. (2011). Canopy water balance of windward and leeward Hawaiian cloud forests on Haleakal a, Maui, Hawai’i. *Hydrol. Process.*, *25*(3), 438–447.

Gibson, H. D., Brown, R. L., and Carr, S. D. (2005). U–Th–Pb geochronologic constraints on the structural evolution of the Selkirk fan, northern Selkirk Mountains, southern Canadian Cordillera. *J. Struct. Geol.*, *27*(10), 1899–1924.

Gingerich, S. B. (1999a). Ground-water occurrence and contribution to streamflow, Northeast Maui, Hawaii, *U.S. Geol. Surv. Water-Resour. Invest. Rep. 99-4090*, 69 pp., USGS, Pacific Islands Water Science Center, Honolulu, HI.

Gingerich, S. B. (1999b). Ground water and surface water in the Haiku area, East Maui, Hawaii. *U.S. Geol. Surv. Water-Resour. Invest. Rep. 98- 4142*, 38 pp., USGS, Pacific Islands Water Science Center. Honolulu, HI.

Gingerich, S. B. (2005). Median and low-flow characteristics for streams under natural and diverted conditions, Northeast Maui, Hawaii. *U.S. Geol. Surv. Sci. Investig. Rep. 2004-5262*. US Geological Survey, Reston, Virginia.

Hall, C. M., Castro, M. C., Lohmann, K. C., and Sun, T. (2012). Testing the noble gas paleothermometer with a yearlong study of groundwater noble gases in an instrumented

monitoring well. *Water Resour. Res.*, *48*, W04517, doi:10.1029/2011WR010951.

Hall, C. M., Castro, M. C., Kenig, F., and Doran, P. T. (2017). Constraining the recent history of the perennially ice-covered Lake Bonney, East Antarctica using He, Kr and Xe concentrations. *Geochim. Cosmochim. Acta*, *209*, 233–253.

Hanna, E., and Cappelen, J. (2003). Recent cooling in coastal southern Greenland and relation with the North Atlantic Oscillation. *Geophys. Res. Lett.*, *30*(3), 1132, doi:10.1029/2002GL015797.

Hanna, E., Mernild, S. H., Cappelen, J., and Steffen, K. (2012). Recent warming in Greenland in a long-term instrumental (1881–2012) climatic context: I. Evaluation of surface air temperature records. *Environ. Res. Lett.*, *7*(4), 045404.

Harris, G. N., Jr., Bowman, K. P., and Shin, D. B. (2000). Comparison of freezing-level altitudes from the NCEP reanalysis with TRMM precipitation radar brightband data. *J. Clim.*, *13*(23), 4137–4148.

Hart, J. K. (2006). Athabasca Glacier, Canada — a field example of subglacial ice and till erosion? Earth Surf. Process. *Landforms*, *31*(1), 65–80.

Heaton, T. H. E., and Vogel, J. C. (1981). "Excess air" in groundwater. *J. Hydrol.*, *50*, 201–216.

Heilweil, V. M., Solomon, D. K., Gingerich, S. B., and Verstraeten, I. M. (2009). Oxygen, hydrogen, and helium isotopes for investigating groundwater systems of the Cape Verde Islands, West Africa. *Hydrogeol. J.*, *17*, 1157–1174.

Heilweil, V. M., Healy, R. W., and Harris, R. N. (2012). Noble gases and coupled heat/fluid flow modeling for evaluating hydrogeologic conditions of volcanic island aquifers. *J. Hydrol.*, *464*, 309–327.

Herzberg, O., and Mazor, E. (1979). Hydrological applications of noble gases and temperature measurements in underground water systems: Examples from Israel. *J. Hydrol.*, *41*, 217–231.

Hildenbrand, A., Marlin, C., Conroy, A., Gillot, P. Y., Filly, A., and Massault, M. (2005). Isotopic approach of rainfall and groundwater circulation in the volcanic structure of Tahiti-Nui (French Polynesia). *J. Hydrol.*, *302*(1), 187–208.

Hohmann, R., Schlosser, P., Jacobs, S., Ludin, A., and Weppernig, R. (2002). Excess helium and neon in the southeast Pacific: Tracers for glacialmeltwater. *J. Geophys. Res.*, *107*(C11), 3198, doi:10.1029/2000JC000378.

Hollis, J. A., Frei, D., van Gool, J. A., Garde, A. A., and Persson, M. (2006). Using zircon geochronology to resolve the Archaean geology of southern West Greenland. *Geol. Surv. Denmark and Greenland Bull.*, *10*, 49–52.

Huang, B., L'Heureux, M., Hu, Z.-Z., and Zhang, H.-M. (2016). Ranking the stron- gest ENSO events while incorporating SST uncertainty. *Geophys. Res. Lett.*, *43*, 9165–9172, doi:10.1002/2016GL070888.

Immerzeel, W. W., van Beek, L. P. H., Bierkens, M. F. P. (2010). Climate change will affect the Asian water towers. *Science*, *328*(5984), 1382–1385.

Intergovernmental Panel on Climate Change (2013). *Climate Change 2013: The Physical Science Basis. Contribution of Working Group I to the Fifth Assessment Report of the Intergovernmental Panel on Climate Change*, edited by T. F. Stocker et al., 1535 pp., Cambridge Univ. Press, Cambridge, U. K., and New York, doi:10.1017/CBO9781107415324.

International Atomic Energy Agency. On October 27, 2015. Retrieved from http://www.univie.ac.at/cartography/project/wiser/.

Jähne, B., Heinz, G., Dietrich, W. (1987). Measurement of the diffusion coefficients of sparingly soluble gases in water. *J. Geophys. Res. Oceans*, *92*(C10), 10767–10776.

James, E. R., Manga, M., Rose, T. P., and Hudson, G. B. (2000). The use of temperature and the isotopes of O, H, C, and noble gases to determine the pattern and spatial extent of groundwater flow. *J. Hydrol.*, *237*, 100–112.

Jean-Baptiste, P., Petit, J. R., Lipenkov, V. Y., Raynaud, D., and Barkov, N. I. (2001). Constraints on hydrothermal processes and water exchange in Lake Vostok from helium isotopes. *Nature*, *411*(6836), 460–462.

Jean-Baptiste, P., Allard, P., Coutinho, R., Ferreira, T., Fourré, E., Queiroz, G., and Gaspar, J. L. (2009). Helium isotopes in hydrothermal volcanic fluids of the Azores archipelago. *Earth Planet. Sci. Lett.*, *281*, 70–80.

Jenkins, W. J. (1987). ^{3}H and ^{3}He in the Beta Triangle: Observations of gyre ventilation and oxygen utilization rates. *J. Phys. Oceanogr.*, *17*(6), 763–783.

Johnston, D. H., Williams, P. F., Brown, R. L., Crowley, J. L., and Carr, S. D. (2000). Northeastward extrusion and extensional exhumation of crystalline rocks of the Monashee complex, southeastern Canadian Cordillera. *J. Struct. Geol.*, *22*(5), 603–625.

Joughin, I., Das, S. B., King, M. A., Smith, B. E., Howat, I. M., and Moon, T. (2008). Seasonal speedup along the western flank of the Greenland Ice Sheet. *Science*, *320*(5877), 781–783.

Kehrwald, N. M., Thompson, L. G., Yao, T., Mosley-Thompson, E., Schotterer, U., Alfimov, V., Davis, M. E., et al., 2008. Mass loss on Himalayan glacier endangers water resources. *Geophys. Res. Lett.*, *35*(22), L22503, doi:10.1029/2008GL035556.

Kelly, J. L., and Glenn, C. R. (2015). Chlorofluorocarbon apparent ages of groundwaters from west Hawaii, USA. *J. Hydrol.*, *527*, 355–366.

Kennedy, K. (1985). *Dikewater relationships to potential geothermal resources on Leeward West Maui, State of Hawaii*. Doctoral dissertation, Univ. of Hawai‘i at Manoa, HI.

Kennedy, B. M., Lynch, M. A., Reynolds, J. H., and Smith, S. P. (1985). Intensive sampling of noble gases in fluids at Yellowstone: I. Early overview of the data; regional patterns. *Geochim. Cosmochim. Acta*, *49*, 1251–1261.

Kennedy, B. M., Reynolds, J. H., and Smith, S. P. (1988). Noble gas geochemistry in thermal springs. *Geochim. Cosmochim. Acta*, *52*, 1919–1928.

Kipfer, R., Aeschbach-Hertig, W., Peeters, F., and Stute, M. (2002) Noble gases in lakes and ground waters. *Rev. Mineral. Geochem.*, *47*(1), 615–700.

Kitayama, K., and Mueller-Dombois, D. (1994). An altitudinal transect analysis on the windward vegetation of Haleakala, a Hawaiian island mountain: (1) Climate and soils. *Phytocoenologia*, *24*, 111–133.

Klint, K. E. S., Engström, J., Parmenter, A., Ruskeeniemi, T., Liljedahl, C., and Lehtinen, A. (2013) Lineament mapping and geological history of the Kangerlussuaq region, southern West Greenland. *Geol. Surv. Denmark and Greenland Bull.*, *28*, 57–60.

Klump, S., Tomonaga, Y., Kienzler, P., Kinzelbach, W., Baumann, T., Imboden, D. M., and Kipfer, R. (2007). Field experiments yield new insights into gas exchange and excess air formation in natural porous media. *Geochim. Cosmochim. Acta*, *71*, 1385–1397.

Klump, S., Cirpka, O. A., Surbeck, H., and Kipfer, R. (2008). Experimental and numerical studies on excess‐air formation in quasi‐saturated porous media. *Water Resour. Res.*, *44*(5), W05402, doi:10.1029/2007WR006280.

Kulongoski, J. T., Hilton, D. R., and Izbicki, J. A. (2003). Helium isotope studies in the Mojave Desert, California: Implications for groundwater chronology and regional seismicity. *Chem. Geol.*, *202*(1), 95–113.

Kulongoski, J. T., Hilton, D. R., and Selaolo, E. T. (2004). Climate variability in the Botswana Kalahari from the late Pleistocene to the present day. *Geophys. Res. Lett.*, *31*(10), L10204, doi:10.1029/2003GL019238.

Kurz, M. D., Garcia, M. O., Frey, F. A., and O'brien, P. A. (1987). Temporal helium isotopic variations within Hawaiian volcanoes: basalts from Mauna Loa and Haleakala. *Geochim. Cosmochim. Acta*, *51*(11), 2905–2914.

Langenheim, V. A. M., and Clague, D. A. (1987). The Hawaiian-Emperor volcanic chain, part II, stratigraphic framework of volcanic rocks of the Hawaiian Islands, Volcanism in Hawaii, U.S. Geol. Surv. Prof. Pap. 1350, edited by in R. W. Decker, T. L. Wright, and P. H. Stauffer, vol. *1*, pp. 55–84, USGS, Hawaiian Volcano Observatory, Hawaii.

Lau, L. K. S., and Mink, J. F. (2006). *Hydrology of the Hawaiian Islands*, Univ. of Hawai‘i Press, Honolulu, HI.

Leventhal, J. S., and Libby, W. F. (1970). Tritium fallout in the Pacific United States. *J. Geophys. Res.*, *75*(36), 7628–7633.

Liotta, M., Favara, R., and Valenza, M. (2006). Isotopic composition of the precipitations in the central Mediterranean: Origin marks and orographic precipitation effects. *J. Geophys. Res.*, *111*, D19302, doi:10.1029/2005JD006818.

Loope, L. L., and Giambelluca, T. W. (1998). Vulnerability of island tropical montane cloud forests to climate change, with special reference to East Maui, Hawaii. In *Potential Impacts of Climate Change on Tropical Forest Ecosystems* (pp. 363-377). Springer Netherlands.

Loose, B., and Jenkins, W. J. (2014). The five stable noble gases are sensitive unambiguous tracers of glacial meltwater. *Geophys. Res. Lett.*, *41*, 2835–2841, doi:10.1002/2013GL058804.

Luckman, B. H., and Crockett, K. J. (1978). Distribution and characteristics of rock glaciers in the southern part of Jasper National Park, Alberta. *Can. J. Earth Sci.*, *15*(4), 540–550.

Ma, L., Castro, M. C., and Hall, C. M. (2004). A late Pleistocene–Holocene noble gas paleotemperature record in southern Michigan. *Geophys. Res. Lett.*, *31*(23), L23204, doi:10.1029/2004GL021766.

Ma, L., Castro, M. C., Hall, C. M., and Walter, L. M. (2005). Cross-formational flow and salinity sources inferred from a combined study of helium concentrations, isotopic ratios, and major elements in the Marshall aquifer, southern Michigan. *Geochem., Geophys., Geosystems*, *6*(10), Q10004, doi:10.1029/2005GC001010.

Ma, L., Castro, M. C., and Hall, C. M. (2009). Atmospheric noble gas signatures in deep Michigan Basin brines as indicators of a past thermal event. *Earth Planet. Sci. Lett.*, *277*, 137–147, doi:10.1016/j.epsl.2008.10.015.

Malone, J. L., Castro, M. C., Hall, C. M., Doran, P. T., Kenig, F., and McKay, C. P. (2010). New insights into the origin and evolution of Lake Vida, McMurdo Dry Valleys, Antarctica—A noble gas study in ice and brines. *Earth Planet. Sci. Lett.*, *289*(1), 112–122.

Manning, A. H., and Solomon, D. K. (2003). Using noble gases to investigate mountain-front recharge. *J. Hydrol.*, *275*, 194–207.

Mark, B. G., Bury, J., McKenzie, J. M., French, A., and Baraer, M. (2010). Climate change and tropical Andean glacier recession: evaluating hydrologic changes and livelihood vulnerability in the Cordillera Blanca. *Peru. Ann. Assoc. Am. Geogr.*, *100*(4), 794–805.

Marrero-Diaz, R., López, D., Perez, N. M., Custodio, E., Sumino, H., Melián, G. V., Sortino, F., et al. (2015). Carbon dioxide and helium dissolved gases in groundwater at central Tenerife Island, Canary Islands: Chemical and isotopic characterization. *Bull. Volcanol.*, *77*(10), 1–18, doi:10.1007/s00445-015-0969-0.

Martinerie, P., Raynaud, D., Etheridge, D. M., Barnola, J. M., and Mazaudier, D. (1992). Physical and climatic parameters which influence the air content in polar ice. *Earth Planet. Sci. Lett.*, *112*(1), 1–13.

Martinerie, P., Lipenkov, V. Y., Raynaud, D., Chappellaz, J., Barkov, N. I., and Lorius, C. (1994). Air content paleo record in the Vostok ice core (Antarctica): A mixed record of climatic and glaciological parameters. *J. Geophys. Res.*, *99*(D5), 10,565–10,576, doi:10.1029/93JD03223.

Marty, B., Meynier, V., Nicolini, E., Griesshaber, E., and Toutain, J. P. (1993). Geochemistry of gas emanations: A case study of the Reunion Hot Spot, Indian Ocean. *Appl. Geochem.*, *8*, 141–152.

Mazor, E. (1972). Paleotemperatures and other hydrological parameters deduced from noble gases dissolved in groundwaters; Jordan Rift Valley, Israel. *Geochim. Cosmochim. Acta*, *36*, 1321–1336.

Mazor, E., and Bosch, A. (1992). Helium as a semi-quantitative tool for groundwater dating in the range of 10^4–10^8 years, in *Isotopes of Noble Gases as Tracers in Environmental Studies*, Rep. STI/PUB/859, pp. 163–178, Int. At. Energy Agency, Vienna. [Available at http://www-pub. iaea.org/books/iaeabooks/3730/Isotopes-of-Noble-Gases-as-Tracers-in-Environmental-Studies.]

Mazor, E., and Wasserburg, G. J. (1965). Helium, neon, argon, krypton and xenon in gas emanations from Yellowstone and Lassen volcanic National Parks. *Geochim. Cosmochim. Acta*, *29*(5), 443–454.

Merlivat, L., and Jouzel, J. (1979). Global climatic interpretation of the Deuterium–Oxygen 18 relationship for precipitation. *J. Geophys. Res. Oceans*, *84*(C8), 5029–5033.

Müller, T., Osenbrueck, K., Strauch, G., Pavetich, S., Al-Mashaikhi, K.-S., Herb, C., Merchel, S., Rugel, G., Aeschbach, W., and Sanford, W. (2016). Use of multiple age tracers to estimate groundwater residence times and long-term recharge rates in arid southern Oman. *Appl. Geochem.*, *74*, 67–83.

National Centers for Environmental Information. On November 13, 2015. National Oceanic and Atmospheric Administration. Retrieved from http://www.ncdc.noaa.gov/cdo-web/datasets/GHCNDMS/stations/GHCND.

Nelson, S. T. (2000a). Sample vial influences on the accuracy and precision of carbon and oxygen isotope ratio analysis in continuous flow mass spectrometric applications. *Rapid Commun. in Mass Spectrom.*, *14(*4), 293–297.

Nelson, S. T. (2000b). A simple, practical methodology for routine VSMOW/SLAP normalization of water samples analyzed by continuous flow methods. *Rapid Commun. in Mass Spectrom.*, *14*(12), 1044–1046.

Nelson, S. T., and Dettman, D. (2001). Improving hydrogen isotope ratio measurements for on-line chromium reduction systems. *Rapid Commun. in Mass Spectrom.*, *15*(23), 2301–2306.

Niu, Y., Castro, M. C., Aciego, S. M., Hall, C. M., Stevenson, E. I., Arendt, C. A., and Das, S. B. (2015). Noble gas signatures in Greenland: Tracing glacial meltwater sources. *Geophys. Res. Lett.*, *42*, 9311–9318, doi:10.1002/2015GL065778.

Niu, Y., Castro, M. C., Hall, C. M., Aciego, S. M., and Arendt, C. A. (2017a). Characterizing glacial meltwater sources in the Athabasca Glacier, Canada, using noble gases as tracers. *Appl. Geochem.*, *76*, 136–147, doi:10.1016/j.apgeochem.2016.11.015.

Niu, Y., Castro, M. C., Hall, C. M., Gingerich, S. B., Scholl, M. A., and Warrier, R. B. (2017b). Noble gas signatures in the Island of Maui, Hawaii: Characterizing groundwater sources in fractured systems. *Water Resour. Res.*, *53*, 3599–3614, doi:10.1002/2016WR020172.

Nullet, D., and Sanderson, M. (1993). Radiation and Energy Balances and Air Temperature. Prevailing Trade Winds: Weather and Climate in Hawaii, pp. 37–55, Univ. of Hawai‘i Press, Honolulu, HI.

O’Nions, R. K., and Oxburgh, E. R. (1983). Heat and helium in the earth. *Nature*, *306*(5942), 429–431.

Ozima, M., and Podosek, F. A. (2002). *Noble Gas Geochemistry*, Cambridge Univ. Press, Cambridge, U. K.

Parker, R. L. (1967). In: Fleischer, M. (Ed.), *Data of Geochemistry*. US Government Printing Office.

Parrish, R. R., Carr, S. D., and Parkinson, D. L. (1988). Eocene extensional tectonics and geochronology of the southern Omineca belt, British Columbia and Washington. *Tectonics*, *7*(2), 181–212.

Patriarche, D., Castro, M. C., and Goblet, P. (2004). Large-scale hydraulic conductivities inferred from three-dimensional groundwater flow and ^{4}He transport modeling in the Carrizo aquifer, Texas. *J. Geophys. Res.*, *109*, B11202, doi:10.1029/2004JB003173.

Pinti, D. L., and van Drom, E. (1998). PALEOTEMP: A Mathematica® program for evaluating paleotemperatures from the concentration of atmosphere-derived noble gases in ground water. *Comput. Geosci.*, *24*(1), 33–41.

Pinti, D. L., Béland-Otis, C., Tremblay, A., Castro, M. C., Hall, C. M., Marcil, J.-S., Lavoie, J.-Y., Lapointe, R. (2011). Fossil brines preserved in the St-Lawrence Lowlands, Quebec, Canada as revealed by their chemistry and noble gas isotopes. *Geochim. Cosmochim. Acta*, *75*(15), 4228–4243, doi:10.1016/ j.gca.2011.05.006.

Pinti, D. L., Castro, M. C., Lopez-Hernandez, A., Han, G., Shouakar-Stash, O., Hall, C. M., and Ramírez-Montes, M. (2017). Fluid circulation and reservoir conditions of the Los Humeros

Geothermal Field (LHGF), Mexico, as revealed by a noble gas survey. *J. Volcanol. Geotherm. Res.*, *333*, 104–115.

Poland, M. P., Takahashi, T. J., and Landowski, C. M. (Eds.) (2014). Characteristics of Hawaiian volcanoes, *U.S. Geol. Surv. Prof. Pap. 1801*, 429 pp., U.S. Geological Survey, Reston, VA, doi:10.3133/pp1801.

Poreda, R. J., Hunt, A. G., Lyons, W. B., and Welch, K. A. (2004). The helium isotopic chemistry of Lake Bonney, Taylor Valley, Antarctica: timing of late Holocene climate change in Antarctica. *Aquat. Geochem.*, *10*(3–4), 353–371.

Rignot, E., Velicogna, I., van den Broeke, M. R., Monaghan, A., and Lenaerts, J. T. M. (2011). Acceleration of the contribution of the Greenland and Antarctic ice sheets to sea level rise. *Geophys. Res. Lett.*, *38*, L05503, doi:10.1029/2011GL046583.

Roether, W. (1967). Estimating the tritium input to groundwater from wine samples: groundwater and direct run-off contribution to central European surface waters. In: ~~Isotopes in Hydrology~~. IAEA, Vienna.

Ross, G. M., and Parrish, R. R. (1991). Detrital zircon geochronology of metasedimentary rocks in the southern Omineca Belt, Canadian Cordillera. *Can. J. Earth Sci.*, *28*(8), 1254–1270.

Rudnick, R. L., and Gao, S. (2005). Composition of the continental crust. In: Rudnick, R.L. (Ed.), *Treatise on Geochemistry*, vol. 3. Elsevier, Boston.

Saar, M. O., Castro, M. C., Hall, C. M., Manga, M., and Rose, T. P. (2005). Quantifying magmatic, crustal, and atmospheric helium contributions to volcanic aquifers using all stable noble gases: Implications for magmatism and groundwater flow. *Geochem., Geophys., Geosyst.*, *6*, Q03008, doi:10.1029/2004GC000828.

Sanderson, M. (Ed.). (1993). *Prevailing Trade Winds: Climate and Weather in Hawaii*. Univ. of Hawai‘i Press, Honolulu, HI.

Schindler, D. W., and Donahue, W. F. (2006). An impending water crisis in Canada's western prairie provinces. *Proc. Natl. Acad. Sci.*, *103*(19), 7210–7216.

Schlosser, P. (1986). Helium: A new tracer in Antarctic oceanography. *Nature*, *321*, 233–235.

Schlosser, P., Stute, M., Dörr, H., Sonntag, C., and Münnich, K. O. (1988). Tritium/^{3}He dating of shallow groundwater. *Earth Planet. Sci. Lett.*, *89*(3), 353–362.

Schlosser, P., Stute, M., Sonntag, C., and Münnich, K. O. (1989). Tritiogenic ^{3}He in shallow groundwater. *Earth Planet. Sci. Lett.*, *94*(3-4), 245–256.

Schlosser, P., Bayer, R., Foldvik, A., Gammelsrød, T., Rohardt, G., and Münnich, K. O. (1990). Oxygen 18 and helium as tracers of ice shelf water and water/ice interaction in the Weddell Sea. *J. Geophys. Res.*, *95*(C3), 3253–3263, doi:10.1029/JC095iC03p03253.

Scholl, M. A., Gingerich, S. B., and Tribble, G. W. (2002). The influence of microclimates and fog on stable isotope signatures used in interpretation of regional hydrology: East Maui, Hawaii. *J. Hydrol.*, *264*, 170–184.

Scholl, M. A., Giambelluca, T. W., Gingerich, S. B., Nullet, M. A., and Loope, L. L. (2007). Cloud water in windward and leeward mountain forests: The stable isotope signature of orographic cloud water. *Water Resour. Res.*, *43*, W12411, doi:10.1029/2007WR006011.

Scholl, M. A., Shanley, J. B., Zegarra, J. P., and Coplen, T. B. (2009). The stable isotope amount effect: New insights from NEXRAD echo tops, Luquillo Mountains, Puerto Rico. *Water Resour. Res.*, *45*, W12407, doi:10.1029/2008WR007515.

Scholl, M., Eugster, W. and Burkard, R. (2011). Understanding the role of fog in forest hydrology: stable isotopes as tools for determining input and partitioning of cloud water in montane forests. *Hydrol. Process.*, *25*(3), 353–366.

Schroeder, T. A. (1993). Climate controls, in *Prevailing Trade Winds, Weather and Climate in Hawaii*, edited by M. Sanderson, pp. 12–36, Univ. of Hawai‘i Press, Honolulu, HI.

Severinghaus, J. P., and Battle, M. O. (2006). Fractionation of gases in polar ice during bubble close-off: New constraints from firn air Ne, Kr and Xe observations. *Earth Planet. Sci. Lett.*, *244*(1), 474–500.

Shade, P. J. (1999). Water budget of East Maui, Hawaii. US Geological Survey Water-Resources Investigations Report 98-4159. 36 pp.

Shepherd, A., and Wingham, D. (2007). Recent sea-level contributions of the Antarctic and Greenland ice sheets. *Science*, *315*(5818), 1529–1532.

Skidmore, M., Anderson, S. P., Sharp, M., Foght, J., and Lanoil, B. D. (2005). Comparison of microbial community compositions of two subglacial environments reveals a possible role for microbes in chemical weathering processes. *Appl. Environ. Microbiol.*, *71*(11), 6986–6997.

Solomon, D. K. (2000). ^{4}He in groundwater. In: Cook, P., Herczeg, A. L. (Eds.), In *Environmental Tracers in Subsurface Hydrology*. Kluwer Academic Publishers, pp. 425–439.

Stearns, H. T., and Macdonald, A. G. (1942). Geology and ground-water resources of the Island of Maui, Hawaii. *Hawaii Div. Hydrogr. Bull.*, *7*, 344 pp.

Stute, M., and Schlosser, P. (1993). Principles and applications of the noble gas paleothermometer. *Clim. Change Cont. Isot. Rec.*, *78*, 89–100. Geophys. Monogr. Ser., edited by P. K. Swart et al., AGU, Washington, D. C.

Stute, M., and Sonntag, C. (1992). Palaeotemperatures derived from noble gases dissolved in groundwater and in relation to soil temperature, in *Isotopes of Noble Gases as Tracers in Environmental Studies*, IAEA Rep., STI/PUB/859, pp. 111–122, Int. At. Energy Agency,

Vienna.

Stute, M., Sonntag, C., Déak, J., Schlosser, P. (1992). Helium in deep circulating groundwater in the Great Hungarian Plain: flow dynamics and crustal and mantle helium fluxes. *Geochim. Cosmochim. Acta*, *56*(5), 2051–2067.

Sun, T., Hall, C. M., and Castro, M. C. (2010). Statistical properties of groundwater noble gas paleoclimate models: Are they robust and unbiased estimators?. *Geochem., Geophys., Geosyst.*, *11*, Q02002, doi:10.1029/2009GC0027.

Sültenfuß, J., Roether, W, and Rhein, M. (2009). The Bremen mass spectrometric facility for the measurement of helium isotopes, neon, and tritium in water. *Isot. in Environ. Health Stud.*, *45*(2), 83–95, doi: 10.1080/10256010902871929.

Swarzenski, P. W., Dulai, H., Kroeger, K. D., Smith, C. G., Dimova, N., Storlazzi, C. D., Glenn, C. R., et al. (2017). Observations of nearshore groundwater discharge: Kahekili Beach Park submarine springs, Maui, Hawaii. *J. Hydrol.: Reg. Stud.*, *11*, 147–165.

Swennen, R., Vandeginste, V., and Ellam, R. (2003). Genesis of zebra dolomites (Cathedral formation: Canadian Cordillera fold and Thrust belt, British Columbia). *J. Geochem. Explor.*, *78*, 571–577.

Tennant, C., and Menounos, B. (2013). Glacier change of the Columbia icefield, Canadian Rocky Mountains, 1919–2009. *J. Glaciol.*, *59*(216), 671–686.

Thoma, M. J., McNamara, J. P., Gribb, M. M., and Benner, S. G. (2011). Seasonal recharge components in an urban/agricultural mountain front aquifer system using noble gas thermometry. *J. Hydrol*., *409*(1), 118–127.

Thomas, D. M. (1989), Hydrothermal systems in Hawaii, in *The Geology of North America Volume N, The Eastern Pacific Ocean and Hawaii*, edited by E. L. Winterer, D. M. Hussong, and R. W. Decker, pp. 271–277, Geol. Soc. Am., Denver, Colo., doi:hdl.handle.net/10524/47079.

Thomas, D. M., Pierce, H. A., Lautze, N. (2017). Integrated geophysical and drilling results for Mauna Kea volcano hydrologic implications. *Geol. Soc. Am. Abstr. Programs*. *49*(6). doi: 10.1130/abs/2017AM-308419.

Top, Z., Martin, S., and Becker, P. (1988). A laboratory study of dissolved noble gas anomaly due to ice formation. *Geophys. Res. Lett.*, *15*(8), 796–799, doi:10.1029/GL015i008p00796.

Torgersen, T., and Ivey, G. N. (1985). Helium accumulation in groundwater. II: a model for the accumulation of the crustal ^{4}He degassing flux. *Geochim. Cosmochim. Acta*, *49*(11), 2445–2452.

Torgersen, T., Kennedy, B. M., Hiyagon, H., Chiou, K. Y., Reynolds, J. H., and Clarke, W. B. (1989). Argon accumulation and the crustal degassing flux of ^{40}Ar in the Great Artesian Basin, Australia. *Earth Planet. Sci. Lett.*, *92*(1), 43-56.

Unterweger, M. P., Coursey, B. M., Schima, F. J., and Mann, W. B. (1980). Preparation and calibration of the 1978 National Bureau of Standards tritiated-water standards. *Int. J. Appl. Radiat. Isot.*, *31*(10), 611–614.

Vinther, B. M., Andersen, K. K., Jones, P. D., Briffa, K. R., and Cappelen, J. (2006). Extending Greenland temperature records into the late eighteenth century. *J. Geophys. Res.*, *111*, D11105, doi:10.1029/2005JD006810.

Wallace, J. M., and Hobbs, P. V. (2006). *Atmospheric Science: An Introductory Survey*, vol. 92, Elsevier Academic Press, Amsterdam, Netherlands.

Wallsgrove, R., and Penn, D. (2012). *Water Resources and Climate Change Adaptation in Hawai'i: Adaptive Tools in the Current Law and Policy Framework*, Univ. of Hawai'i, Cent. for Island Adaptation and Policy, Honolulu, HI.

Warrier, R. B., Castro, M. C., and Hall, C. M. (2012). Recharge and source-water insights from the Galapagos Islands using noble gases and stable isotopes. *Water Resour. Res.*, *48*, W03508, doi:10.1029/2011WR010954.

Warrier, R. B., Castro, M. C., Hall, C. M., and Lohmann, K. C. (2013). Noble gas composition in rainwater and associated weather patterns. *Geophys. Res. Lett.*, *40*, 3248–3252, doi:10.1002/grl.50610.

Warrier, R. B., Castro, M. C., Hall, C. M., Kenig, F., and Doran, P. T. (2015). Reconstructing the evolution of Lake Bonney, Antarctica using dissolved noble gas. *Appl. Geochem.*, *58*, 46–61, doi:10.1016/j.apgeochem.2015.02.013.

Weise, S. M. (1986). *Heliumisotopen-Gehalte im Grundwasser, Messung und Interpretation*. Doctoral dissertation. Universität München, München, Germany.

Weise, S. M., and Moser, H. (1987). Groundwater dating with helium isotopes. In: *Techniques in Water Resources Development*. IAEA, Vienna, pp. 105–126.

Weiss, R. F. (1968). Piggyback sampler for dissolved gas studies on sealed water samples, *Deep Sea Res., Part I*, 15, 695–699.

Wen, T., Castro, M. C., Ellis, B. R., Hall, C. M., Lohmann, K. C., and Bouvier, L. (2015). Assessing compositional variability and migration of natural gas in Antrim Shale in the Michigan Basin using noble gas geochemistry. *Chem. Geol.*, *417*, 356–370.

Wen, T., Castro, M. C., Hall, C. M., Pinti, D. L., and Lohmann, K. C. (2016a). Constraining groundwater flow in the glacial drift and saginaw aquifers in the Michigan Basin through helium concentrations and isotopic ratios. *Geofluids*, *16*(1), 3–25.

Wen, T., Castro, M. C., Nicot, J. P., Hall, C. M., Larson, T., Mickler, P., and Darvari, R. (2016b). Methane Sources and Migration Mechanisms in Shallow Groundwaters in Parker and Hood Counties, Texas — A Heavy Noble Gas Analysis. *Environ. Sci. Technol.*, *50*(21), 12012–12021.

Weppernig, R., Schlosser, P., Khatiwala, S., and Fairbanks, R. G. (1996). Isotope data from Ice Station Weddell: Implications for deep water formation in the Weddell Sea. *J. Geophys. Res.*, *101*, 25–723, doi:10.1029/96JC01895.

West, H. B., Gerlach, D. C., Leeman, W. P., and Garcia, M. O. (1987). Isotopic constraints on the origin of Hawaiian lavas from the Maui volcanic complex, Hawaii. *Nature*, *330*(6145), 216–220.

Whittier, R. B., Rotzoll, K., Dhal, S., El-Kadi, A. I., Ray, C., and Chang, D. (2010). Groundwater source assessment program for the state of Hawaii, USA: methodology and example application. *Hydrogeol. J.*, *18*(3), 711–723.

Zwally, H. J., Giovinetto, M. B., Li, J., Cornejo, H. G., Beckley, M. A., Brenner, A. C., Saba, J. L., and Yi, D. (2005). Mass changes of the Greenland and Antarctic ice sheets and shelves and contributions to sea-level rise: 1992–2002. *J. Glaciol.*, *51*(175), 509–527.